Helicopter Blade-Vortex Interaction Locations— Scale-Model Acoustics and Free-Wake Analysis Results

Danny R. Hoad

Aerostructures Directorate
USAARTA-AVSCOM
Langley Research Center
Hampton, Virginia

Summary

The results of a model rotor acoustic test in the Langley 4- by 7-Meter Tunnel were used to evaluate a free-wake analytical technique. The acoustic data were examined in detail for blade-vortex interaction acoustic waveform characteristics. These results were used in an acoustic triangulation technique to define the location in the rotor disk of the noise source. These locations, along with the results of the free-wake analysis, were used to define the geometry of the blade-vortex interaction phenomena as well as to determine if the free-wake analysis is a capable diagnostic tool.

The model used for the investigation was a 1/4-scale (12-ft-diameter rotor) representation of the UH-1 helicopter. Two rotor systems were evaluated—the standard UH-1 rotor with rectangular blades and an advanced version with tapered blades. Several reports evaluating the aerodynamic and acoustic performance benefits or penalties of the advanced rotor system compared with the standard rotor system have been published. This report, however, uses the acoustic data results from the test as an evaluation tool to develop a better understanding of the mechanisms of blade-vortex interaction and does not address any relative performance issues.

The results of the correlation of the experimentally determined source location and the analytically generated wake geometry for the rectangular blades are encouraging. The free-wake analysis successfully predicts the occurrence of blade-vortex interaction and is able to provide information on the interaction geometry. In the case of the advanced rotor system, the correlation between analysis and experiment is poor. The reason for the poor correlation may be related to the selection of the point on the rotor blade where the vortex is defined as being generated. Additional information is needed to provide a better understanding of the wake geometries developed by nonrectangular rotor blades.

Introduction

Blade-vortex interaction (BVI) noise, when present, is independent of the number of blades on the helicopter. Every helicopter experiences this phenomenon in varying degrees, and because the energy content of the BVI mechanism is in the midrange of the human hearing spectrum, it is of considerable concern to the heliport operator, worried about community acceptance, as well as to the military, worried about detectability of the aircraft. This noise source typically occurs during low-power descending flight in which low rotor-disk inflow causes the rotor wake to be blown back into the rotor disk (refs. 1 and 2).

The rotor wake is imbedded with concentrated vortices shed from previous blade passages, and the close encounter of a rotor blade with these vortices can cause the distinctive blade slap sounds. Some very recent work has concentrated on the physics of the interaction process and has shown that the acoustic emission depends critically upon the vortex path and orientation at each intersection (ref. 3). Other researchers have looked at the deformation of the transverse vortex as it encounters a lifting body and how its path is altered (ref. 4). Although informative, these fundamental studies cannot account for the complex flow field of the helicopter wake in forward flight.

The vortex paths, in a simplified rotor-wake approximation, are helical patterns convected rearward away from the rotor at the free-stream velocity and downward at the momentum inflow velocity. The actual helicopter rotor wake is not as simple as this approximation. The tip-vortex paths depend heavily on the interaction of the tip vortices with all the blades, on the interaction of the tip vortices with other vortices in the flow field, on the presence of the fuselage, on the turbulence of the free stream, and on a myriad of other possible distortion effects which are not fully understood. Close to the rotor, the most pronounced effects on the helical pattern are probably the large vertical motions of the vortex paths caused by the bound circulation of a nearby blade. These abrupt vertical motions cause the vortex to be convected into or very near the path of a rotor blade, setting up the kinds of interactions noted in references 3 and 4. The critical factor in understanding the BVI process and in being able to predict the noise propagation from this phenomenon is the ability to predict the position and the geometry of the blade-vortex interaction. The free-wake analysis (refs. 5 and 6) is a tool which allows the rotor–wake analyst to study the wake structure of a fully converged rotor-blade wake interaction process.

The results of a scale-model helicopter acoustic test have been used to provide a measure of confidence in the free-wake analyses through use of the acoustic data and an acoustic triangulation technique to identify the location in the rotor disk where blade-vortex interaction occurred. The triangulation was used successfully in reference 7 on acoustic data acquired from a four-bladed rotor system and again in reference 8 on another four-bladed rotor system. The wake analysis (refs. 5 and 6) was used for both programs. In reference 7, the free-wake module was used; however, in reference 8, a prescribed-wake module was used. The prescribed-wake module is a first-level, generalized-wake model and is designed to reduce the computation time required for a

complete distorted-wake calculation. The use of the generalized-wake module was relatively unsuccessful, probably because the geometry of the rotor model used for the tests was not the same as that used to generate the generalized-wake (prescribed-wake) code. Consequently, this report concentrates on the free-wake module from references 5 and 6. A large amount of computer time was needed for complete convergence; however, the details of the complex rotor-wake environment were considered to be well worth the additional expense.

The data used in these analyses were acquired in an experimental program defined in references 9 to 14. Aerodynamic results are available in references 9 and 10. The high-speed impulsive noise characteristics can be found in references 11 and 12, and the BVI noise results are available in references 13 and 14.

Symbols

C_L rotor lift coefficient, $\frac{\text{Rotor lift}}{\rho\pi R^2(\Omega R)^2}$

C_T rotor thrust coefficient, $\frac{\text{Rotor thrust}}{\rho\pi R^2(\Omega R)^2}$

c standard rotor system blade chord, 5.25 in.

D rotor drag, lb

L rotor lift, lb

P sound pressure, dynes/cm^2

R rotor radius, 6.00 ft

r local blade radial location, ft

V_T rotor tip speed, ft/sec

V_∞ free-stream velocity, ft/sec

x,y,z coordinates for microphone locations in tunnel, ft

α_{TPP} rotor tip-path-plane angle of attack, deg

γ rotor descent angle, $\tan^{-1}(D/L)$, deg

μ rotor advance ratio, V_∞/V_T

ρ free-stream density, slug/ft^3

Ω rotor rotational speed, rad/sec

Abbreviations:

ARS   advanced rotor system

BVI   blade-vortex interaction

CG   center of gravity

GRMS   general rotor model system

SRS   standard rotor system

Test Apparatus

Helicopter Model

The general rotor model system (GRMS) (ref. 15) was mounted in the Langley 4- by 7-Meter Tunnel for this investigation. The fuselage was a $^1/_4$-scale representation of the UH-1 helicopter and was mounted to the GRMS with a balance to provide independent fuselage load data. The rotor system was independently mounted on a separate six-component strain-gage balance within the model. (See fig. 1.) The rotor performance data presented in this report were acquired with the rotor balance.

Figure 2 shows a sketch of the model and the two rotor systems tested. Both main rotor systems were mounted to a geometrically scaled version of the UH-1 helicopter hub. The standard rotor system (SRS) was geometrically and dynamically scaled to the current UH-1 helicopter rotor configuration, whereas the advanced rotor system (ARS) had a modified blade planform and was constructed with dynamic characteristics as close as possible to those of the SRS. The ARS had a wider root chord than the SRS and had a 3-to-1 taper ratio beginning at 0.50R. Advanced rotorcraft airfoils (ref. 16) were used, with thickness ratios ranging from 12 percent inboard to 8 percent at the tip. Both sets of rotor blades were made of fiberglass/Kevlar[1] composite and had a graphite/epoxy composite structural torque box. The SRS aerodynamic contours were formed by an external fiberglass/epoxy shell with a Nomex[2] honeycomb core in the trailing edge. The ARS aerodynamic contours were formed similarly except that the trailing edge was formed with a Styrofoam[3]/balsa core. Details of the geometric characteristics of the two rotor systems are provided in figure 3 and in table I.

The rotor blades were mounted to a teetering hub with cyclic and collective pitch on the blades controlled by a swashplate driven by remotely controlled actuators. Teetering measurements were made at the teetering axis. The rotor was driven by a 90-hp electric motor through a transmission. The entire system (rotor, transmission, and motor) was mounted on the rotor balance as shown in figure 1.

---

[1] Kelvar: Trade name of E. I. du Pont de Nemours & Co., Inc.

[2] Nomex: Trade name of E. I. du Pont de Nemours & Co., Inc.

[3] Styrofoam: Trade name of Dow Chemical Co.

The helicopter model was supported in the wind tunnel by a three-joint sting which allowed model pitch and yaw control to ±45° about a fixed point on the model. The three-joint sting was mounted on a model support system which allowed height control as well as limited additional pitch and yaw control. A photograph of the model installed in the wind tunnel is presented in figure 4.

Wind-Tunnel Facility

The model investigation was conducted in the NASA Langley 4- by 7-Meter Tunnel operated in the optional open-throat configuration. The rectangular jet entrance to the test chamber is 14.50 ft high by 21.75 ft wide. The ceiling in the open-throat configuration is simply raised from the closed-throat configuration and is approximately 24.6 ft above the test chamber floor. In order to improve the anechoic characteristics of the test chamber, acoustic treatment was installed on the test section floor and ceiling. This acoustic treatment, which is partially visible in figure 4 and is indicated in figure 5, consisted of fiberglass-filled aluminum panels and open-cell polyurethane foam. Aluminum panels 5 in. thick were installed on the floor directly under the model as a semirigid floor to facilitate periodic maintenance and modifications to the model rotor system. Polyurethane foam 4 in. thick was installed on the floor directly upstream of the aluminum panels and overhead on the surface of the raised ceiling. An evaluation of the effectiveness of this acoustic treatment is reported in reference 17.

Instrumentation

The acoustic transducers used for this investigation were 1/2-in-diameter condenser microphones fitted with standard nose cones. Eight microphones were positioned in the flow around the model. Figure 4 is a rear-quarter-view photograph of the model installed in the tunnel with acoustical treatment and shows the relative locations of six of the microphones. A sketch showing the relative position of all components in the test chamber in more detail (microphones, model, ceiling, tunnel lip, treatment, and so forth) is provided in figure 5.

Data from five of the eight microphones have been used to compute the source-location data in this report. The locations of these five microphones relative to the rotor hub with the model at zero angle of attack are presented in table II. Microphone 2 was mounted close to the fuselage under the rotor disk in a location shown to be relatively sensitive to BVI noise (refs. 18 and 19). Microphone 4 was mounted upstream of the model near the plane of the rotor disk. Although the position of microphone 4 is not considered to be a sensitive location for the measurement of BVI, time history data from this microphone were helpful in some cases in computing the location of BVI. Microphones 6, 7, and 8 were mounted upstream of the model as far as possible from the rotor at about 30° below the rotor tip-path plane. The directivity of the BVI blade slap has been shown experimentally (ref. 2) and theoretically (ref. 20) to be a maximum in the direction of microphones 6, 7, and 8. Signals from each microphone were fed through an amplifier-attenuator and into a 14-channel frequency-modulated (FM) tape recorder operating at a tape speed of 30 in/sec tape speed, thus providing a 10-KHz bandwidth capability. Blade azimuth and time code were also recorded.

The acoustic analog signals were digitized through use of a conditional sampling technique triggered on the rotor signal once per revolution. The synchronized digitized data provided 1024 equally spaced intervals for each revolution. Acoustic data were digitized for a period of time equal to approximately 50 rotor revolutions. For this particular data set, a band-pass filter (set at 10 to 10 000 Hz) was used in the digitizing process.

An in-line white noise signal was inserted simultaneously into each data channel to identify phase errors. The phase of the cross-power spectral density function between any two channels showed that the phase errors were less than the time interval of the digitized samples; therefore, no corrections to relative time measurements because of channel-to-channel phase errors were made.

Operating Procedures

The test procedures utilized to define the BVI envelope for either rotor system were identical. At each advance ratio, the simulated descent angle was varied from a climb condition with little observable BVI to a descent condition with maximum BVI to a high-descent condition with BVI appearing to vanish. This procedure provided a matrix of flight conditions (fig. 6) at which both the rotor systems were operated. The procedure used to establish each flight condition was to set a constant advance ratio and then adjust collective, cyclics, and model angle of attack to obtain the desired rotor C_L. In addition to the desired C_L, the adjustments in the controls provided zero longitudinal flapping and a small negative lateral flapping. The angle-of-attack adjustments were required to provide the desired simulated descent angle $\gamma = \tan^{-1}(D/L)$. With the rotor system at the desired condition, approximately 30 sec of analog acoustic data were recorded on

the FM tape recorder, and model and tunnel information were recorded simultaneously on the tunnel data-acquisition system.

Acoustic Triangulation Technique

Blade-vortex interaction locations were computed with an acoustic ray tracing technique successfully used in references 7 and 8. The complete acoustic data for both rotor systems and all microphones were carefully examined to identify those data points and microphones where BVI impulses existed. An example of a condition for which BVI exists and is identifiable in several microphones is provided in figure 7. This figure shows a 1-revolution sample of acoustic data for microphones 2, 6, 7, and 8 for the SRS at an advance ratio μ of 0.124, a thrust coefficient C_T of 0.00317, and a descent angle γ of $-0.04°$. The origin of the data for each microphone corresponds to the instant in time when the reference blade passed 0° azimuth. Three positive-amplitude BVI's are identified in the microphone data as impulses A, B, and C. Those identified in microphones 2, 6, and 7 were relatively easy to associate with each other. In some cases, such as the data for microphone 8, knowledge of the approximate relative propagation times between the rotor advancing side and each microphone location were helpful in identifying the specific impulse.

To compute the source location of the BVI, each acoustic time history data file was examined in detail to determine the exact time interval between the time at which the reference blade passed 0° azimuth and the time at which the BVI arrived (fig. 7). The propagation times were corrected for the effect of tunnel speed and then converted to distances of acoustic wave travel with the measured speed of sound. The location of the origin of the rotor-disk axis system was corrected for deflection resulting from sting bending according to the amount of rotor lift generated and the measured spring constant of the sting structure. Since the axis system was fixed to the rotor disk, microphone positions varied according to the rotor tip-path-plane angle of attack. These positions were corrected from the measured microphone positions at 0° rotor-disk angle of attack through use of the measured shaft angle and longitudinal flapping angle. Geometric triangulation was then applied with the corrected BVI propagation times and the corrected microphone positions to arrive at a locus of points in the truncated cone inscribed by the rotor blades where BVI could have occurred. To compute the location of the BVI in the three-dimensional truncated cone, a set of simultaneous fourth-order equations were required with input from the acoustic data from at least three microphones. For each of these possible locations, the actual instant of BVI impulse emission was calculated as well as the azimuth location of the rotor blades. The BVI locations presented are those chosen when these two locations coincided within 0.0278R along any axis direction.

Probably the most significant error inherent in the source-location calculations is the assumption of rigid blade motion. Flapwise bending motion of the rotor blades is the largest source of error. In addition, the acoustic wave propagation is not corrected for nonuniformities in the fluid medium such as rotor and wake interactions.

Analytical Model

The rotorcraft wake analysis described in references 5 and 6 was used for the predictions in this report. The results of this code, the local time-varying blade circulation distributions, were used as input to a free-wake module. The free-wake module, in turn, computed a fully interactional wake geometry which was used as input for the rotorcraft wake analysis. This iteration process typically required five to seven cycles before acceptable convergence was attained based on the blade circulation distribution. This code did not model any components on the helicopter except the rotor system; there were, therefore, no fuselage interactional effects included in the calculations.

In these analyses, each blade was represented by a segmented lifting line, and the helical wake of the rotor was represented by discrete segmented vortex filaments. The strength of each trailing-vortex segment was a direct result of the spanwise variation of bound circulation at the time of tip-vortex generation. The converged solution included a full wake geometry, or blade tip-vortex paths. The full-wake-geometry data were compared with the calculated values for rigid blade motion in a detailed point-by-point fashion to determine probable BVI's. If the distance between the vortex and the filament was found to be within 0.03R in any direction, the geometric characteristics of the BVI were recorded.

The inputs for the analysis included rotor geometry, rotor operating conditions, rotor flow-field characteristics, and program control. The inputs were carefully prepared from the aerodynamic data acquired during each acoustic data run. The blade was divided into nine segments and the wake calculations were made at 15° azimuthal time steps for 5 rotor revolutions.

A sample plot of a fully converged rotor wake is presented in figure 8 for a blade azimuth of 60° and 240°. Figure 8(a) is a view from above and to the left rear of the rotor system and points out those

filament-blade locations where BVI could occur. Vertical distortions of the filaments occur predominantly at the edge of the wake in a rolled-up pattern similar to that of a fixed-wing wake. Figure 8(b) is a view from just above and directly behind the rotor and clearly shows the large vertical motions of the vortex filaments. The possible BVI's identified in figure 8(a) were a result of a vertical motion of each filament as it was influenced by the passage of a rotor blade.

Discussion Of Results

Acoustic Data Results

The acoustic data and results of the source-location calculations pertinent to this report are included in the appendix. Figure 9 presents a sample of the data in the appendix displayed as an acoustic time history cascade. At each descent angle, acoustic data for a half of a rotor revolution are presented, always beginning at the time when the reference blade passed $0°$ azimuth. The method of presentation allows the reader to visualize the migration of the BVI impulses as the descent angle varied. For instance, in figure 9 at large negative descent angles (climb), impulse A is evident but impulses B and C are not. Impulse C begins to be evident at $\gamma = -2.05°$, and impulse B becomes evident at $\gamma = -0.04°$. Impulse A is always present whereas impulses C and B are not present for descent angles greater than $2.79°$. The data from microphone 6 (fig. 9(b)) show that impulses A and B are evident throughout the descent envelope tested. Each impulse has a characteristic waveform that seems to distinguish it from the other, and that waveform is carried through at each advance ratio and thrust coefficient. These different characteristics suggest different source mechanisms such as vortex strength, vortex age, blade-vortex interaction angle, or blade-vortex vertical separation. Waveforms that are broad (such as impulse C) produce an energy content at lower frequencies than waveforms that are sharp and distinct (such as impulse A).

Because the impulses have distinctly different waveform characteristics, each particular impulse displayed in the time histories can be localized with reasonable confidence in the results. The triangulation routine requires that the same impulsive signal be identified in at least three microphone signals and that these phenomena be identifiable very accurately in time. Without this restriction, the accuracy of the source location would be very poor, and because of it, not all impulses evident in the time histories can be localized. For instance, for microphone 7 at $\gamma = -0.04°$ (fig. 9(c)), three possible BVI impulses exist. Impulses A and C can be identified, but it is unclear which impulse can be labeled as B, which is clearly identified in the data for microphone 2 (fig. 9(a)). It is possible that a retreating-side BVI is buried within these data, but it is not easily identified.

The results of the triangulation calculations are also included in the appendix. Figure 10 presents a sample figure from the appendix where the data correlate with the acoustic time history data in figure 9. The data points in figure 10 represent source-location calculations for all descent angles available for the advance ratio and thrust coefficient represented in figure 9. The source locations in figure 10 have been identified as to waveform shape so that the results are compatible with the information presented in time history format in figure 9. For example, three BVI locations are identified in figure 10—A, B, and C— and they are the same as those identified in figure 9.

An example of the variability of the BVI source location as a function of the descent angle at a constant thrust coefficient and advance ratio is presented in figure 11. The data show the radial and azimuthal position of the BVI source (impulse A) as a function of descent angle for the standard rotor system at an advance ratio of 0.104 and a thrust coefficient of 0.00313. In general, as the descent angle increases the azimuth of the BVI tends to migrate towards $90°$. These trends existed for most of the data presented.

Most of the source locations computed for this data set were in the first quadrant ($0°$ to $90°$ azimuth), as was the case in references 7 and 8. References 21 and 22 have implied the existance of retreating-side BVI. If such a phenomenon exists in these data, there is no proof; however, it is important to remember that this source-location technique requires absolute identification of BVI's in the data for three microphones. Only the very strongest BVI's will be identifiable in the microphone data (particularly in more than one microphone). The retreating-side BVI may be buried in some of these data, but it cannot be specifically identified.

In the data there is no obvious trend of source location with increasing advance ratio. Consistently, impulse B was found outboard of impulse A, and impulse C was found inboard of impulse A. (See fig. 9.) These results suggest the possibility of a correlation of the source location with a particular vortex, with the free-wake analysis being used to identify the vortex.

Analytical and Experimental Comparison

It has been suggested and shown by limited flow visualization in reference 23 that, in the immediate vicinity of the rotor disk, the plan view of the

rotor-wake geometry conforms to an undistorted classic helical path. This helical path traces a point near the blade tip from the location where the rolled-up tip vortex originates. One may conceivably sketch this pattern in plan view and be able to draw conclusions about the possible BVI locations in the rotor disk. From the plan view the complete path of the vortex across the rotor disk must be chosen as possible interaction sources unless specific information about the vertical motion of the vortices is available. These conclusions leave a broad area of possible interaction that encompasses a large portion of the rotor disk. It is known from considerable work in free-wake analyses and rotor-wake measurements that the blade tip-vortex paths do not follow a vertical path consistent with average momentum downwash velocity (refs. 23 to 25). These vortices are, in fact, greatly affected by the passage of the bound vorticity representative of a rotor blade, especially in the near wake of the rotor. In some cases the vortices pass up through the rotor disk and exist above the path of the blades for long periods of time (ref. 24). This passage of the rotor tip vortices through the disk gives rise to the BVI phenomena. The occurrence of this motion is critical to the isolation of the BVI phenomena locally in the rotor disk. The results of the rotorcraft wake analysis code utilized in this report address these vertical excursions.

Several model operating conditions were chosen for comparison of the experimentally determined BVI source with analyses. These conditions were as follows:

Figure

Standard rotor system—$\mu = 0.124$:

$C_T = 0.00314;\ \gamma = -2.05°$ . . . . 12(a)
$C_T = 0.00314;\ \gamma = -1.02°$ . . . . 12(b)
$C_T = 0.00319;\ \gamma = 1.83°$ . . . . 12(c)
$C_T = 0.00317;\ \gamma = 2.79°$ . . . . 12(d)

Advanced rotor system:

$C_T = 0.00304;\ \mu = 0.146;\ \gamma = -1.28°$ . . 13(a)
$C_T = 0.00310;\ \mu = 0.146;\ \gamma = 3.56°$ . . . 13(b)
$C_T = 0.00319;\ \mu = 0.157;\ \gamma = 1.42°$ . . . 13(c)
$C_T = 0.00324;\ \mu = 0.157;\ \gamma = 5.42°$ . . . 13(d)

Figures 12 and 13 are presented in polar coordinate format showing the particular BVI encounter measured in the acoustic data as plus signs inside an elliptical area and the predicted BVI encounters as shaded areas. The predicted encounters were chosen based on the criteria that a tip vortex had to pass within $0.03R$ of a rotor blade in any direction. In some cases the predicted encounter on the retreating side of the rotor disk was the same vortex as

that on the advancing side. Two full-wake representations are provided in figures 14 and 15 and illustrate the wake geometries used for the predictions in figures 12(a) and 12(c), respectively. In figure 14, all tip-vortex paths are displayed for 5 revolutions, and the predicted BVI's are highlighted as shaded areas. It is clear in this figure that use of the free-wake calculations reduced the extent of possible interaction locations substantially compared with use of the classic helical wake to define the location of BVI's.

After detailed examination of the wake-geometry data file on a point-by-point basis, it is possible to conclude that BVI impulse A was a result of an interaction of a tip vortex generated by a blade when it was at an azimuth of 105°, thus providing an indication of the relative strength of the vortex. In addition, the vortex was 1 complete revolution old and was interacting with the same blade that generated it. The free-wake geometry predicted that before interaction the vortex was in a path that was above the rotor disk. Figure 12(b) and its corresponding wake geometries (not shown here) show identical results.

At first glance, figures 12(c) and 12(d) seem to indicate that BVI impulse C in fact may have been in the same location as BVI impulse A (figs. 12(a) and 12(b)) and may not have been another BVI. This, however, is not the case if the full wake geometry is examined in figure 15. The shaded area, which appears in figure 12(c) to agree with BVI impulse C, is shown in figure 15 to have been caused by a different BVI. The interaction occurred with a vortex that was generated at 150° azimuth and was 1½ revolutions old. In fact, the interaction was with the vortex of the opposite blade and occurred when the vortex was pulled down from above the rotor disk, as was the case with BVI impulse A of figure 12(a).

With these events in mind, let us look at the time history representation of figure 9(a) for microphone 2. At a descent angle of −1.02°, BVI impulse A appears to be crisper and sharper than BVI impulse C. The positive side of BVI impulse A is steeper than that for BVI impulse C, whereas impulse C tends to be broader throughout the descent angle range. This waveform difference is probably caused by either the increased age of impulse C or a slight difference in vertical spacing between blade and vortex. The results of reference 3 analytically have shown similar kinds of waveform variations with vertical separation variations between the vortex and blade.

The results of the analyses for the advanced rotor system are not as successful as those for the standard rotor system. Figure 13 presents the comparison of analysis with experimentally determined interaction locations and shows poor correlation. Little

experimental information is available concerning the wake geometry generated by a tapered blade planform such as this. In the analysis, the tip vortex is assumed to trail from the tip of the blade; however, it is more likely that for a tapered blade the concentrated trailing vortices leave the blade at some location inboard of the tip, perhaps even as far inboard as the point of taper initiation. It is also possible that the tapered blades, in effect, distribute the vorticity along the blade, and the results shown for the experimentally determined source location are from only the strongest of the vortex encounters. Whatever the cause of the poor performance of the free-wake analysis, it is clearly evident that future effort needs to be applied to understand nonrectangular-blade wake geometries, particularly vortex formation.

Conclusions

The results of a model rotor acoustic test in the Langley 4- by 7-Meter Tunnel were used to evaluate a free-wake analytical technique. The acoustic data were examined in detail for blade-vortex interaction (BVI) acoustic waveform characteristics. These results were used in an acoustic triangulation technique to define the location in the rotor disk of the noise source. These locations, along with the results of the free-wake analysis, were used to define the geometry of the BVI phenomena as well as to determine if the free-wake analysis is a capable diagnostic tool. Some of the conclusions are summarized as follows:

1. Those BVI's of sufficient strength to be identified (so that the source location routine could be utilized) were caused by a vortex which, before interaction, had been above the path of the blades over the front portion of the rotor disk. The interaction occurred when the vortex was pulled down through the rotor disk.

2. Correlation of the free-wake analysis with the source-location data provided confidence in the analysis as a diagnostic tool for the standard rotor system. Care should be taken in applying the analysis to rotor systems for which the input assumptions are not strictly applicable. The results for the advanced rotor system (i.e., with tapered blades) did not correlate well with the wake-geometry predictions, and the error may have been caused by the selection of the location defining where the vortex trailed from the rotor blade.

3. The analytical results for the rotor-wake geometries indicated that retreating-side BVI was likely; however, the source location only identified source mechanisms in the first quadrant of the rotor disk. The triangulation technique requires precise identification of the same BVI in the data of at least three microphones. The retreating-side BVI, if present, was not of sufficient magnitude to meet these criteria.

NASA Langley Research Center
Hampton, VA 23665-5225
December 10, 1986

Table I. Rotor Characteristics

Number of blades 2

Airfoil section:
    SRS . . . . NACA 0012
    ARS . . . . RC(3)-12, RC(3)-10, RC(3)-08

Radius, ft 6.00

Blade chord:
    SRS, in. 5.25
    ARS, in. . . . . 2.21 to 6.62

Twist:
    SRS, deg . . . . -10.9
    ARS, deg . . . . -14.0

Planform solidity:
    SRS 0.04642
    ARS 0.04863

Root cutout, ft 0.5089

Table II. Microphone Locations Relative to Rotor Hub With Model at Angle of Attack of 0°

Microphone location	x, ft	y, ft	z, ft
2	-1.558	2.215	-2.493
4	-10.742	7.083	$-.558$
6	-11.250	3.793	-5.666
7	-11.250	$-.167$	-5.656
8	-11.250	-4.377	-5.666
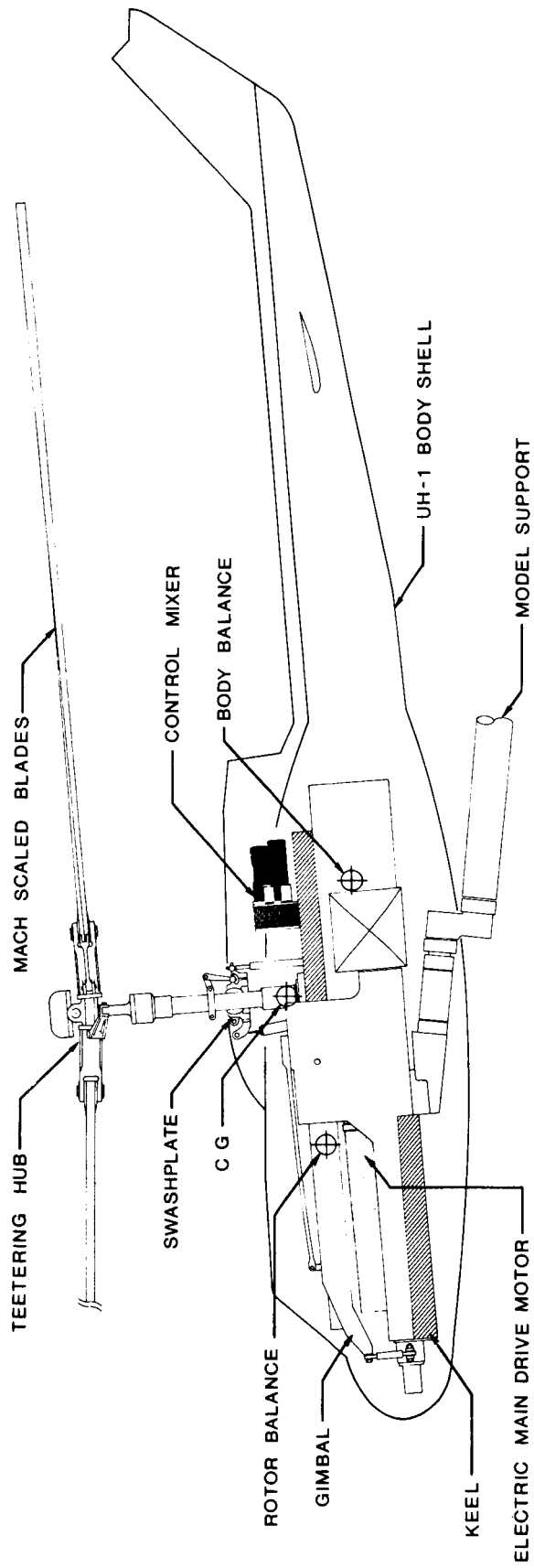
Figure 1. Model of UH-1 fuselage installed on GRMS.

TEETERING HUB

MACH SCALED BLADES

CONTROL MIXER

BODY BALANCE

UH-1 BODY SHELL

MODEL SUPPORT

SWASHPLATE

C G

ROTOR BALANCE

GIMBAL

KEEL

ELECTRIC MAIN DRIVE MOTOR
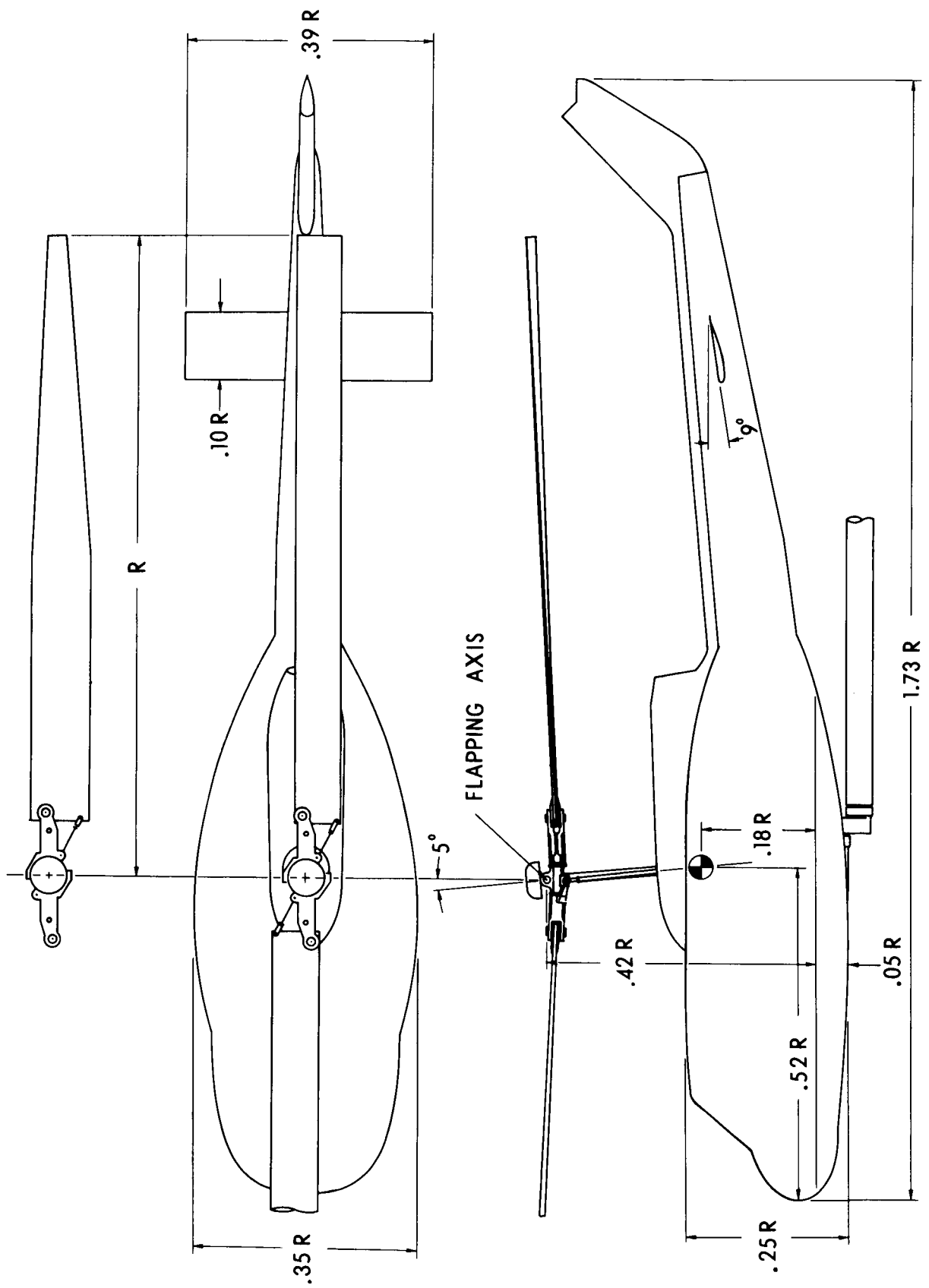
Figure 2. Model of UH-1 helicopter tested.

Standard blade

c

NACA 0012

R

+

Advanced blade

.42c

R

RC(3)-08

.9R

RC(3)-10

.8R

.5R

RC(3)-12

1.26c
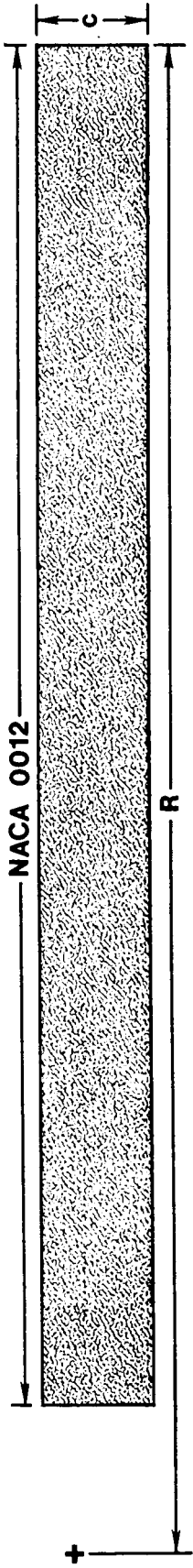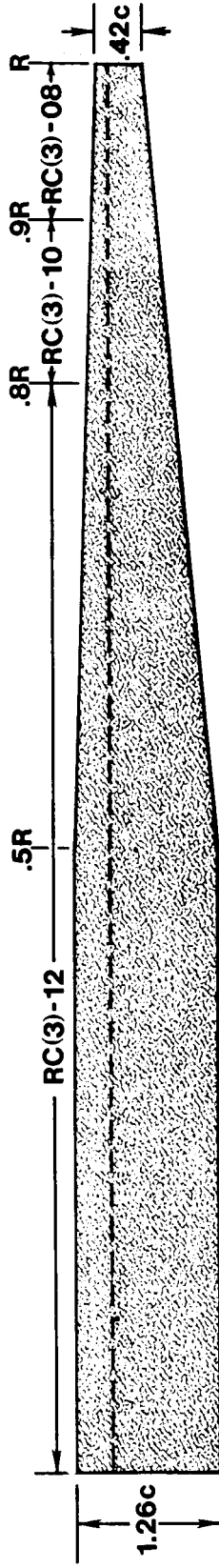
Figure 3. Geometric comparison of standard and advanced rotor blades.
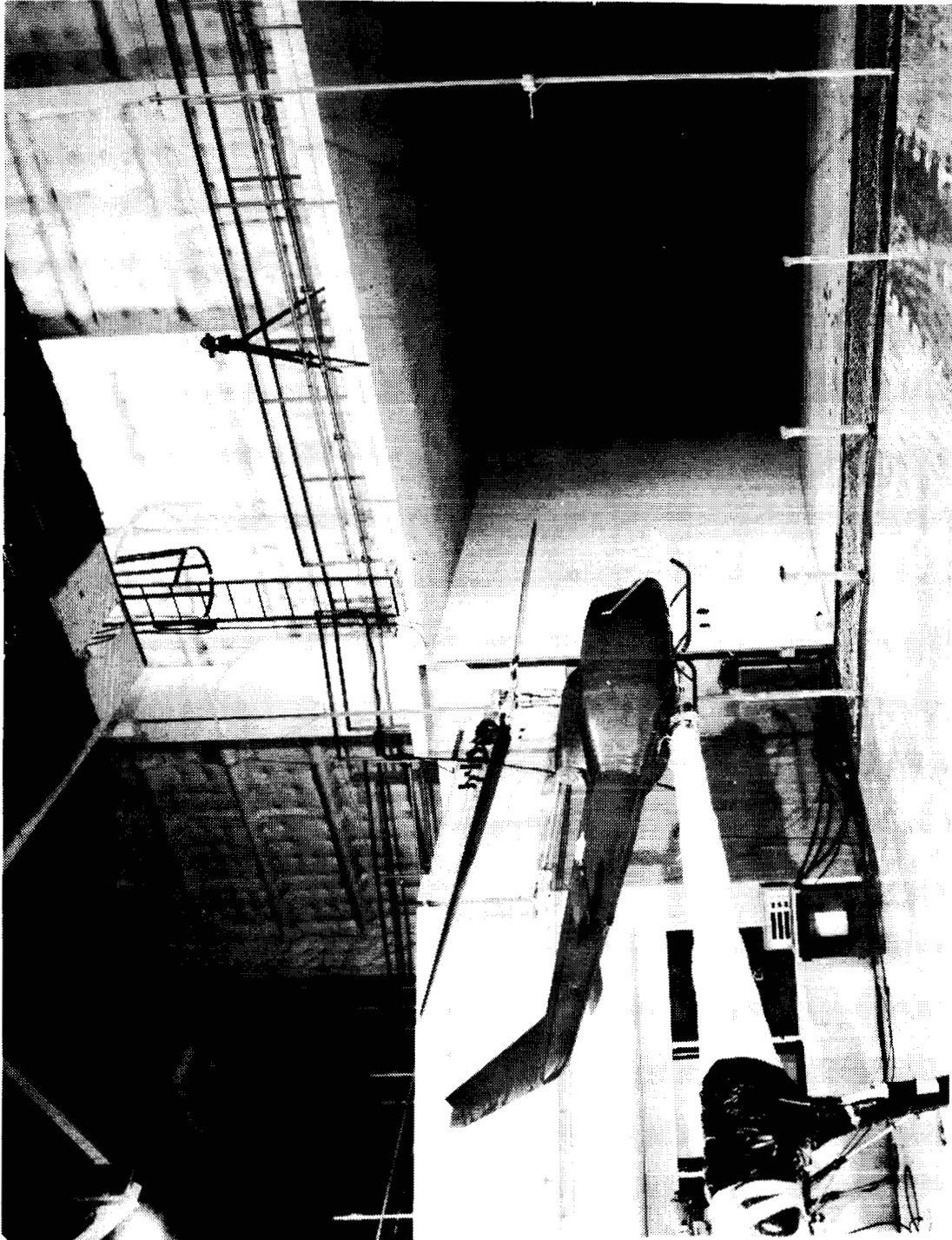
Figure 4. Rear quarter-view of UH-1 helicopter model in tunnel with acoustic treatment and microphones installed.

L-87-553
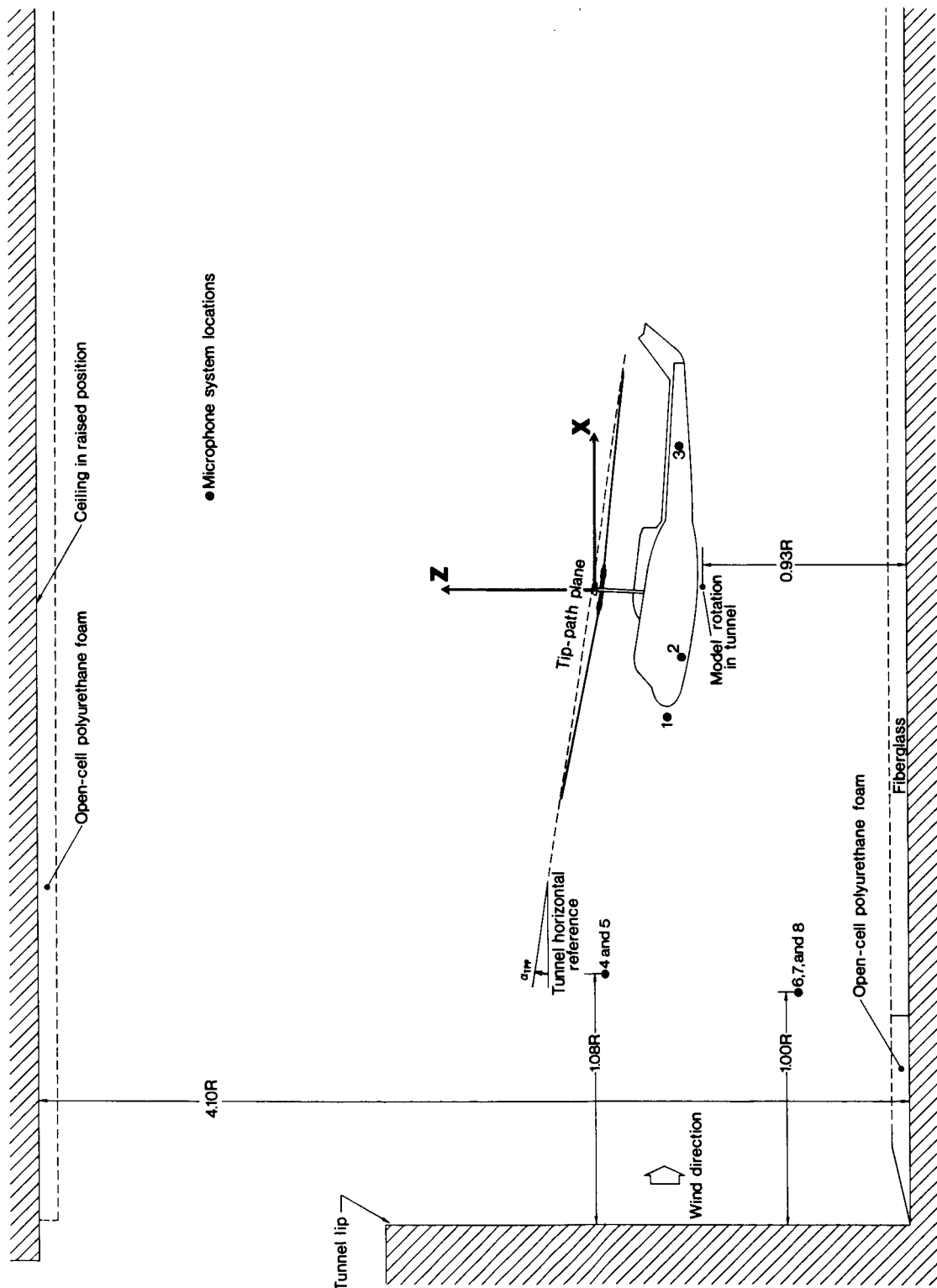
(a) Side view.

Figure 5. Relative position of components in acoustic test of UH-1 helicopter model.

Fiberglass filled panels

Open-cell polyurethane foam

Tunnel lip

Wind direction

Tunnel centerline

Fiberglass filled panels

Open-cell polyurethane foam

1.0R

X

Y

• 3

• 2

• 1

• 4

• 6

• 7

• 8

• 5

• Microphone system locations

Floor treatment installed over existing floor
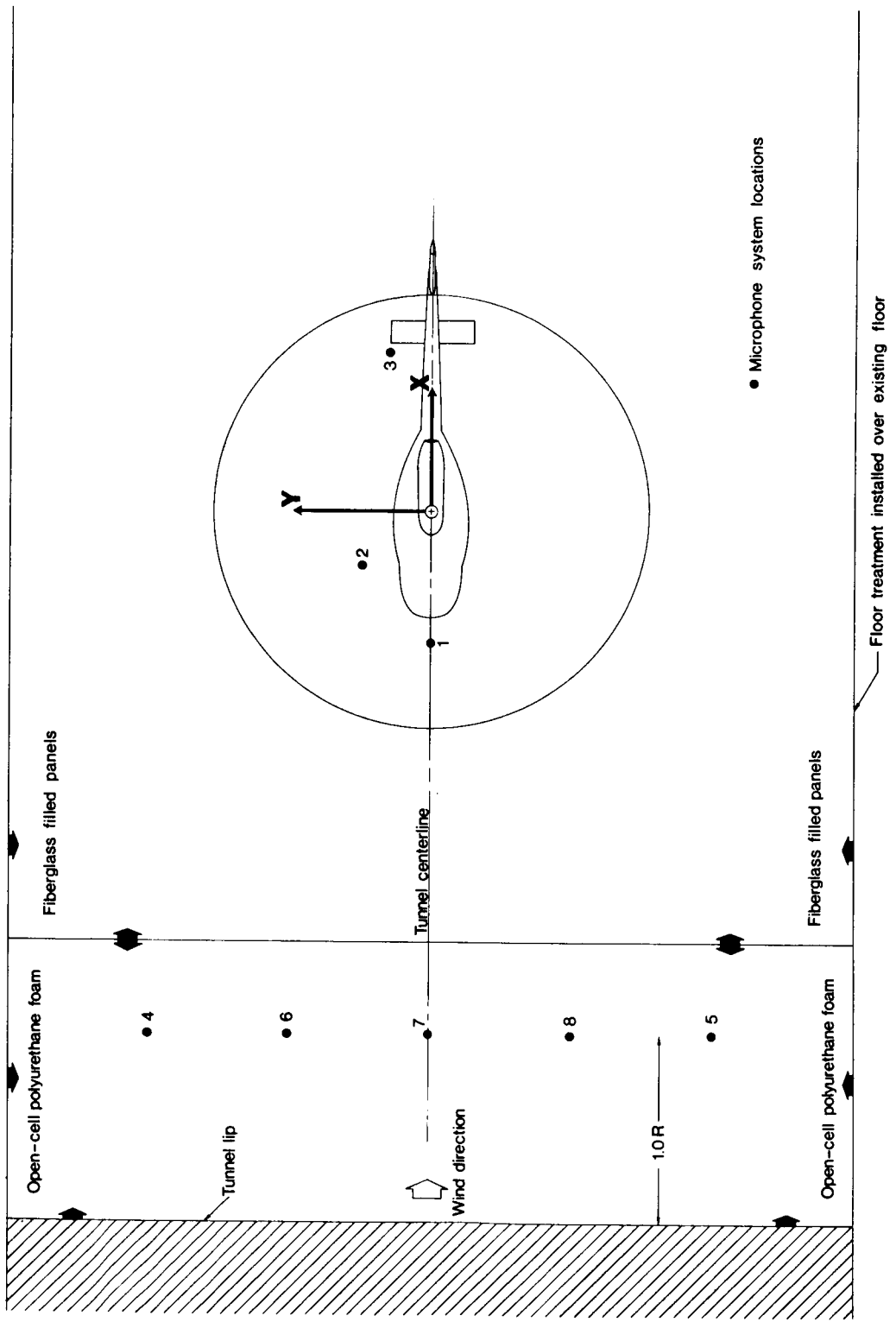
(b) Top view.

Figure 5. Concluded.
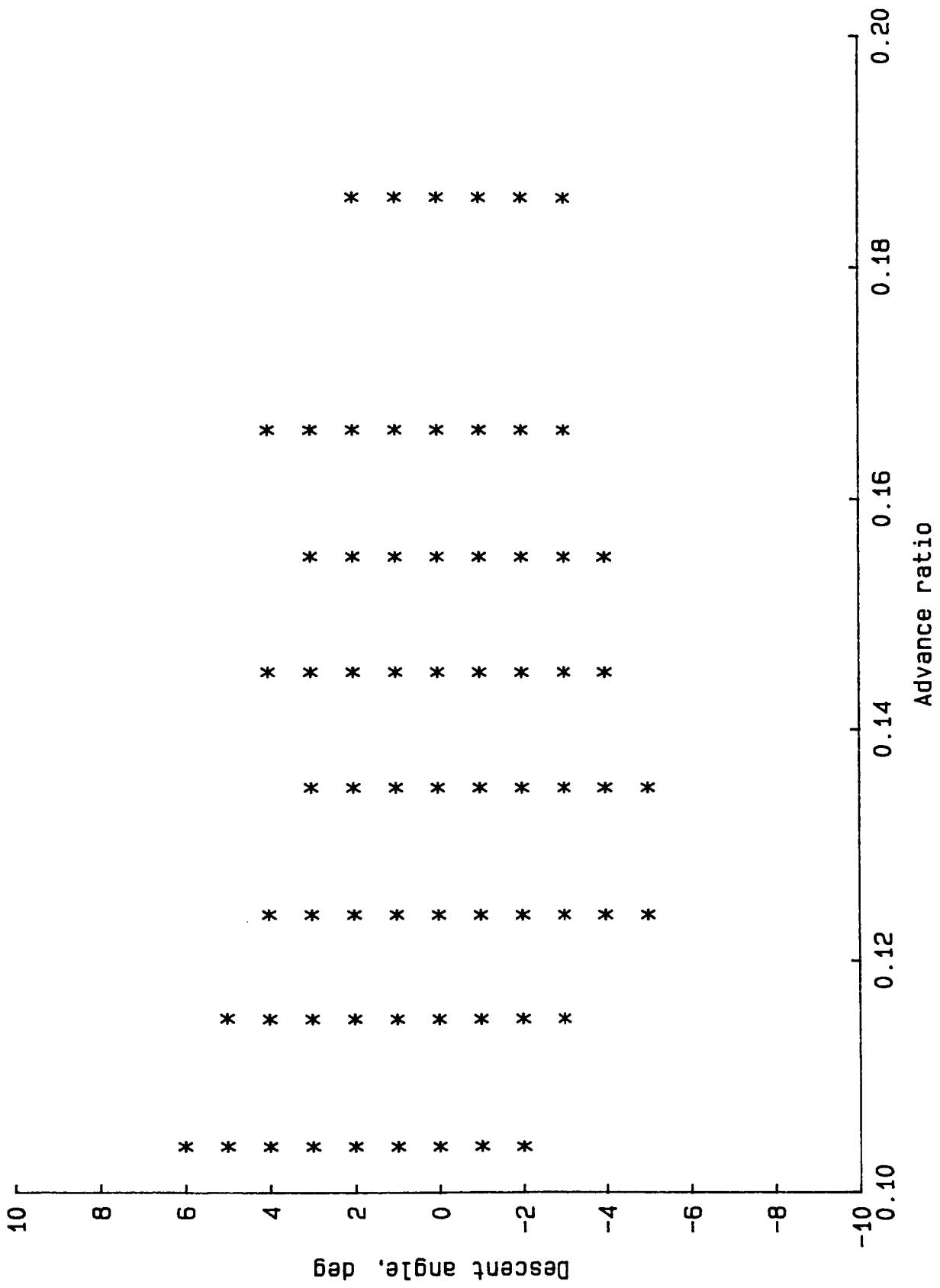
Figure 6. Rotor operating conditions for UH-1 rotor-system acoustic tests. Descent angle based on rotor balance data.
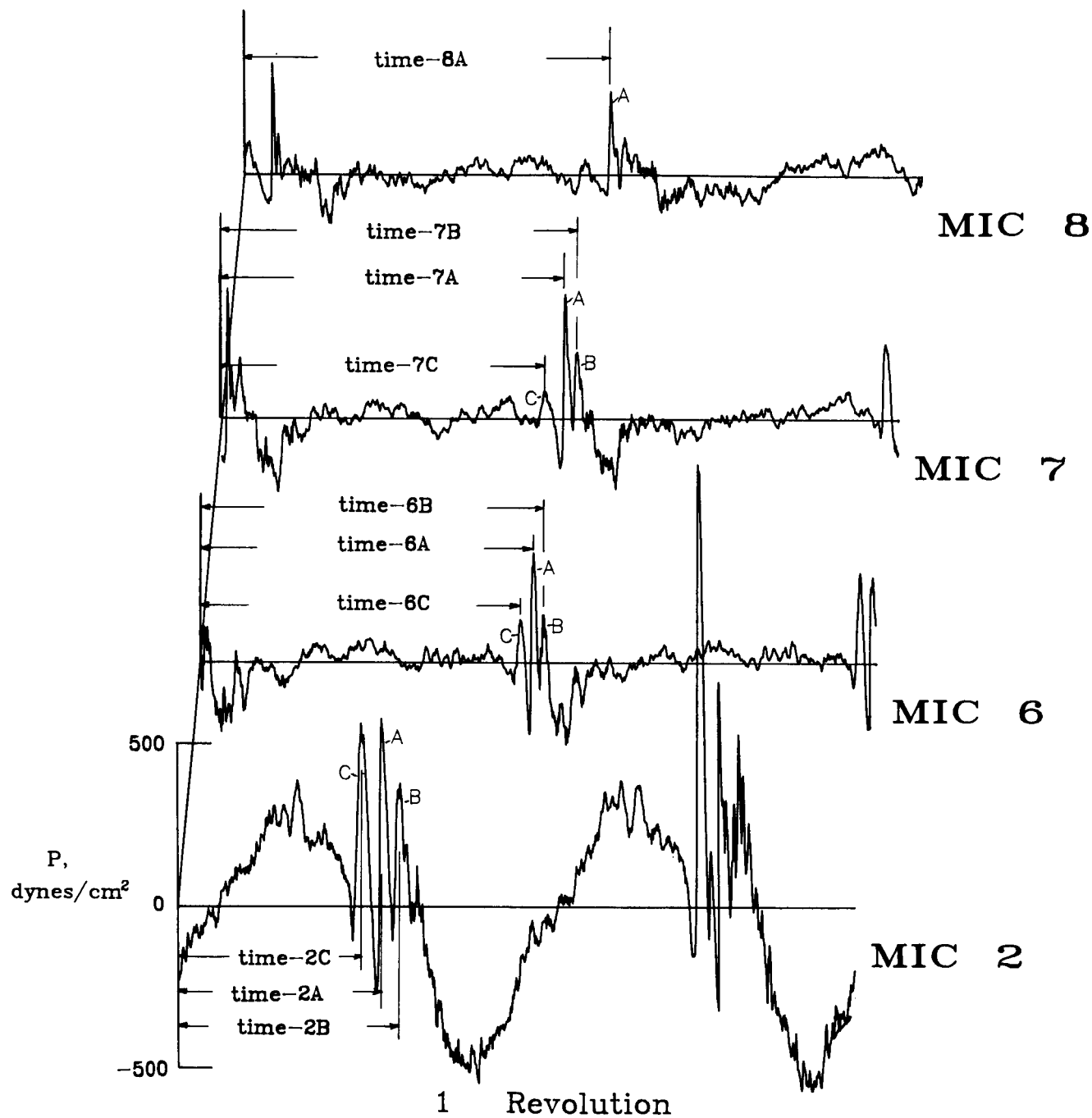
Figure 7. Example of source-location time interval calculations from four microphones for standard rotor system. $\mu = 0.124$; $C_T = 0.00317$; $\gamma = -0.04°$.
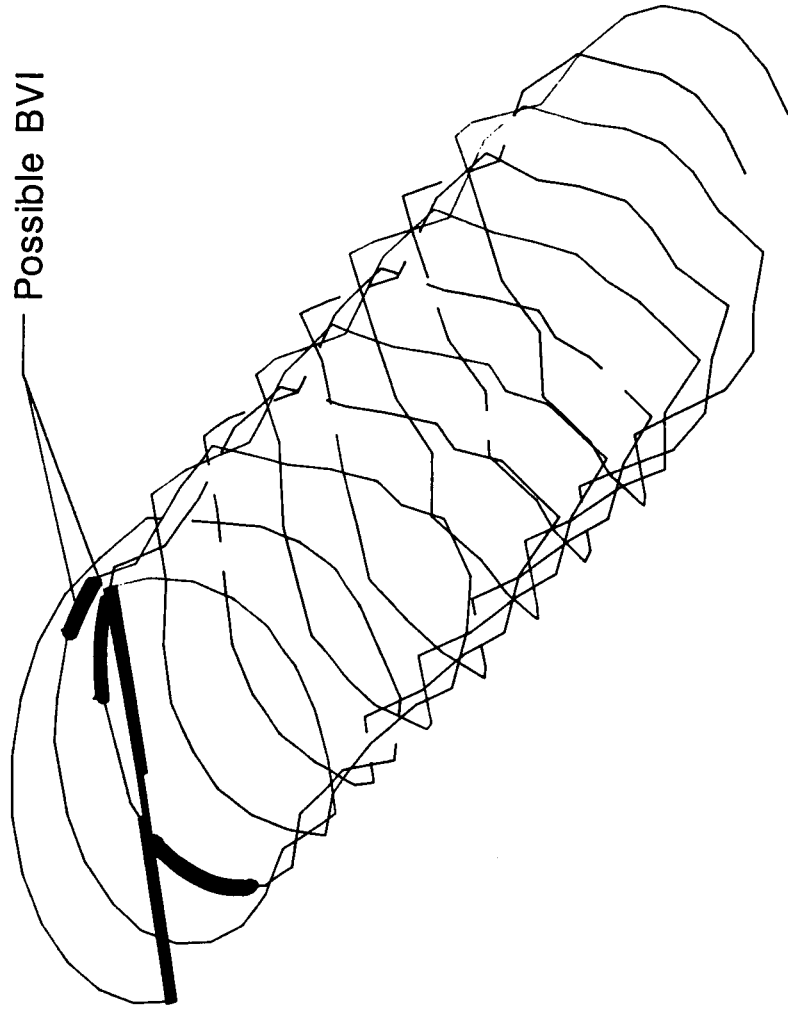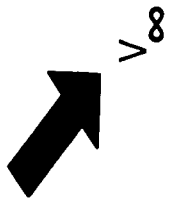
(a) View from above and to left rear of rotor.

Figure 8. Typical rotor-wake geometry for fully converged solution with rotor blades at azimuth 60° and 240°.
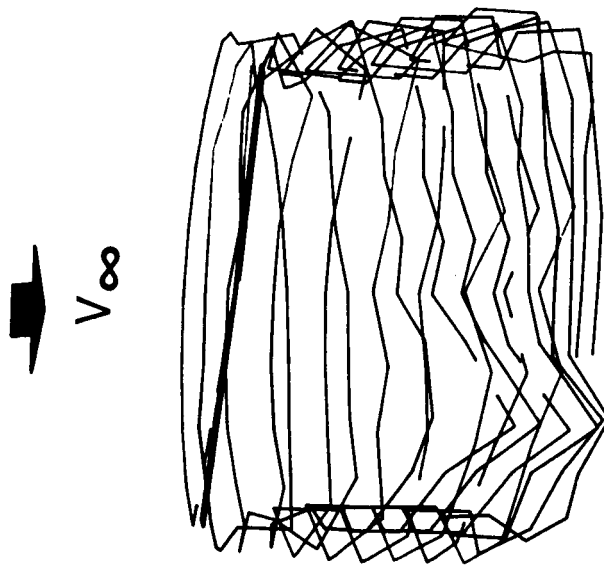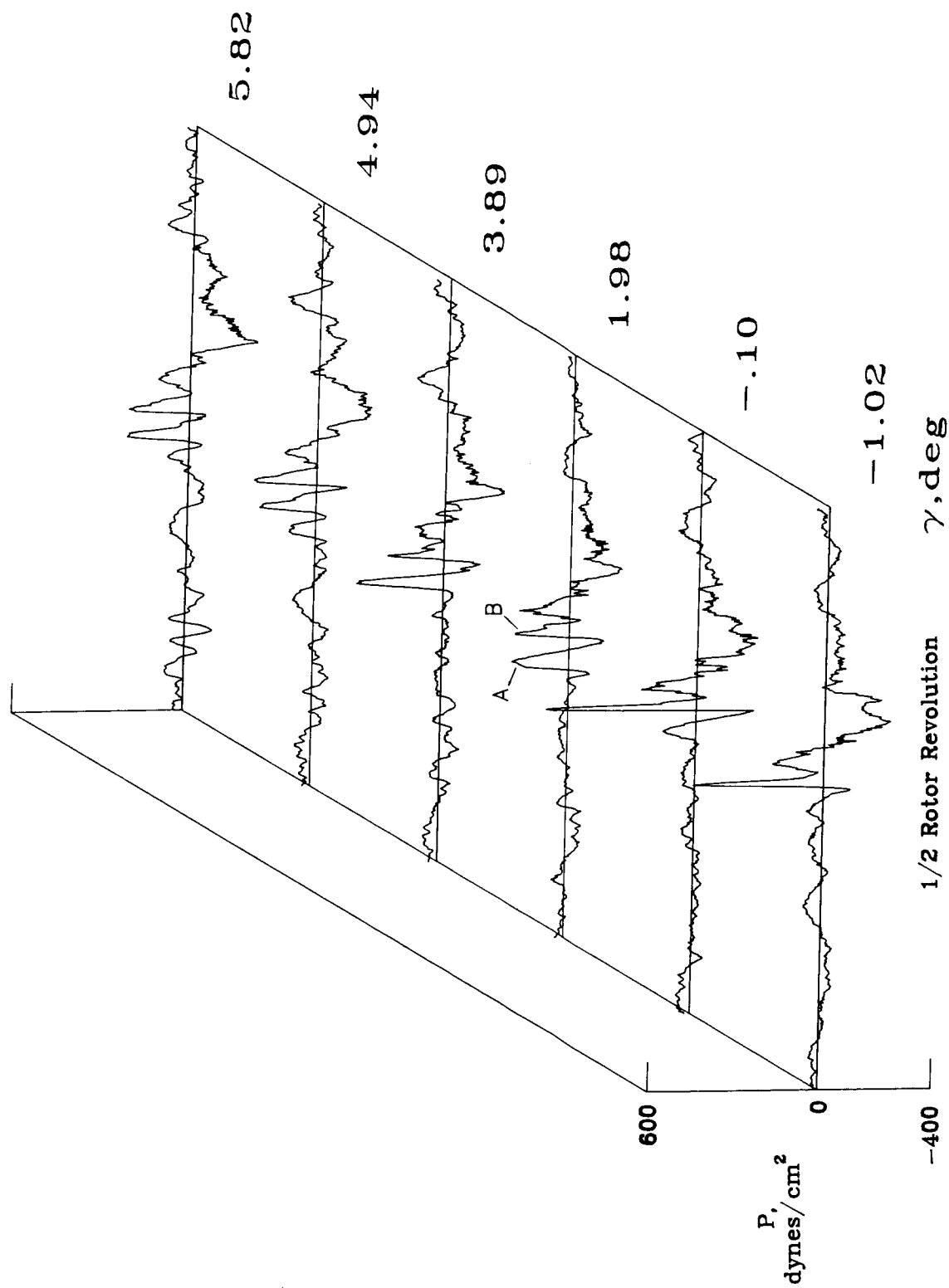
(b) View from directly behind and slightly above rotor.

Figure 8. Concluded.
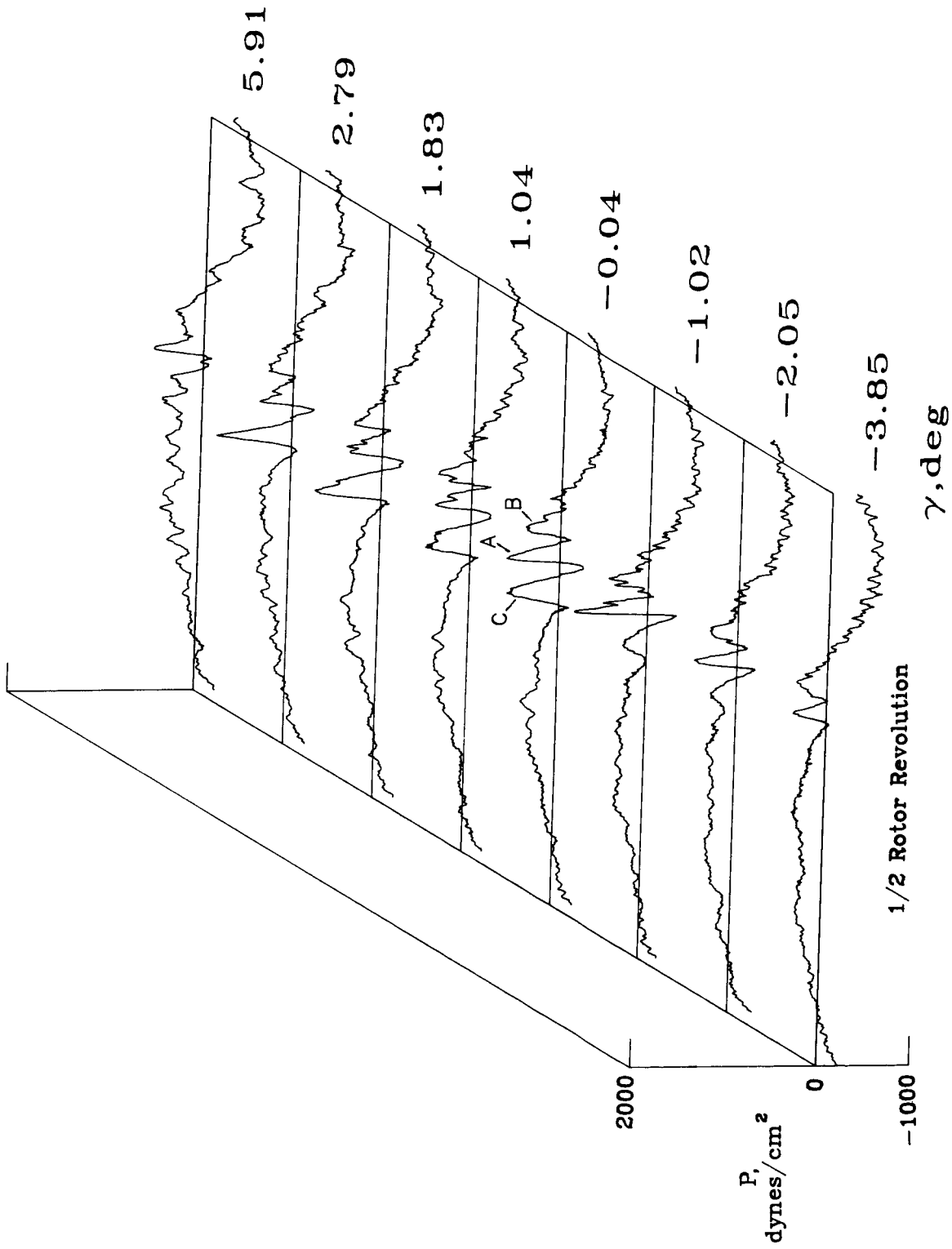
(a) Microphone 2.

Figure 9. Acoustic time history data for standard rotor sytem at $\mu = 0.124$ and $C_T = 0.00317$.

5.91

2.79

1.83

1.04

−0.04

−1.02

−2.05

−3.85

γ,deg

C

A
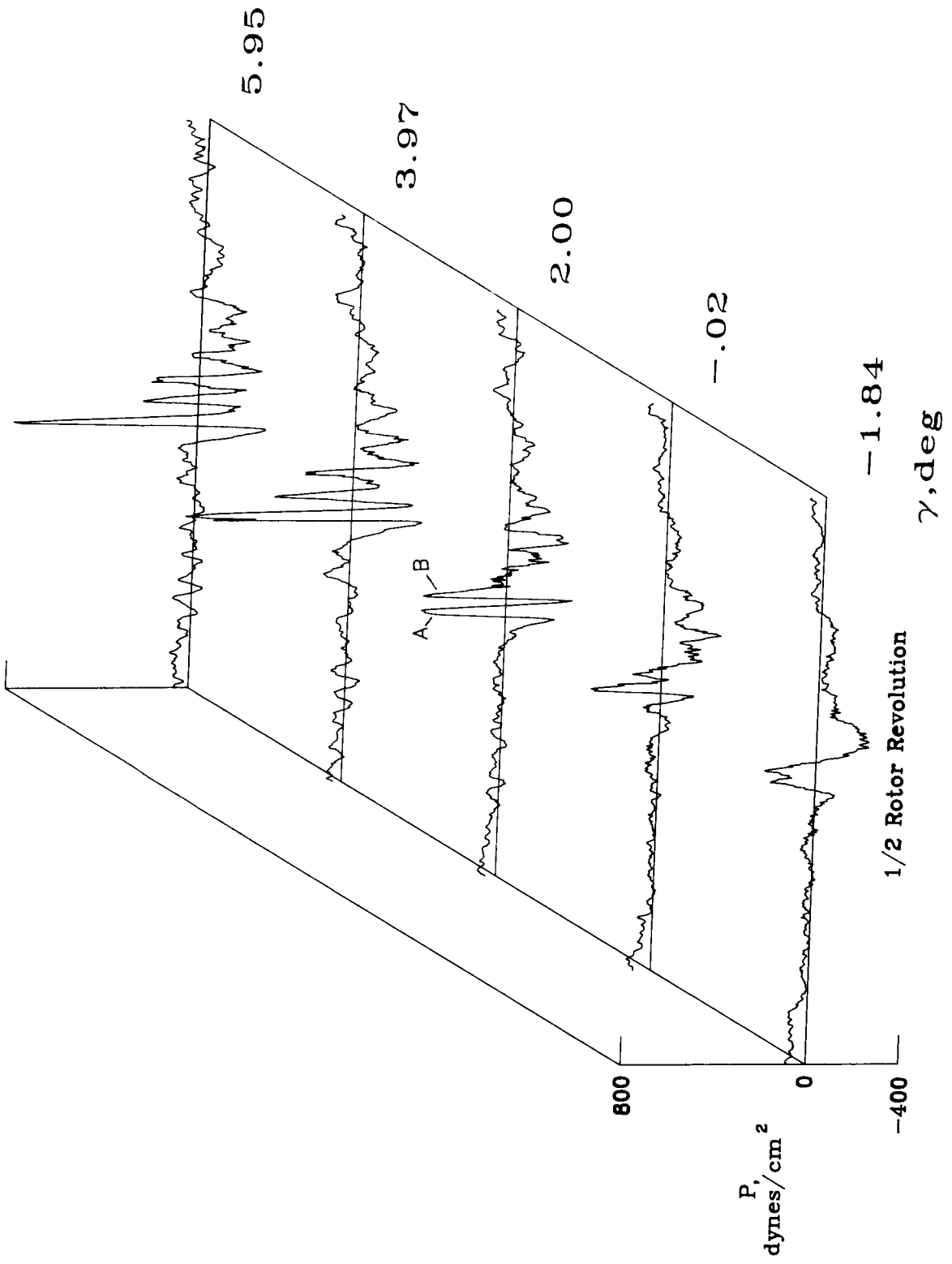
B

1/2 Rotor Revolution

P, dynes/cm²

1000

0

−1000
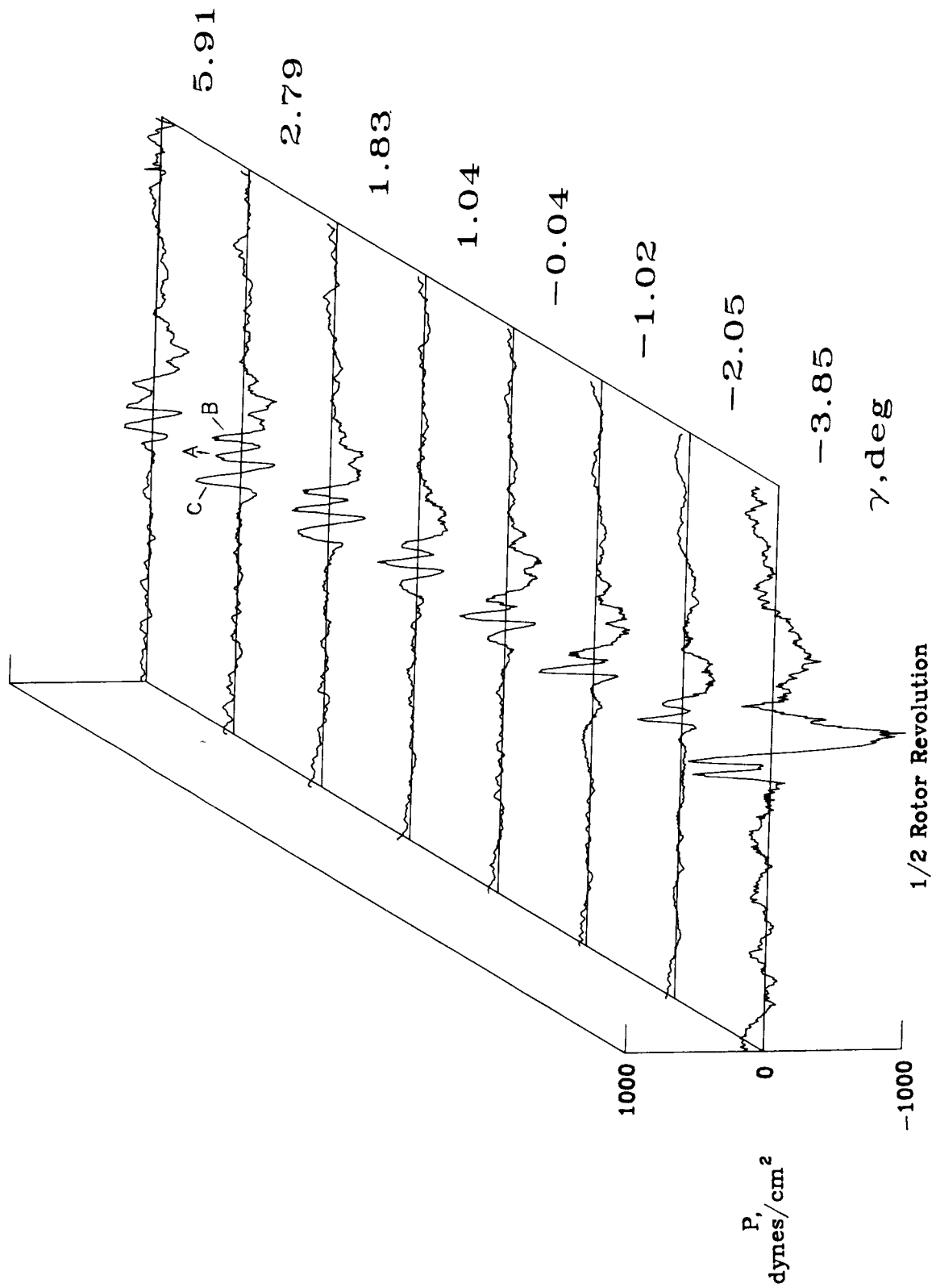
(b) Microphone 6.

Figure 9. Continued.
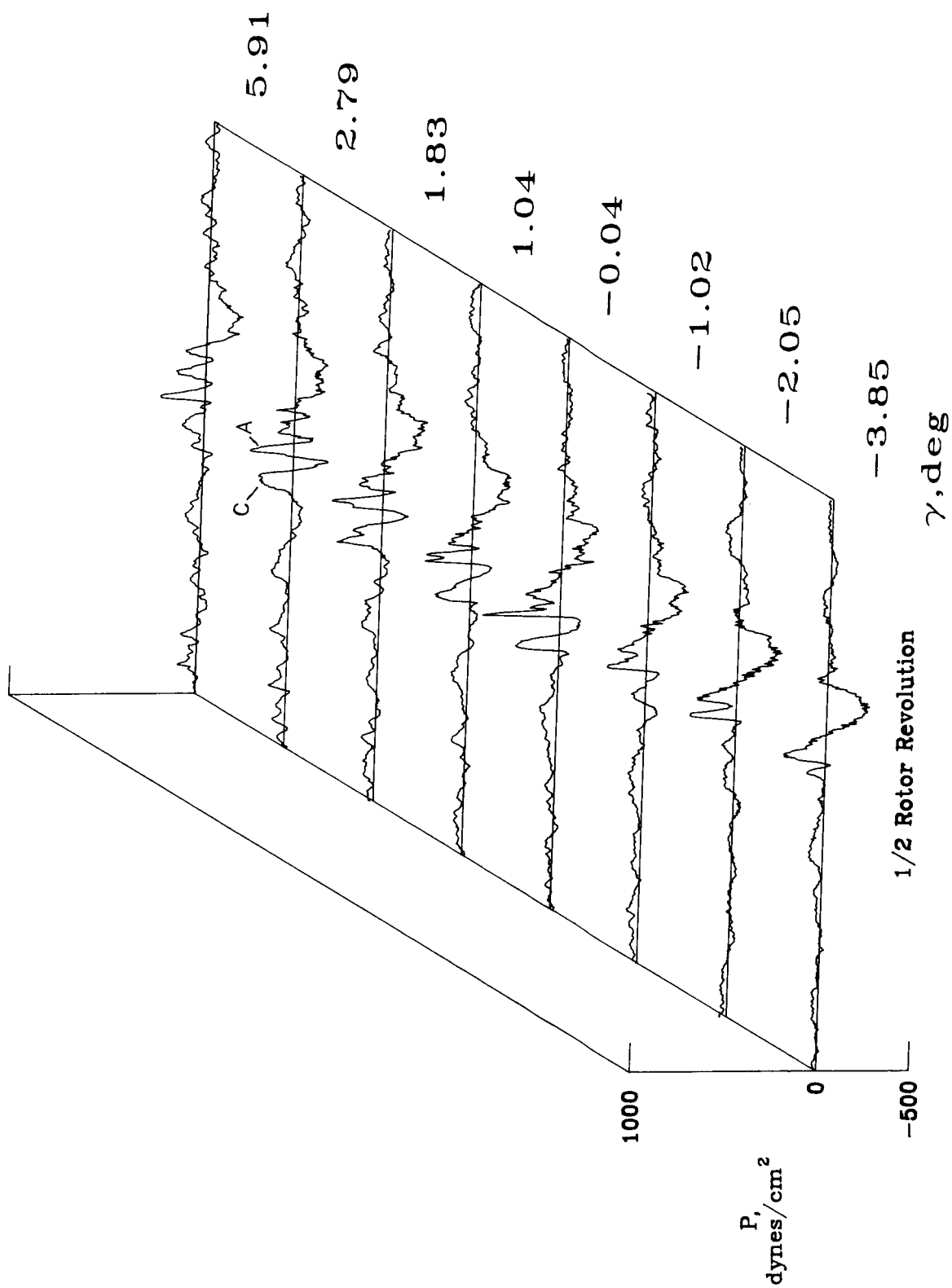
(c) Microphone 7.

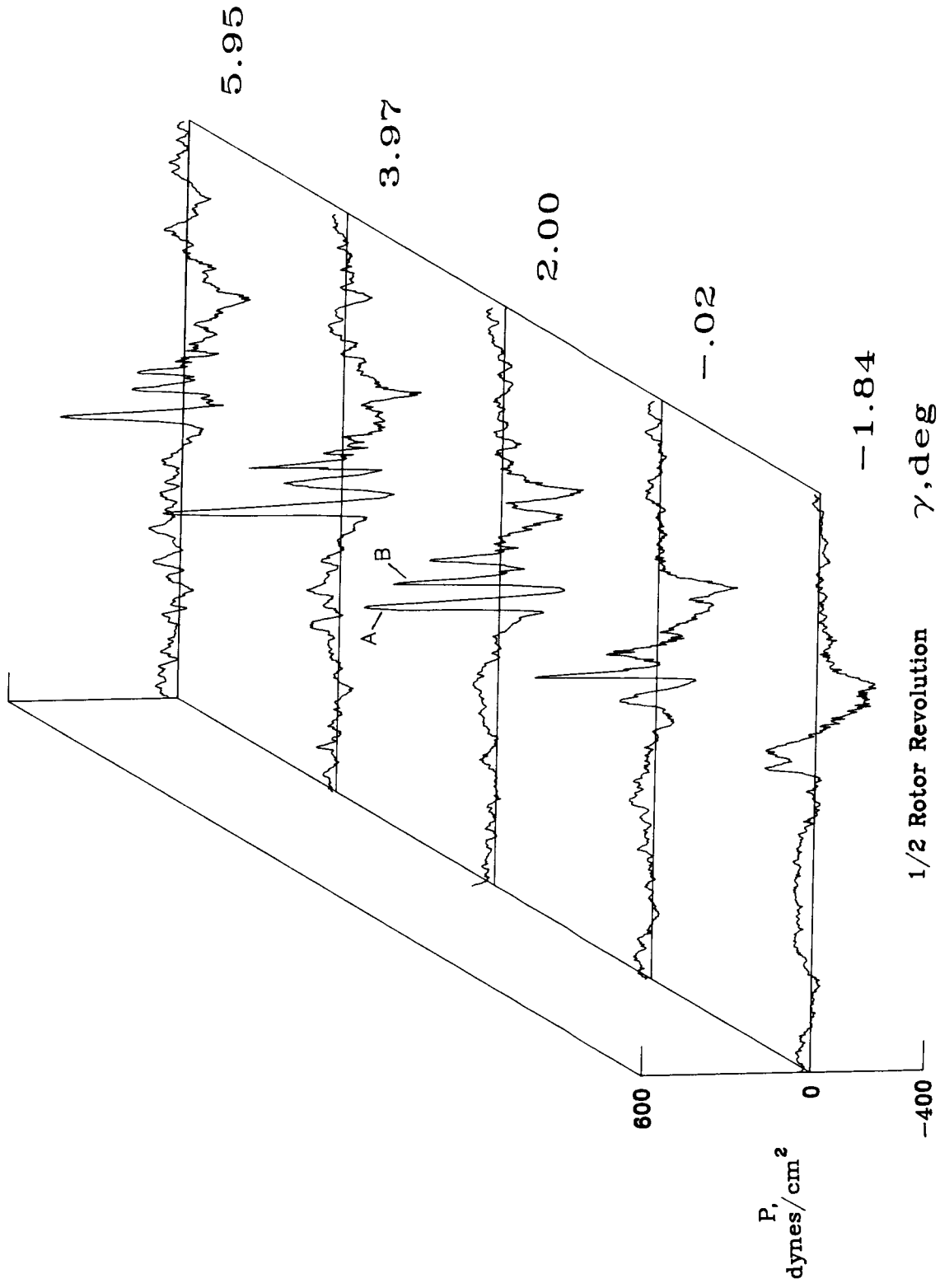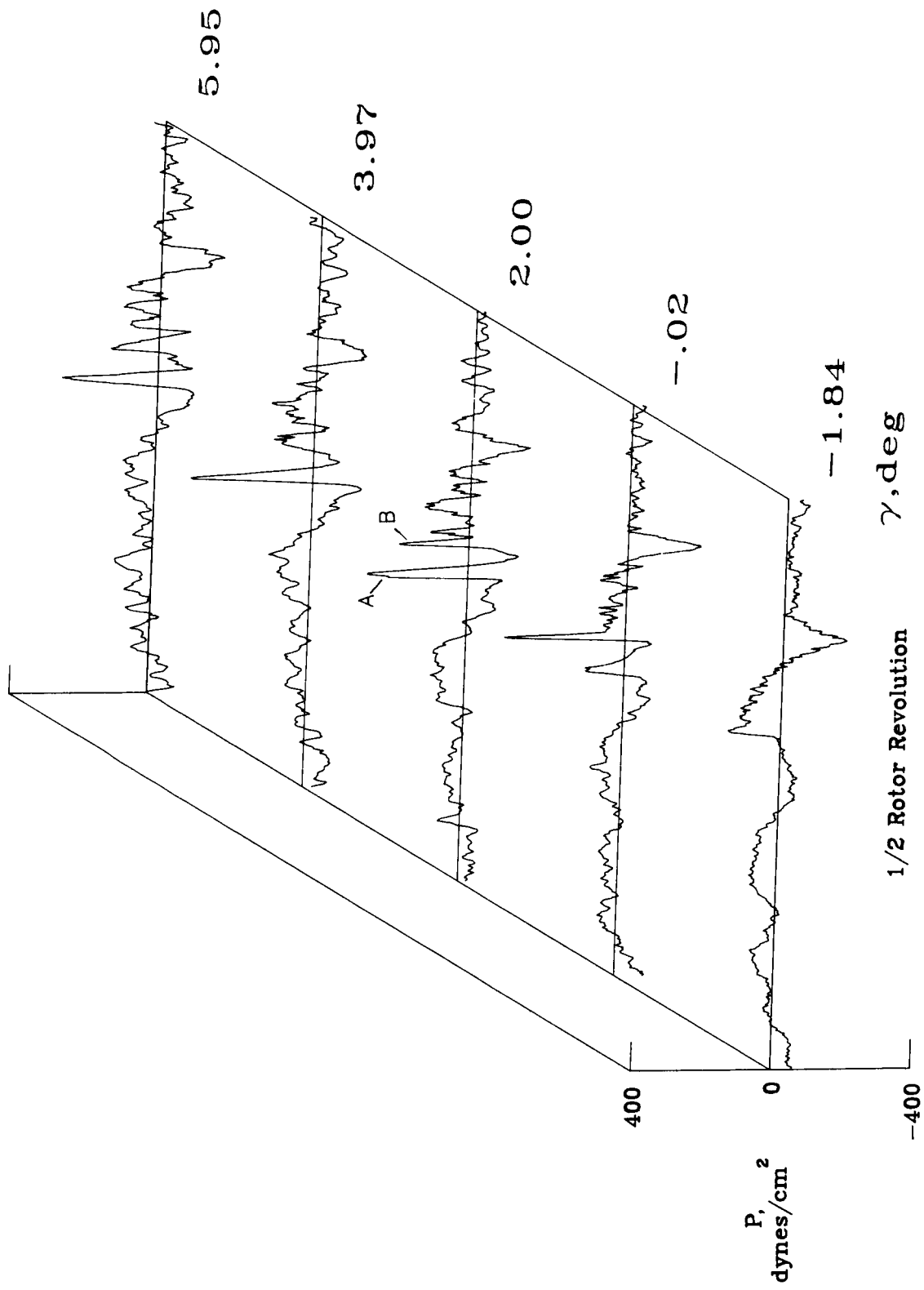Figure 9. Continued.
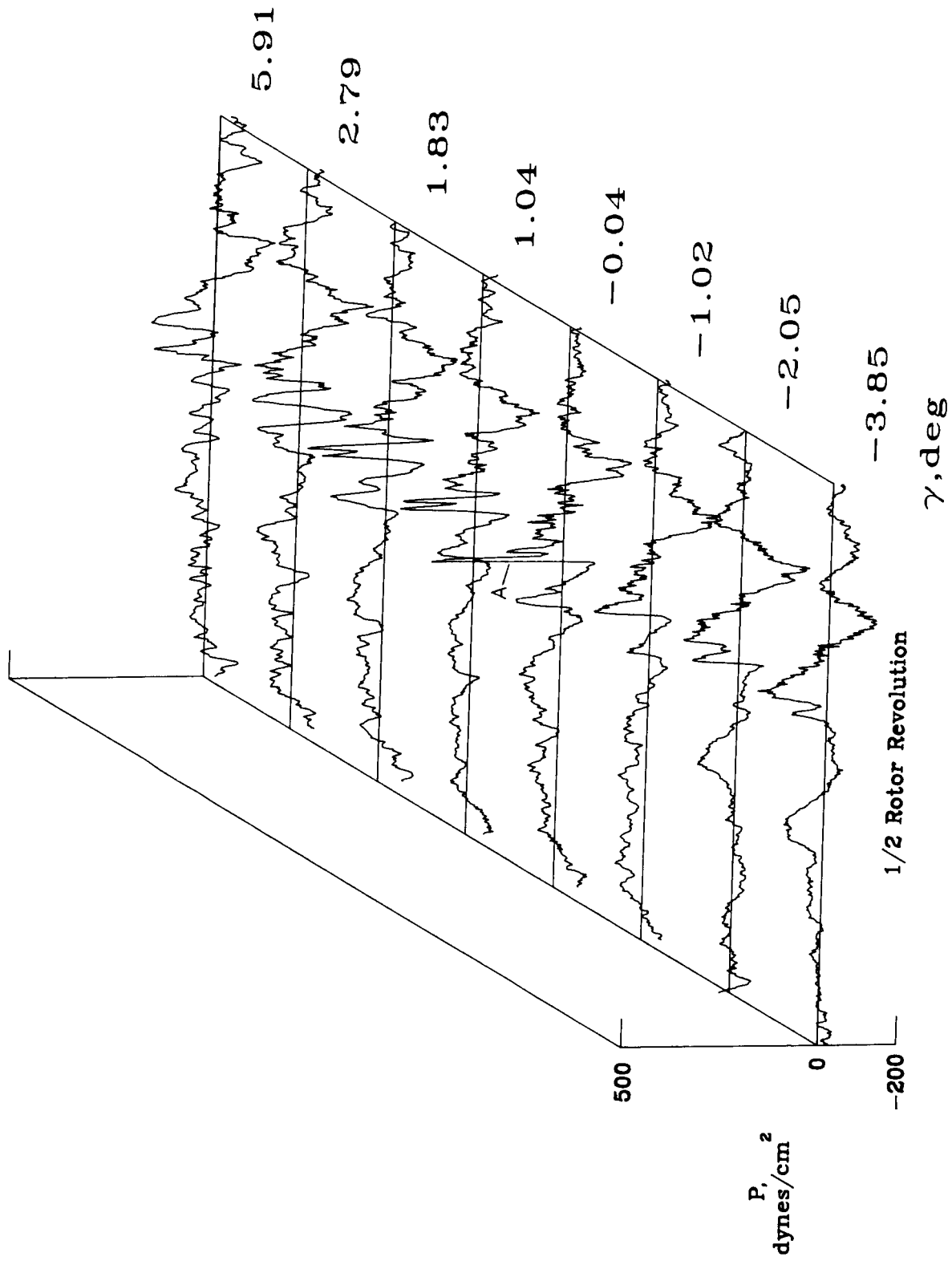
(d) Microphone 8.

Figure 9. Concluded.
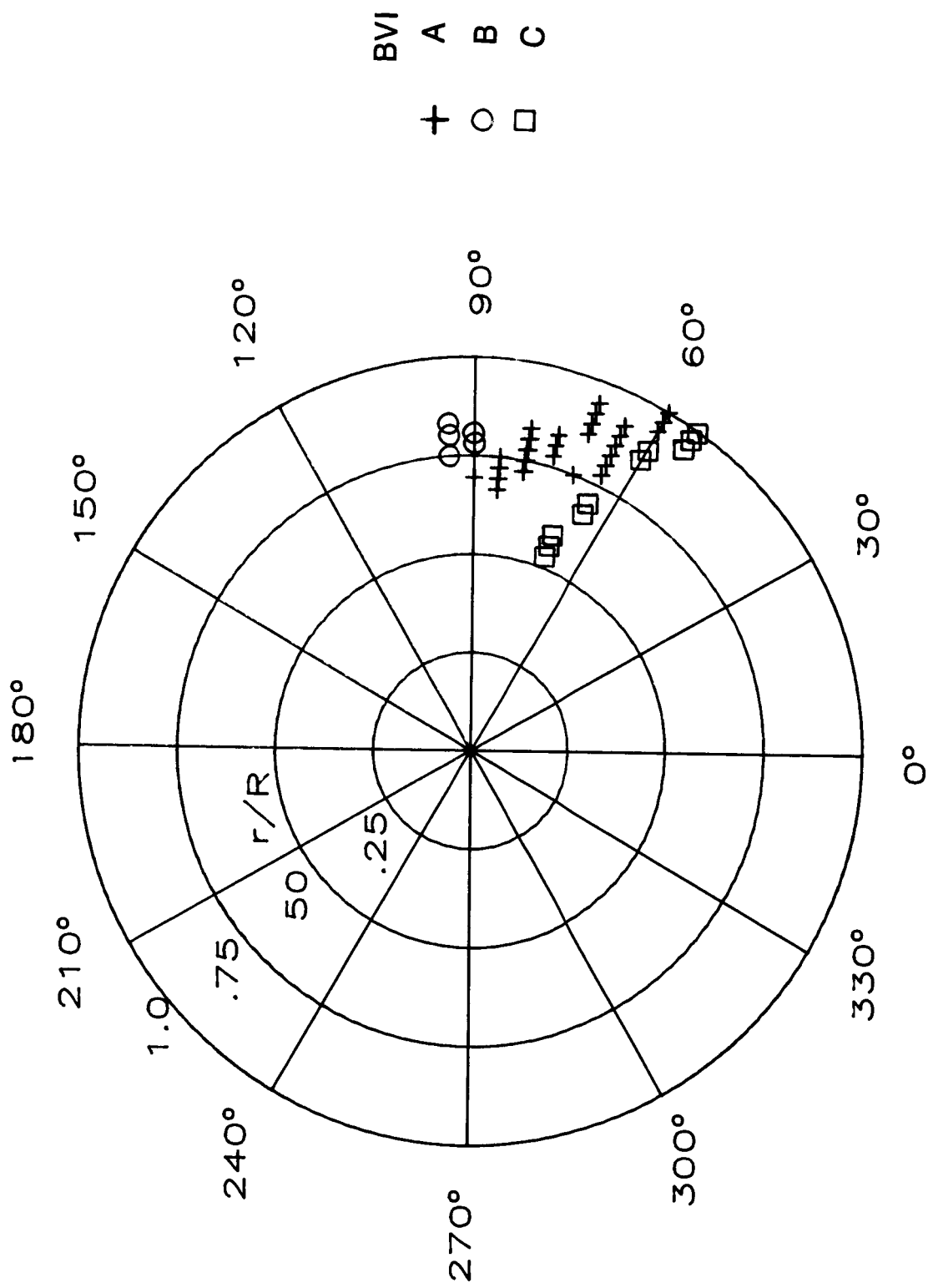
Figure 10. Source-location results for standard rotor system with $\mu = 0.124$ and $C_T = 0.00317$.
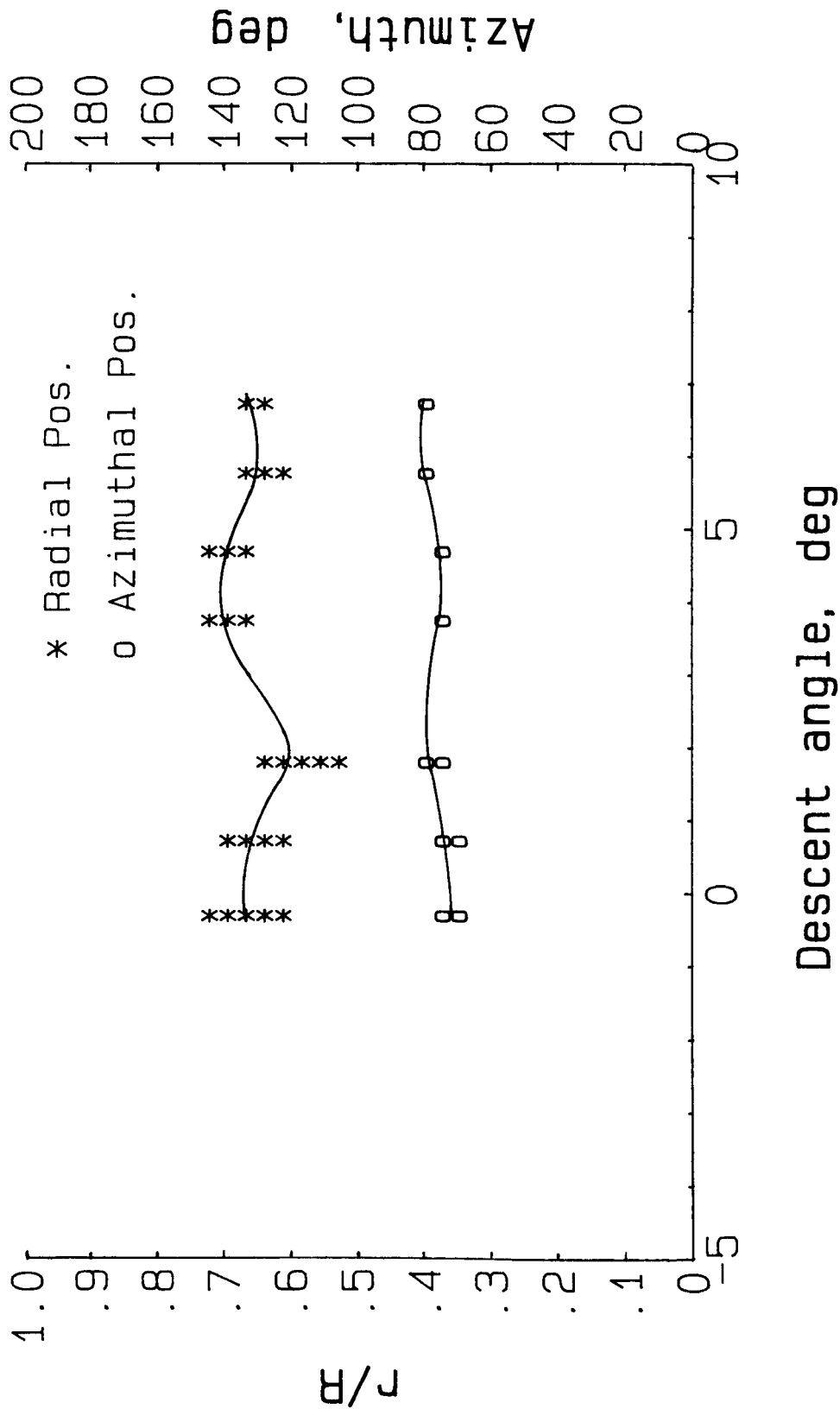
Figure 11. Example of variation of BVI source location with descent angle for standard rotor system. Impulse A; $\mu = 0.104$; $C_T = 0.00313$.
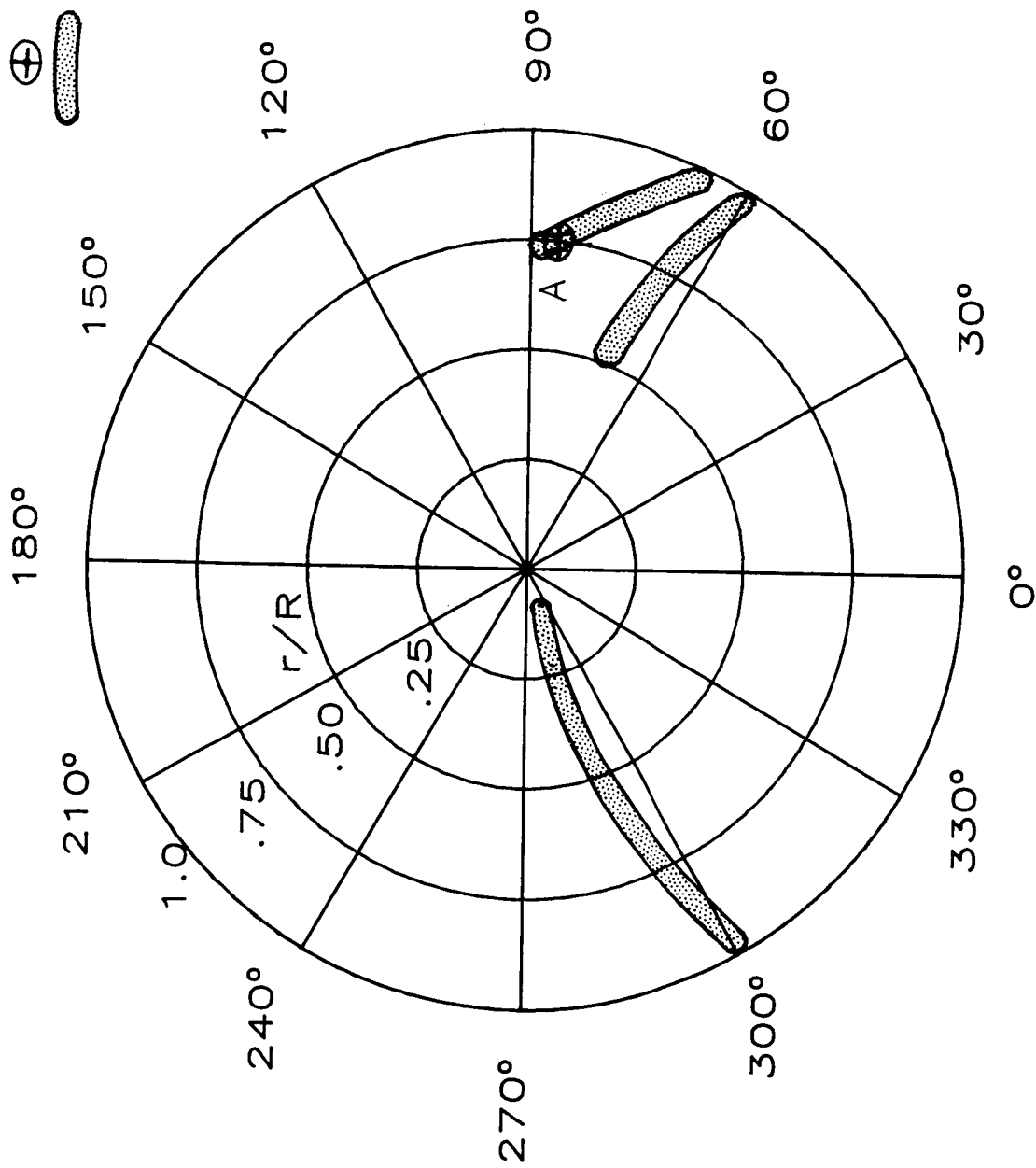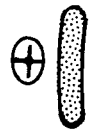
Figure 12. Source locations of BVI for standard rotor system computed from acoustic data and predicted with free-wake analysis.

(a) $\mu = 0.124$; $C_T = 0.00314$; $\gamma = -2.05°$.

25
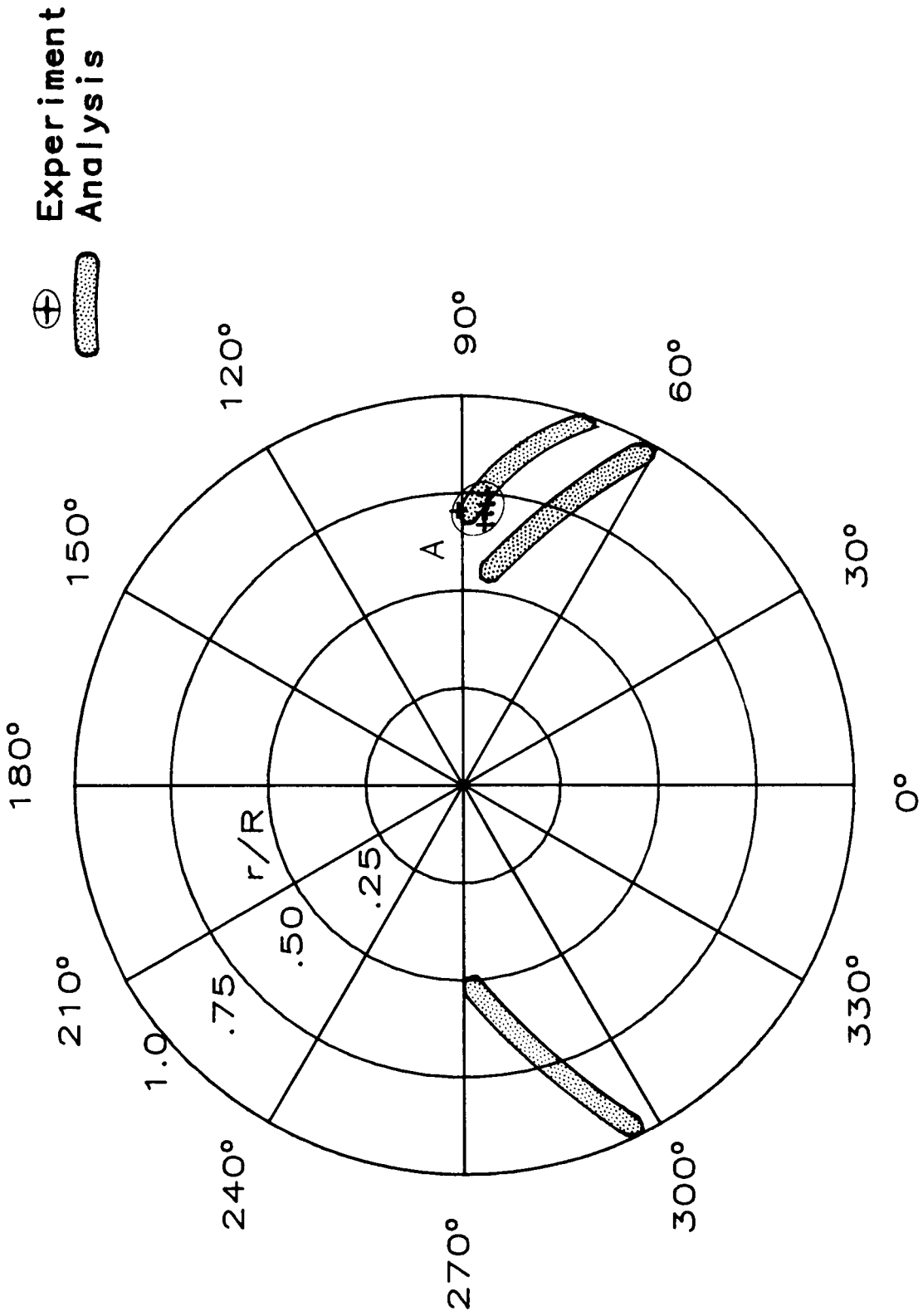
(b) $\mu = 0.124$; $C_T = 0.00314$; $\gamma = -1.02°$.

Figure 12. Continued.
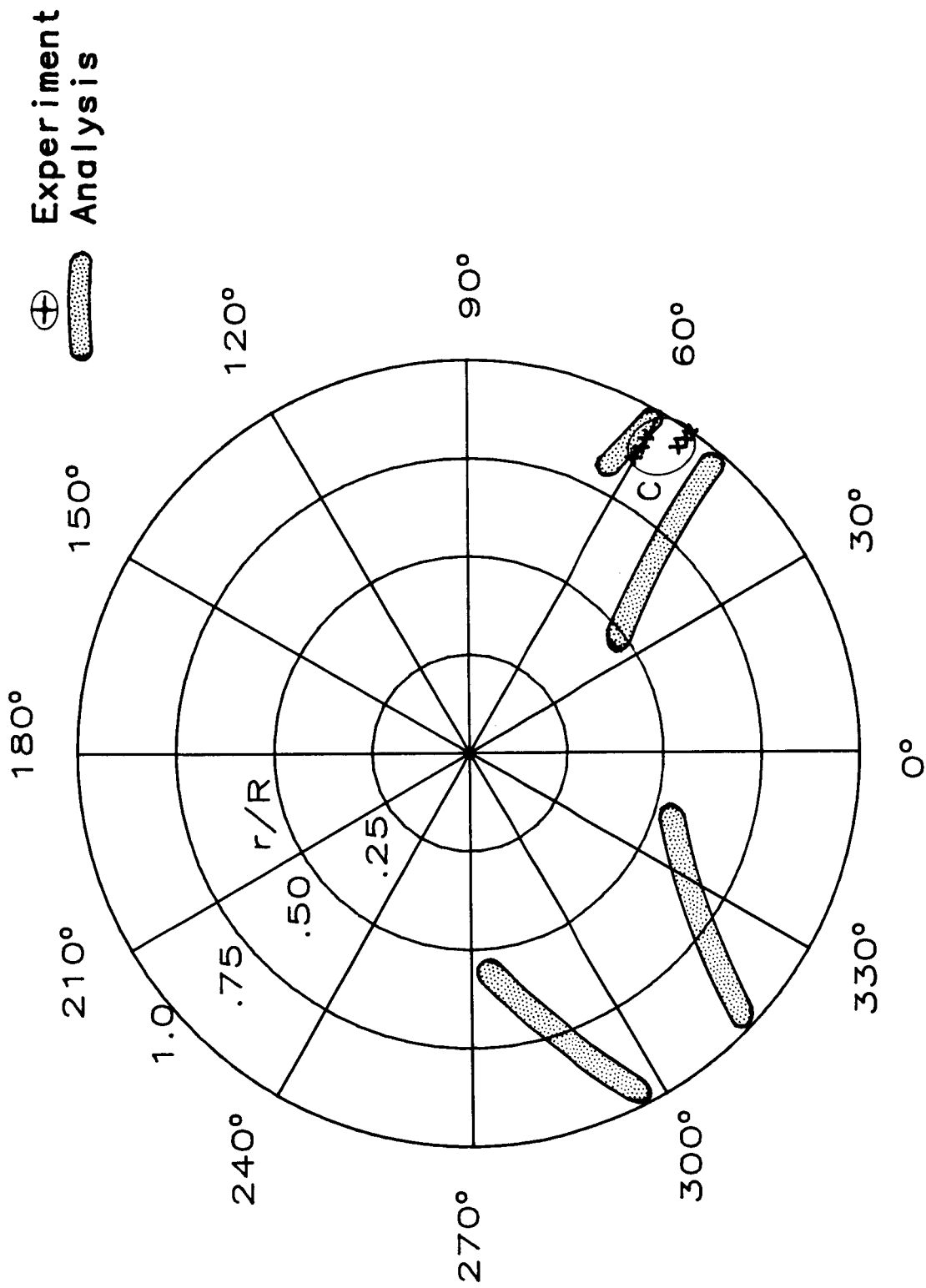
(c) $\mu = 0.124$; $C_T = 0.00319$; $\gamma = 1.83°$.

Figure 12. Continued.
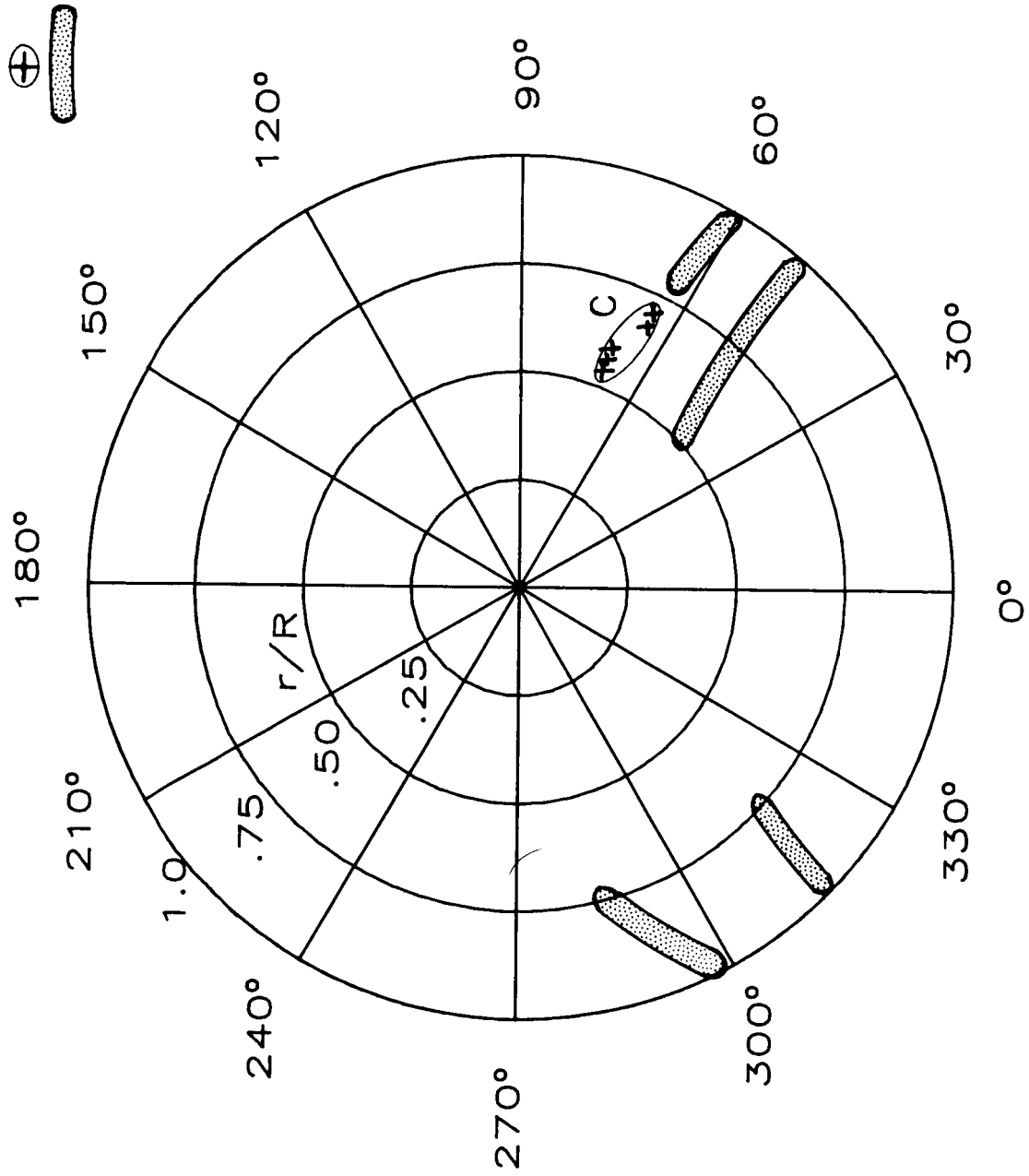
(d) $\mu = 0.124$; $C_T = 0.00317$; $\gamma = 2.79°$.

Figure 12. Concluded.
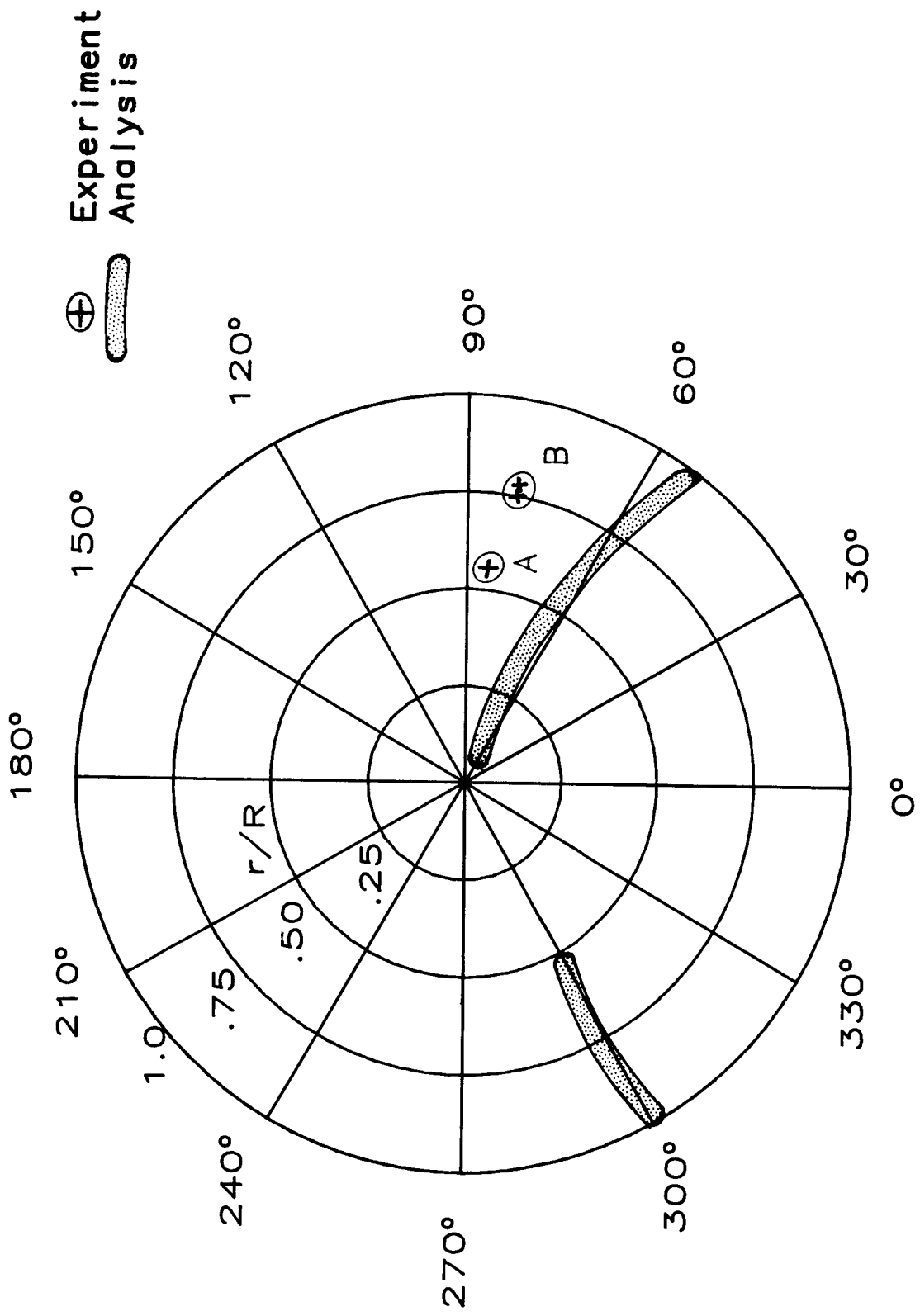
(a) $\mu = 0.146$; $C_T = 0.00304$; $\gamma = -1.28°$.

Figure 13. Source locations of BVI for advanced rotor sytem computed from acoustic data and predicted with free-wake analysis.
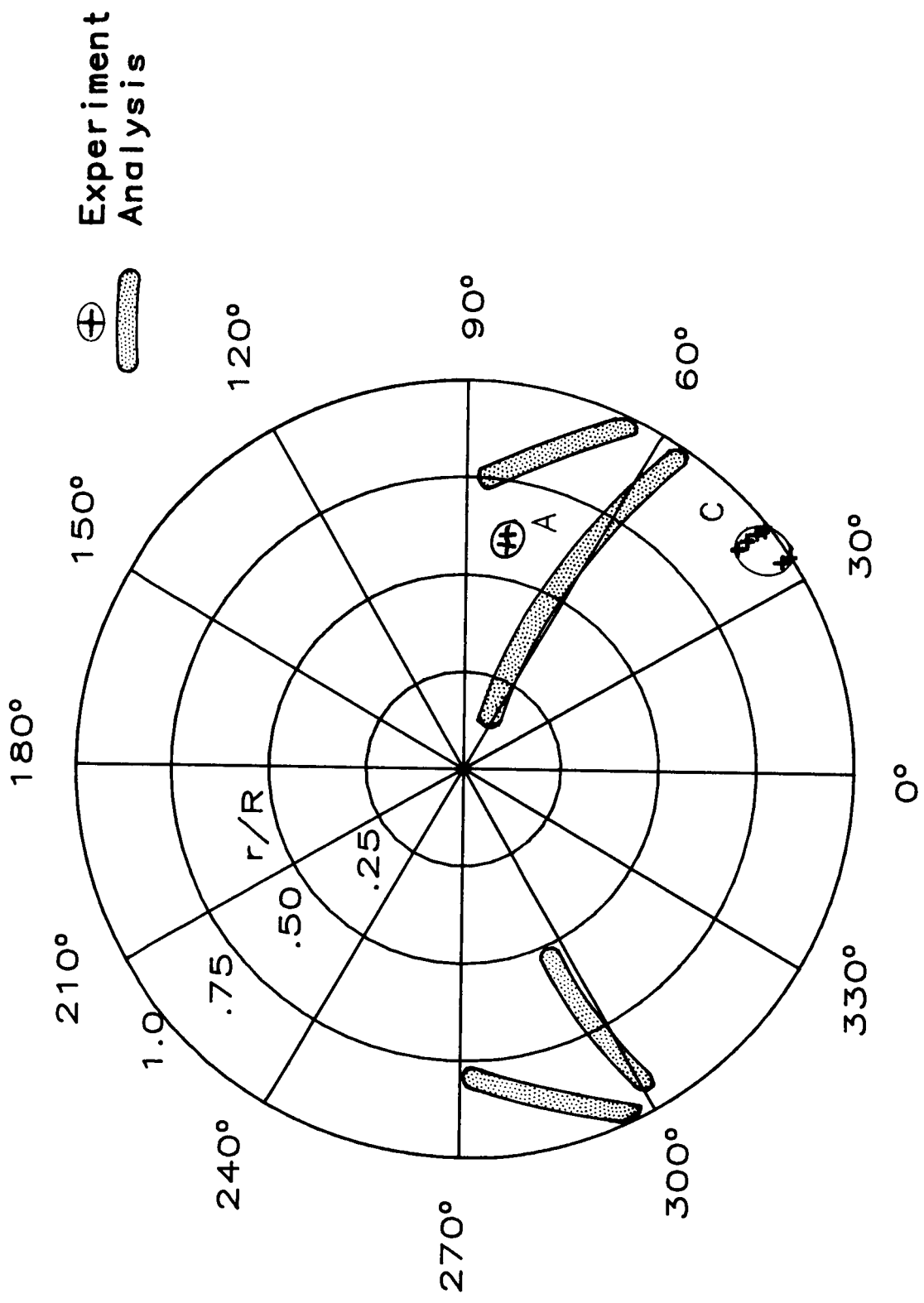
(b) $\mu = 0.146$; $C_T = 0.00310$; $\gamma = 3.56°$.

Figure 13. Continued.
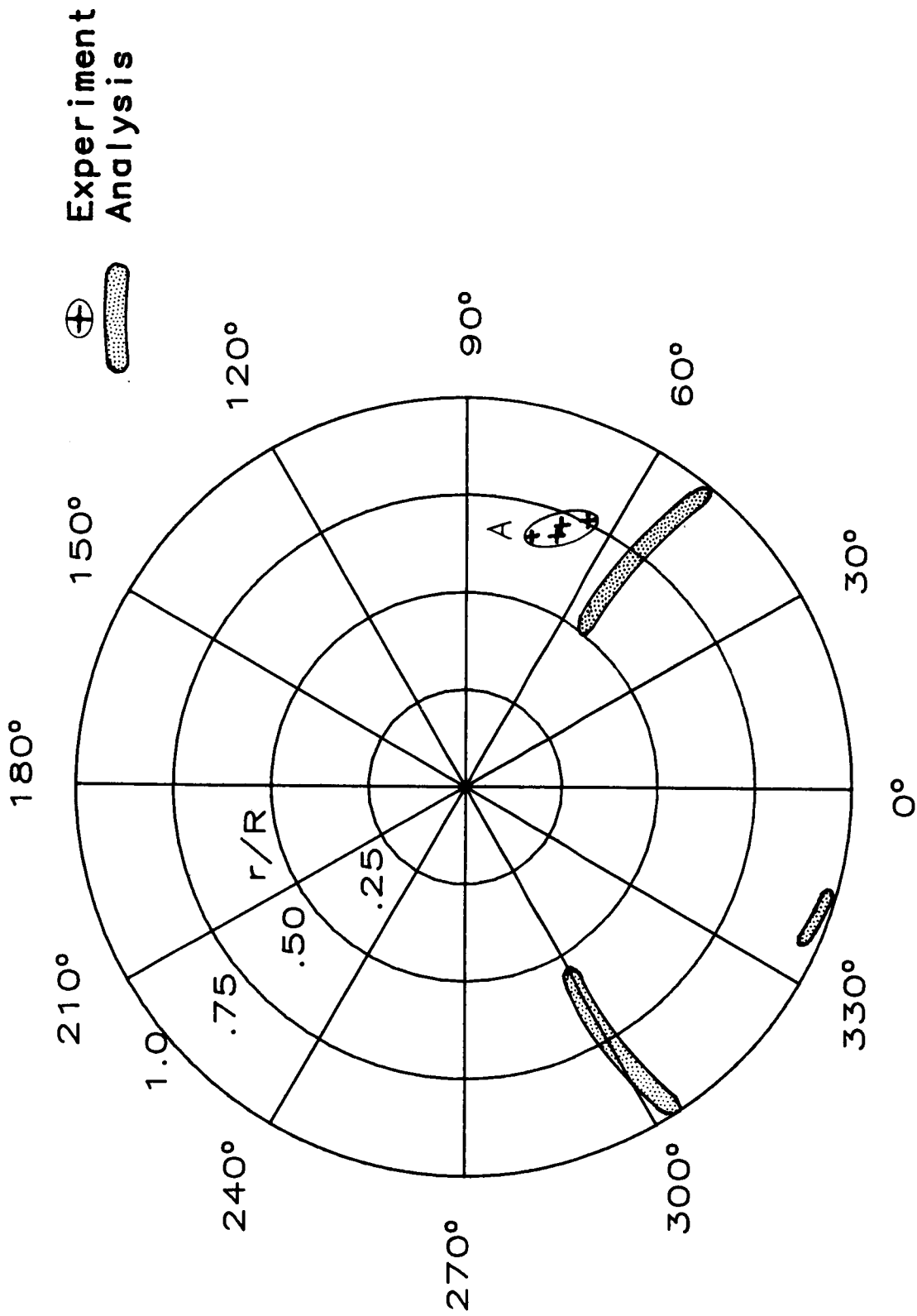
(c) $\mu = 0.157$; $C_T = 0.00319$; $\gamma = 1.42°$.

Figure 13. Continued.
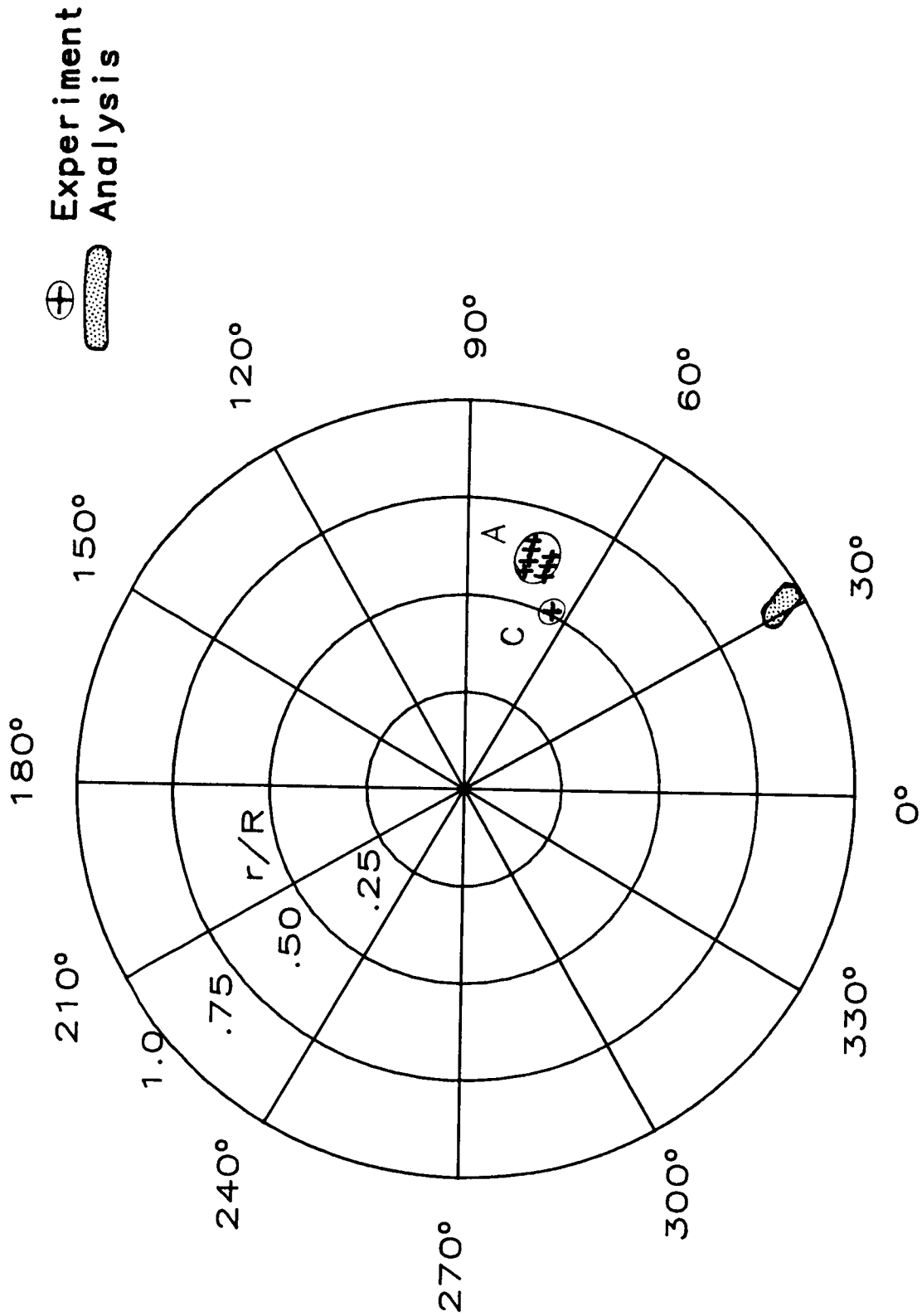
(d) $\mu = 0.157$; $C_T = 0.00324$; $\gamma = 5.42°$.

Figure 13. Concluded.
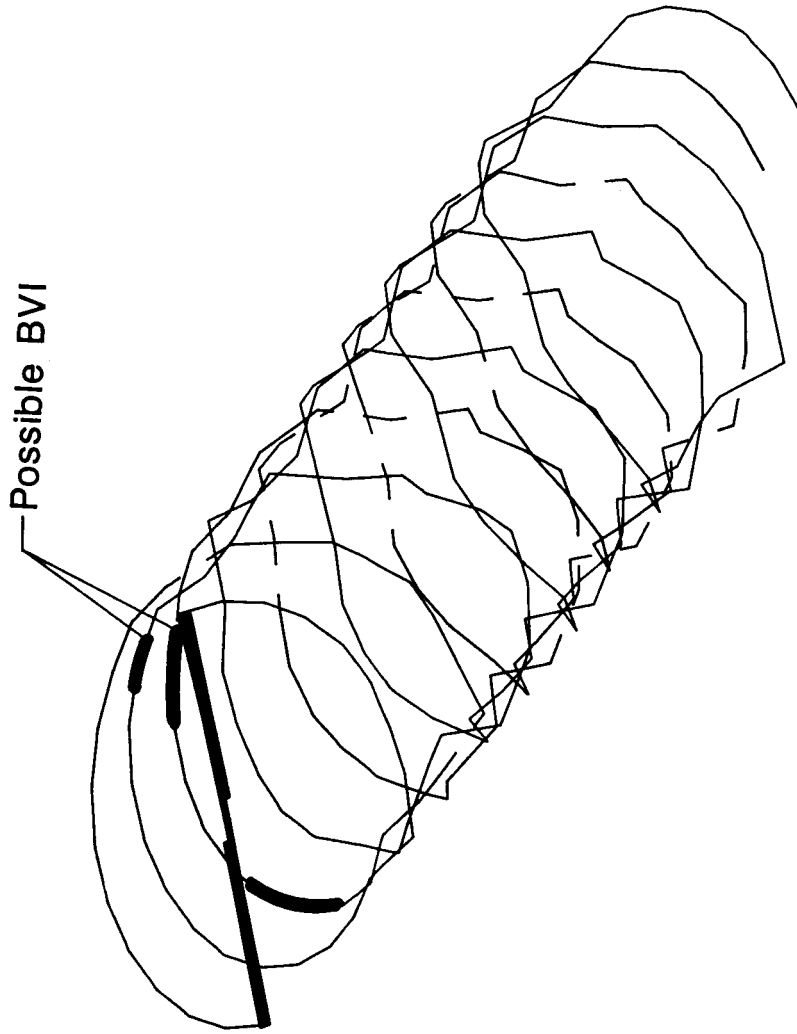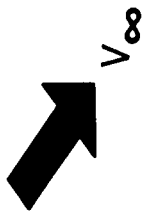
Figure 14. Rotor-wake geometry predicted for standard rotor system at $\mu = 0.124$, $C_T = 0.00314$, and $\gamma = -2.05$.

33
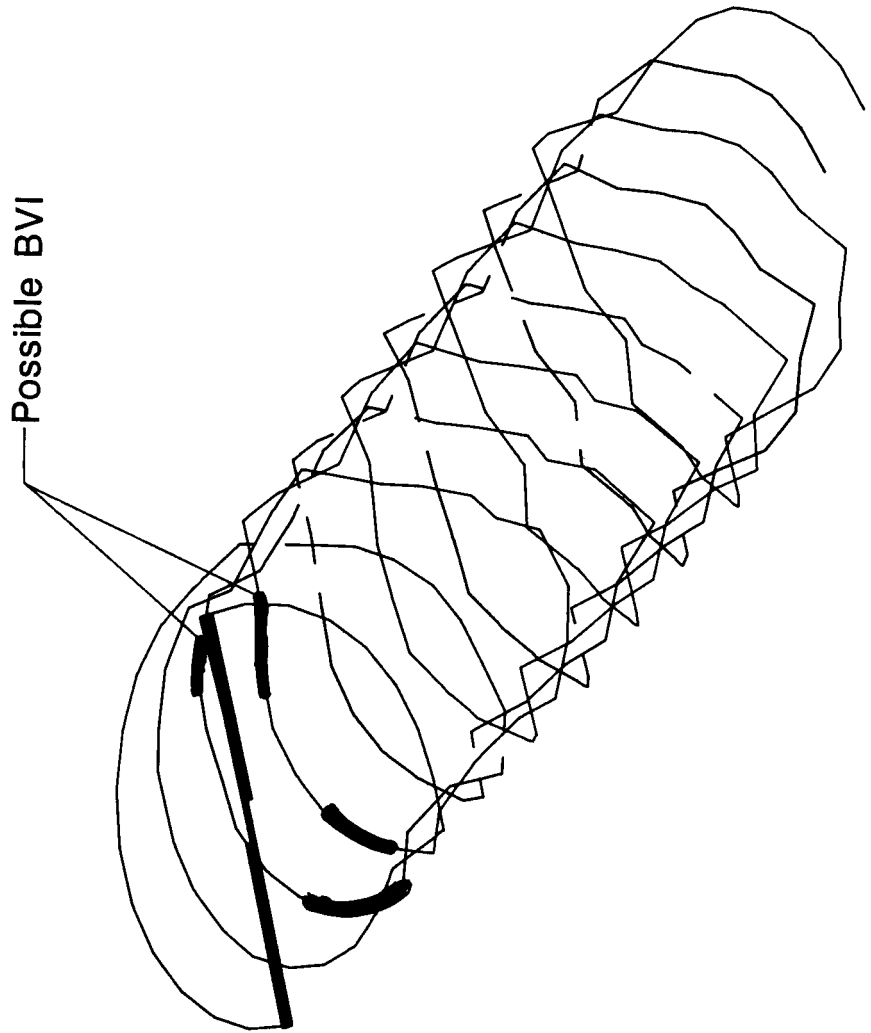
Figure 15. Rotor-wake geometry predicted for standard rotor system at $\mu = 0.124$, $C_T = 0.00319$, and $\gamma = 1.83°$.

Appendix

Acoustic Data and Source Location

The acoustic data and results of source-location calculations presented in this report are grouped into two categories—cascade-style plots of time histories for selected microphones and rotor test conditions (figs. A1 to A11) and the complete set of source-location results for both rotors and for all test conditions at which distinct blade-vortex interaction (BVI) was discernible (figs. A12 and A13). The arrangement of the data plots is in the following format:

The time history cascade plots are presented in a manner which shows the variation of the time history for $1/2$ revolution as the simulated descent angle is varied from a climb condition to a large descent value. For clarity in the figures, not all the data collected that were usable in the source-location calculations are presented. In each part of figures A1 to A11, BVI impulses have been identified as A, B, or C. These particular impulses are also specifically identified in the polar coordinate plots of the source-location data in figures A12 and A13.

The source-location data in figures A12 and A13 are presented in polar coordinate form, where the $0°$ azimuth is the position in the rotor disk as viewed from above the tail of the helicopter. The symbols plotted are for BVI impulses throughout the range of descent angles at that particular advance ratio and thrust coefficient. For instance, in figure A12(a), BVI impulses A and B are the direct results of the calculations from the propagation time measurements for BVI impulses A and B in figures A1(a) to A1(c).
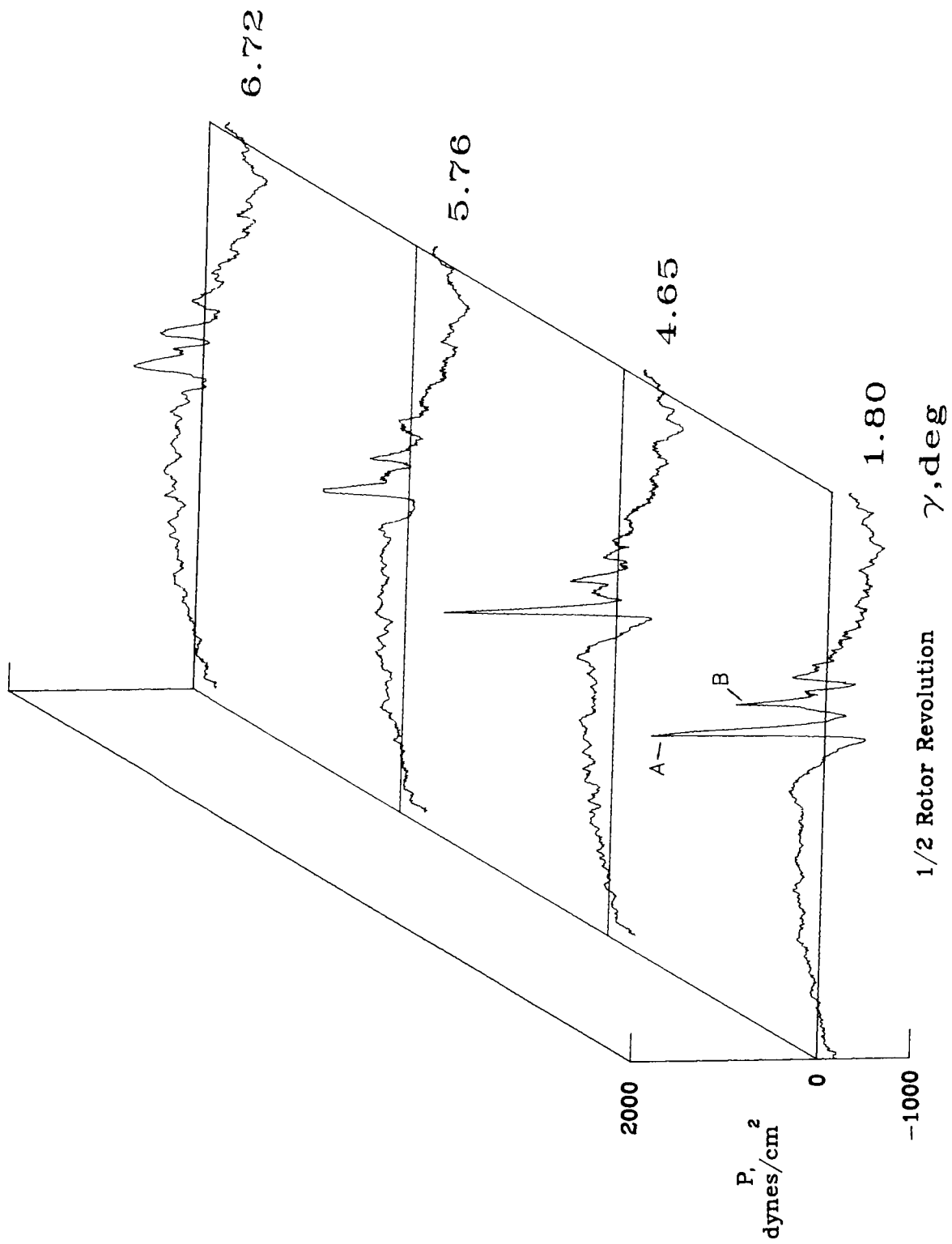
(a) Microphone 2.

Figure A1. Acoustic time history data for standard rotor sytem at $\mu = 0.104$ and $C_T = 0.00313$.

36
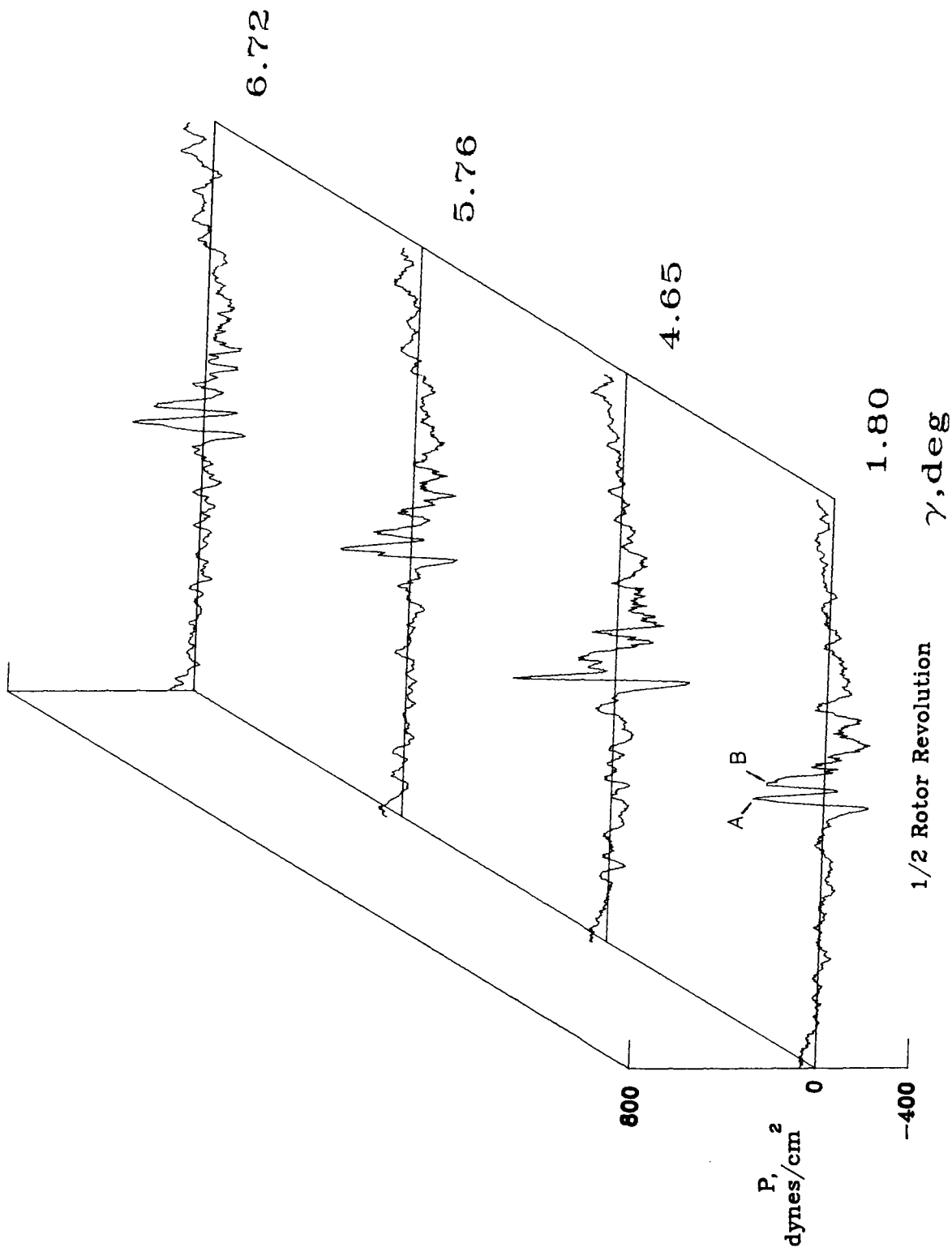
(b) Microphone 6.

Figure A1. Continued.
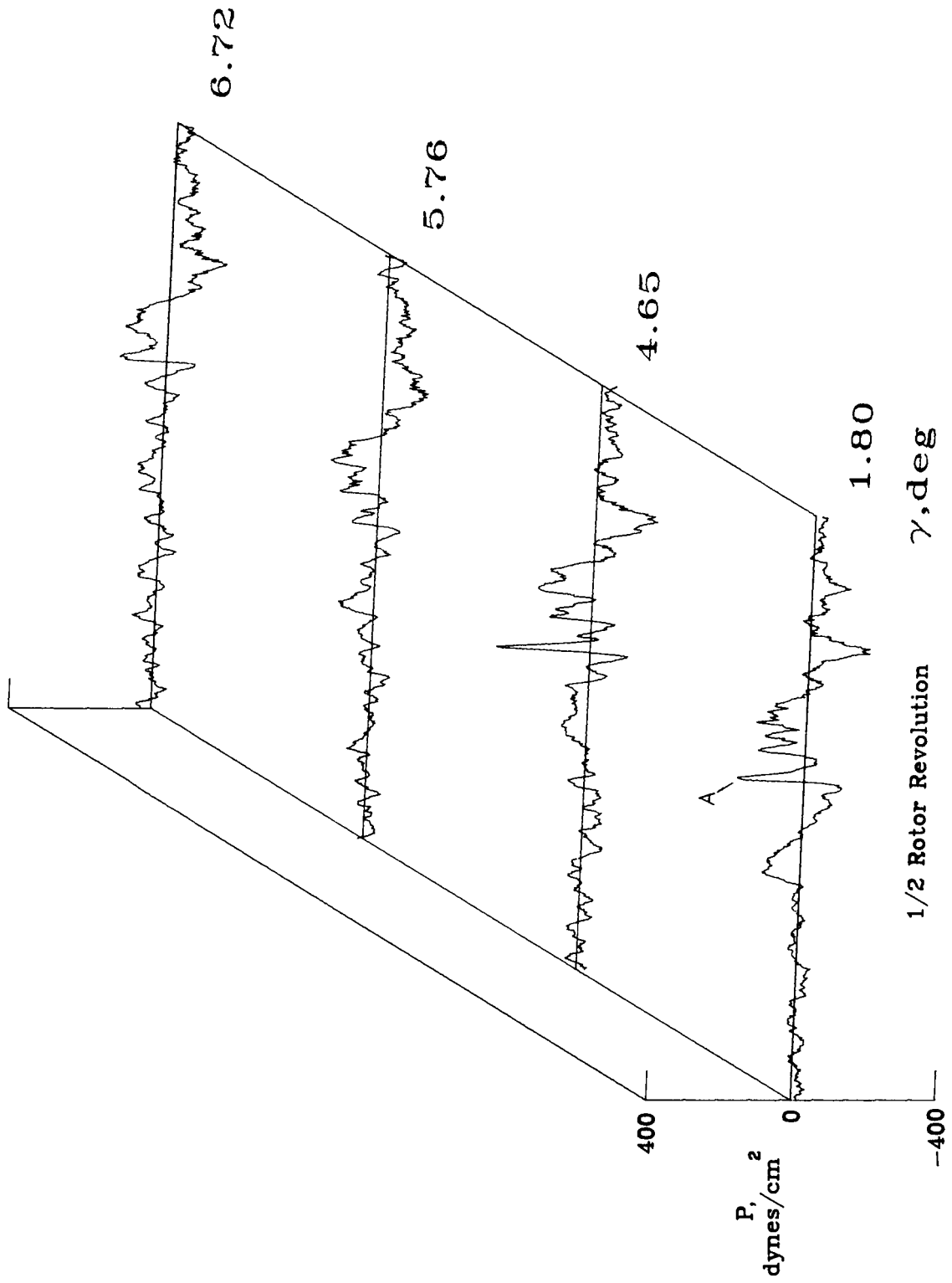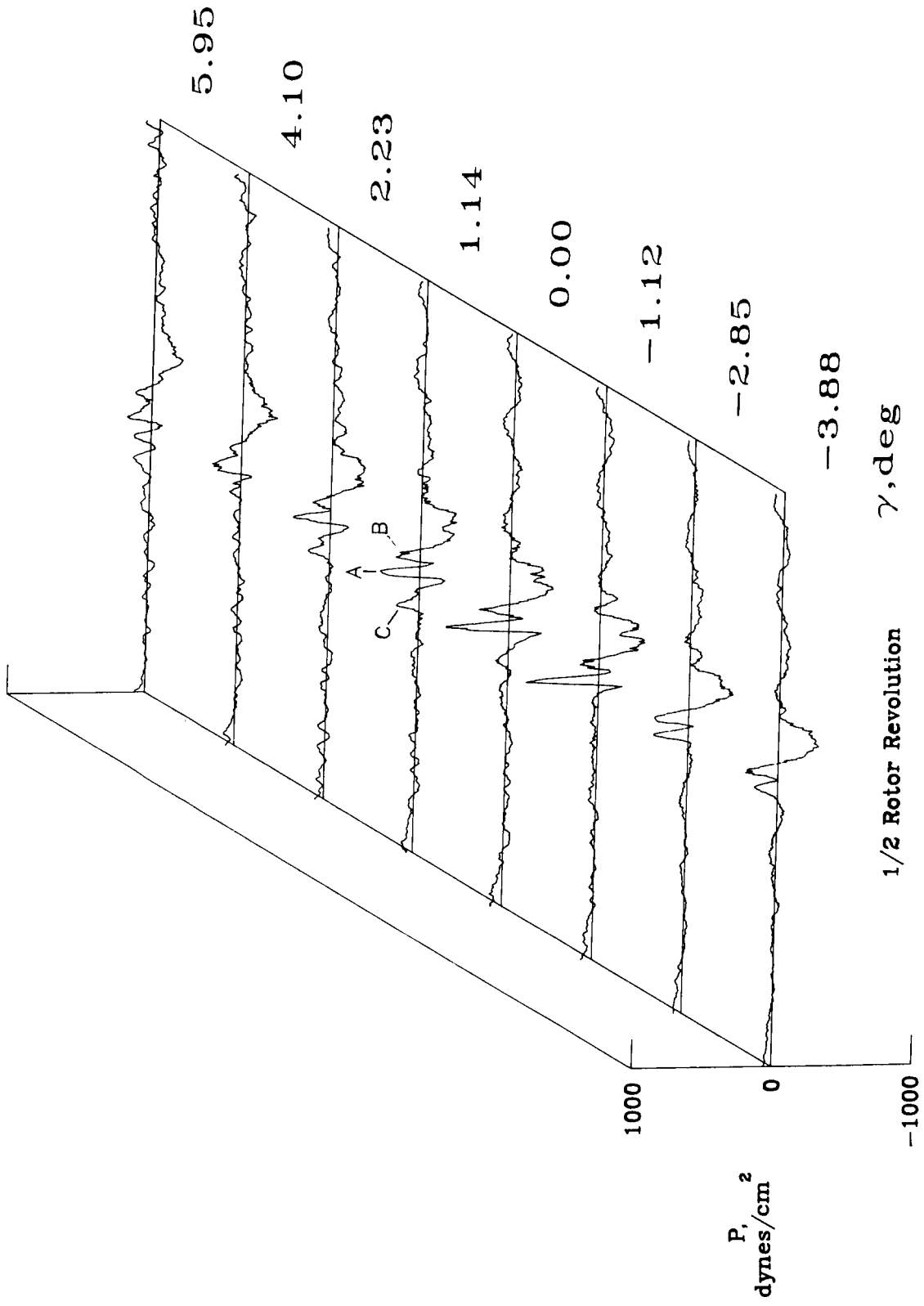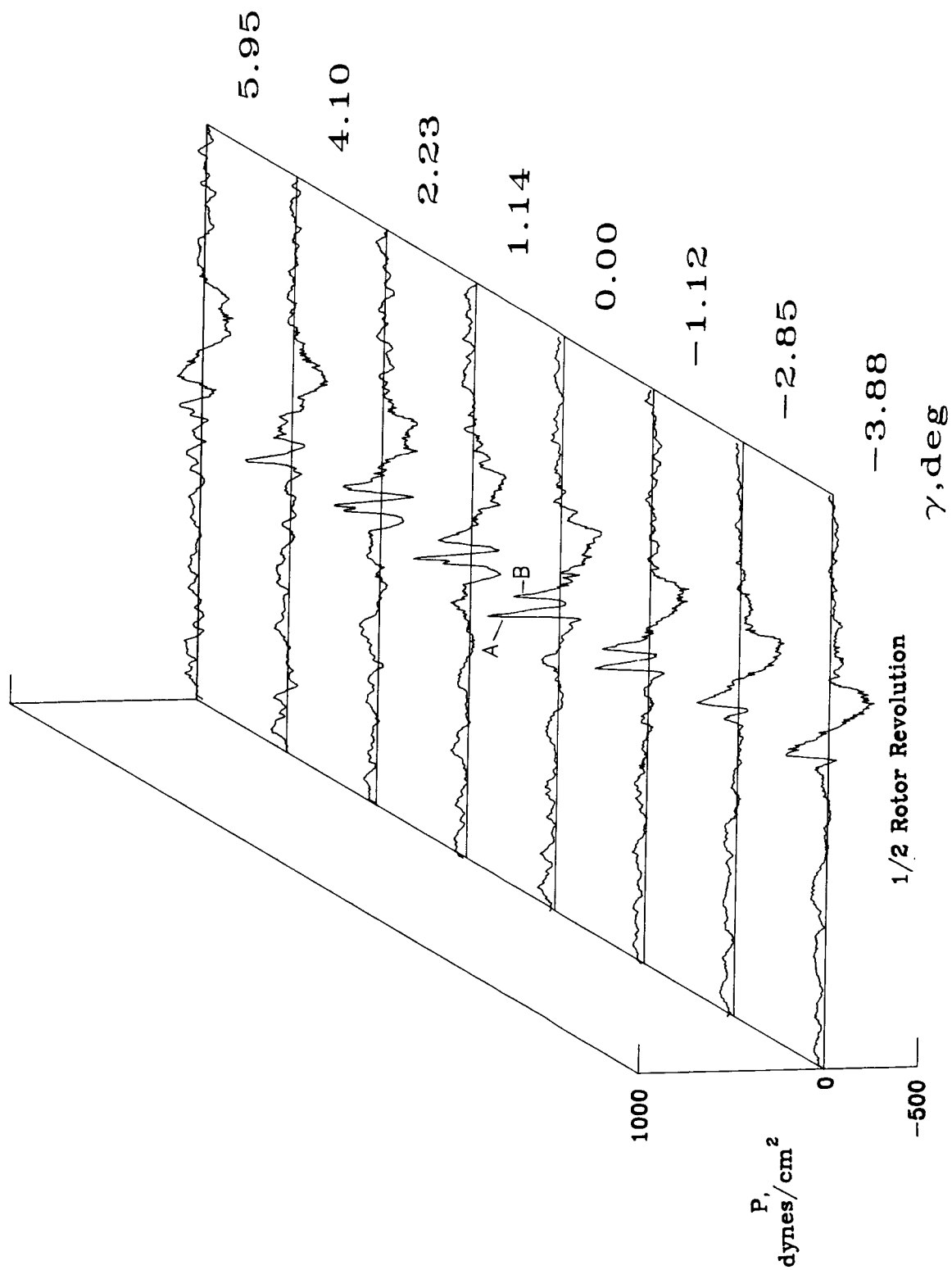
(c) Microphone 8.

Figure A1. Concluded.
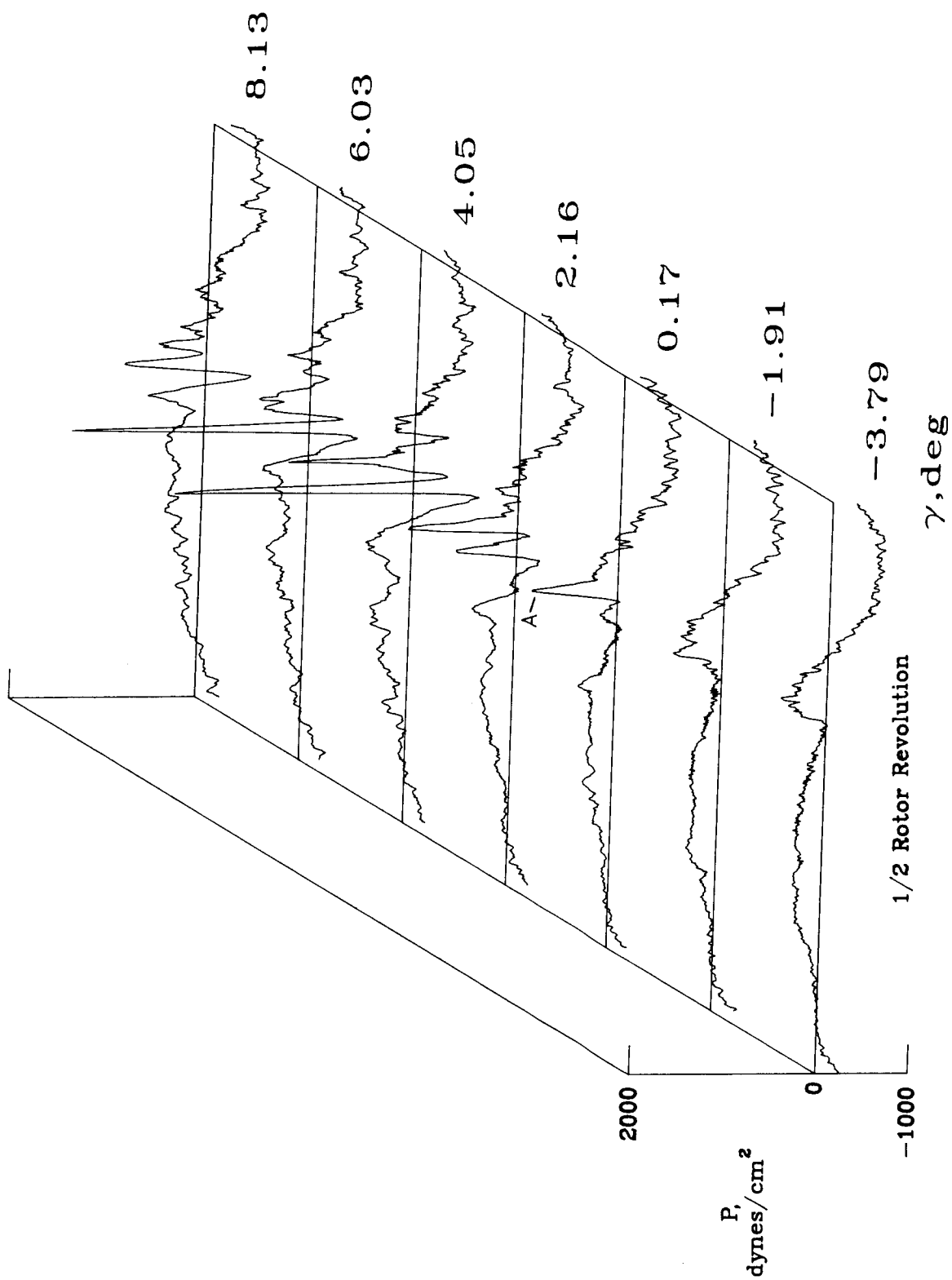
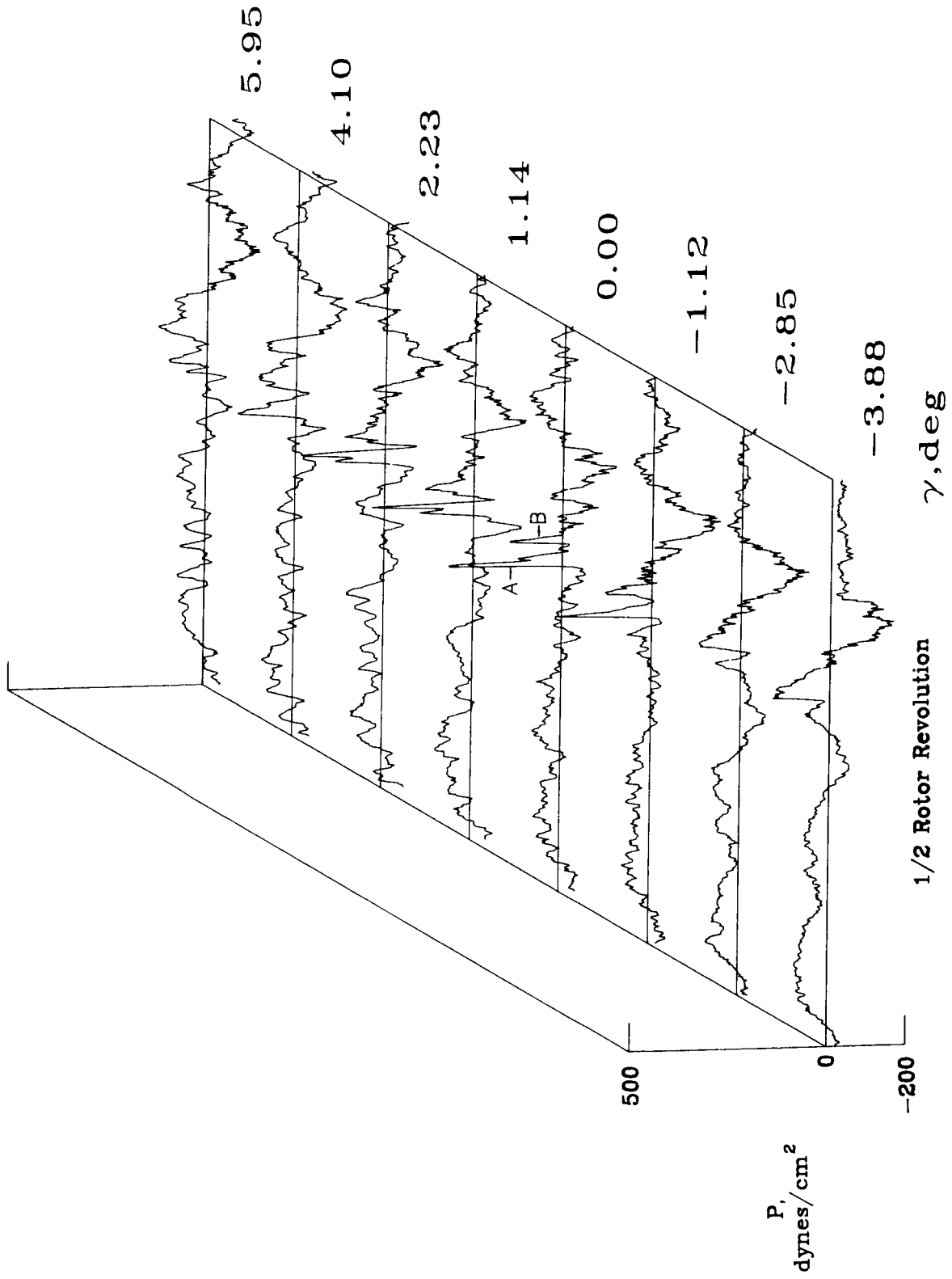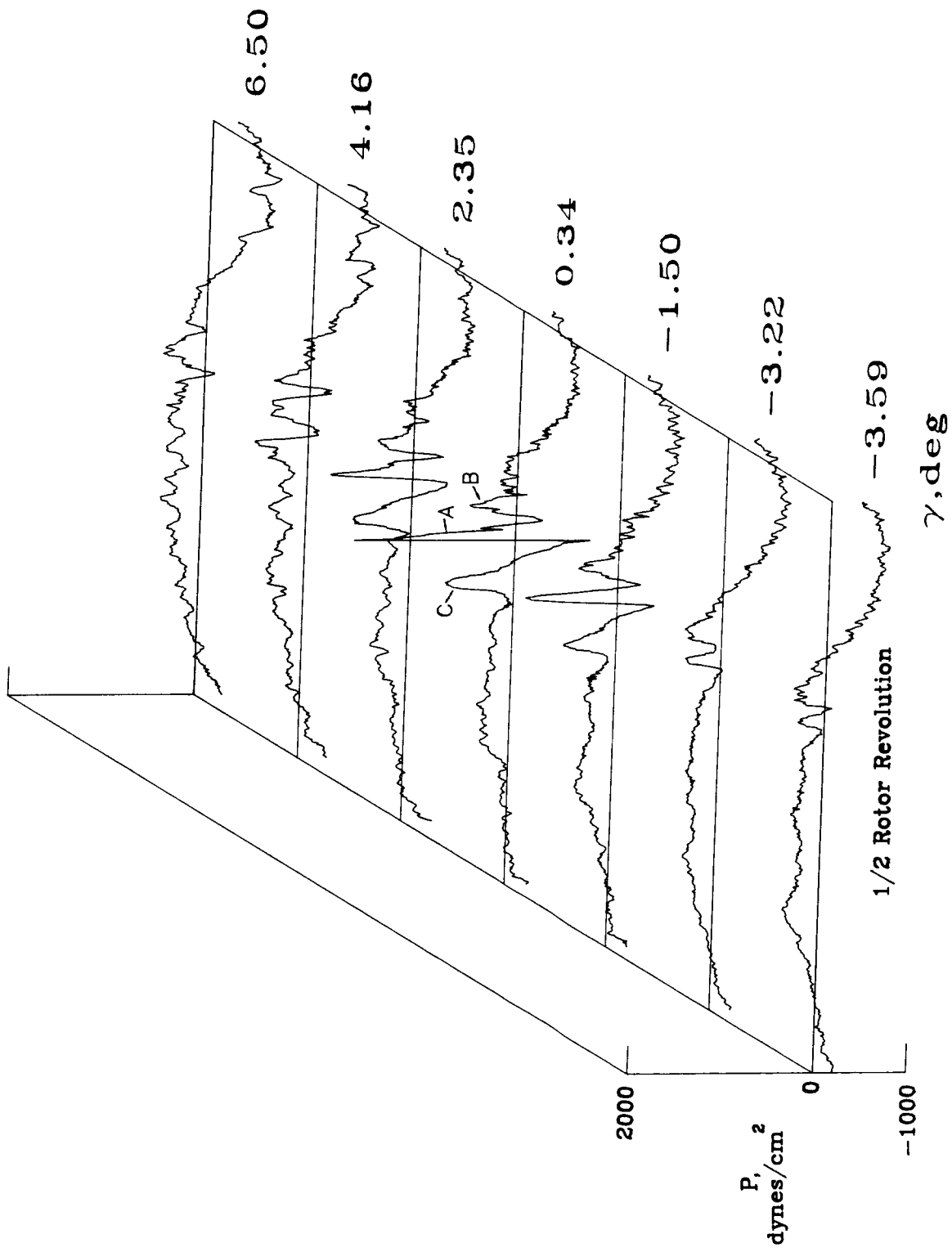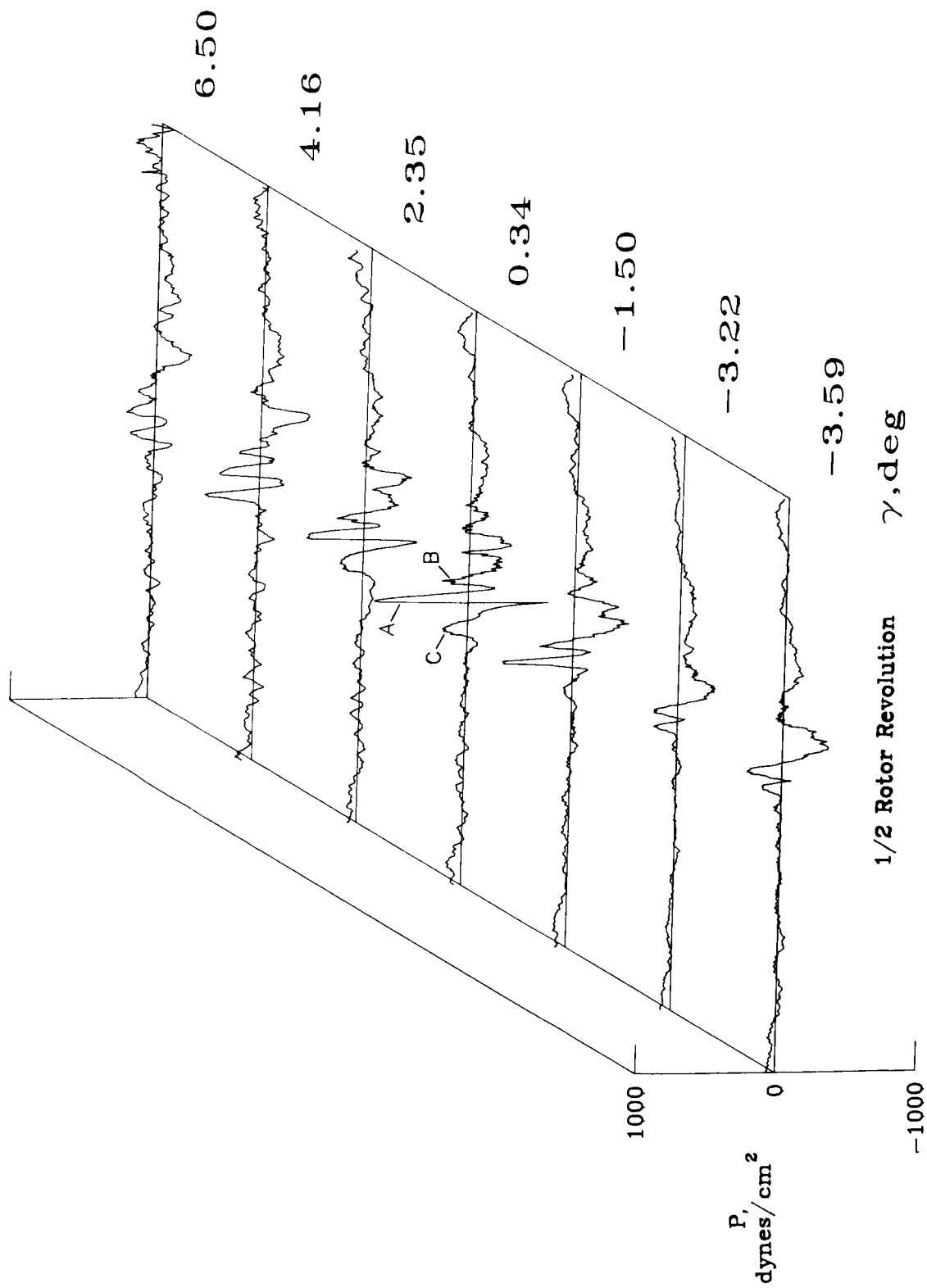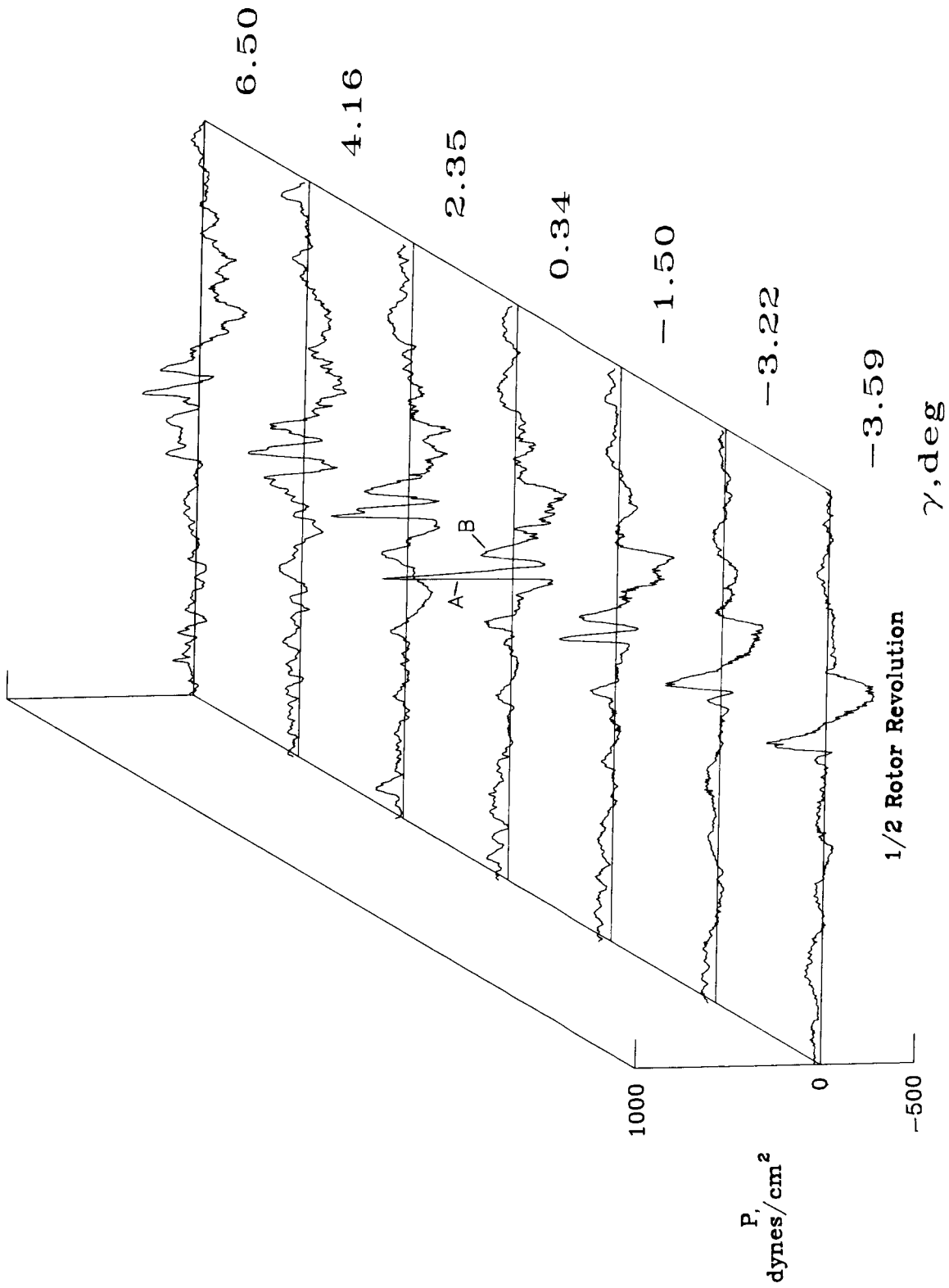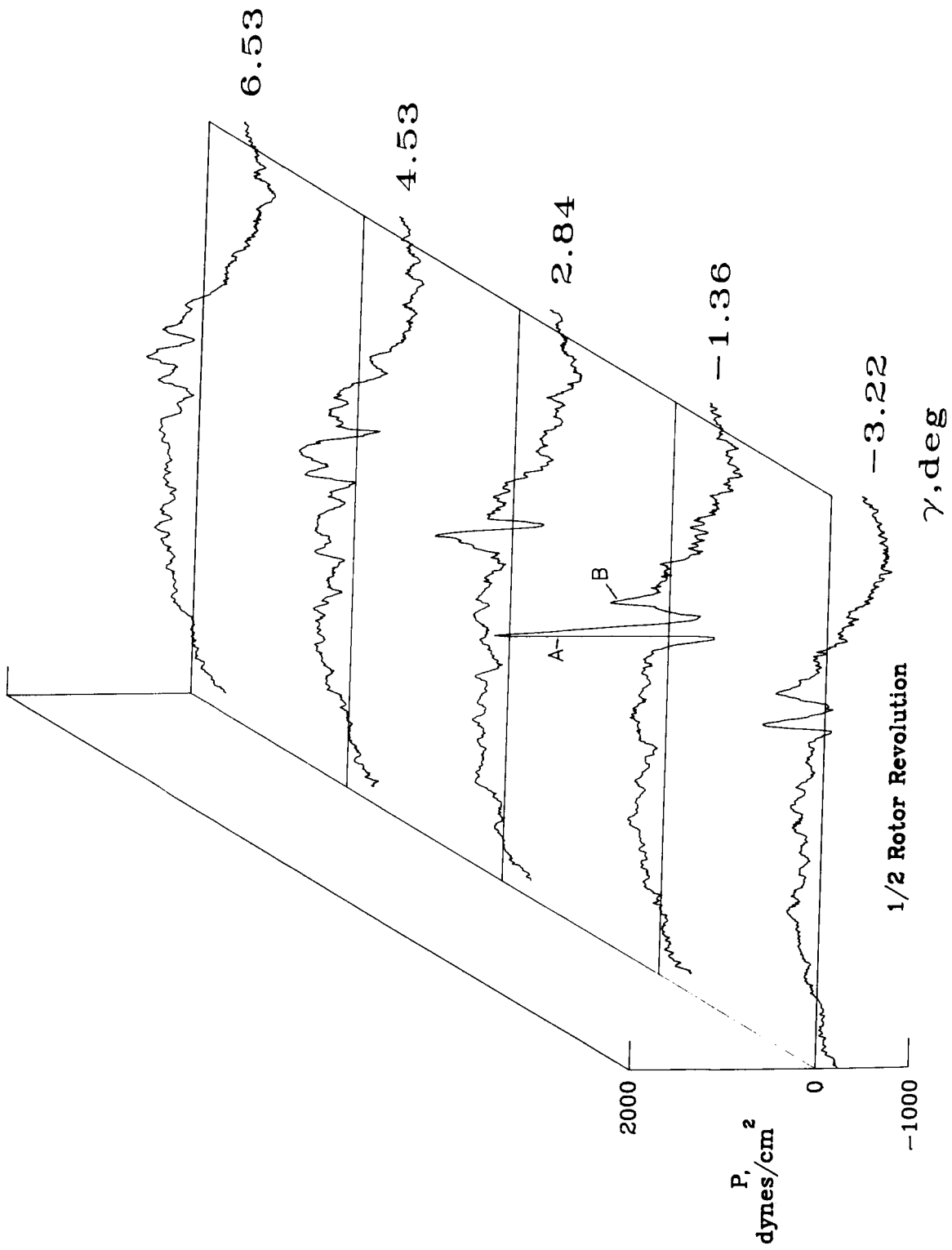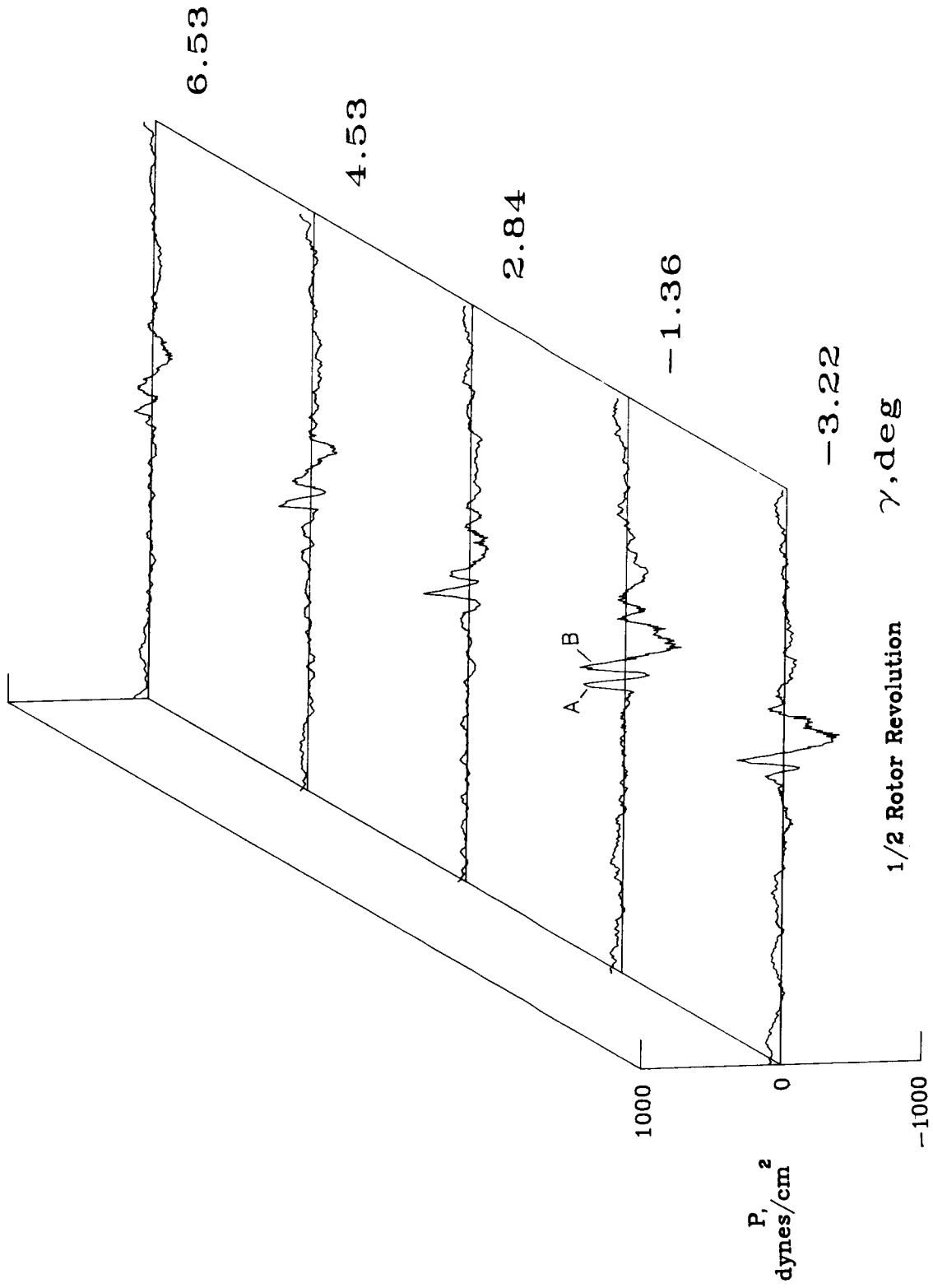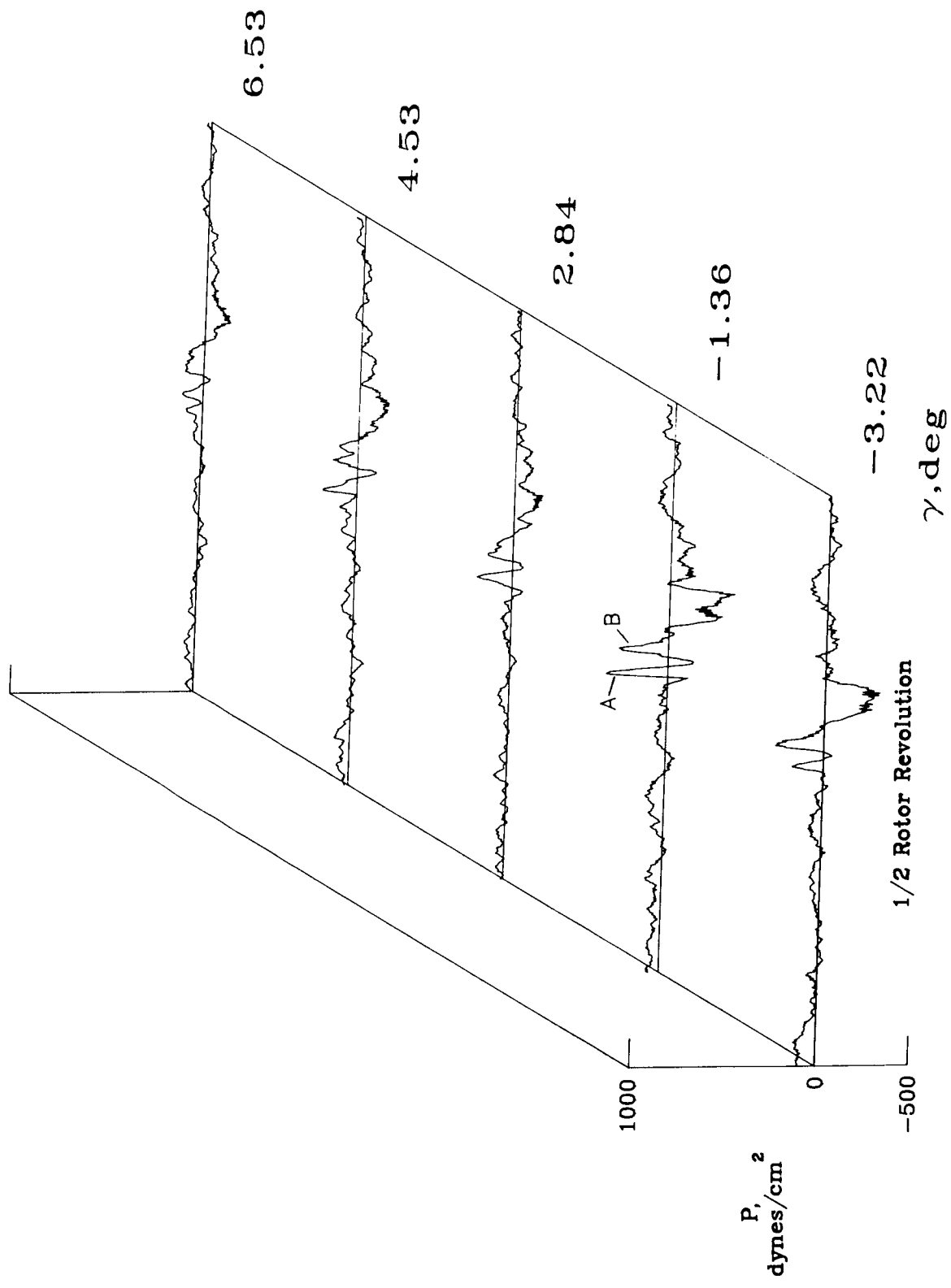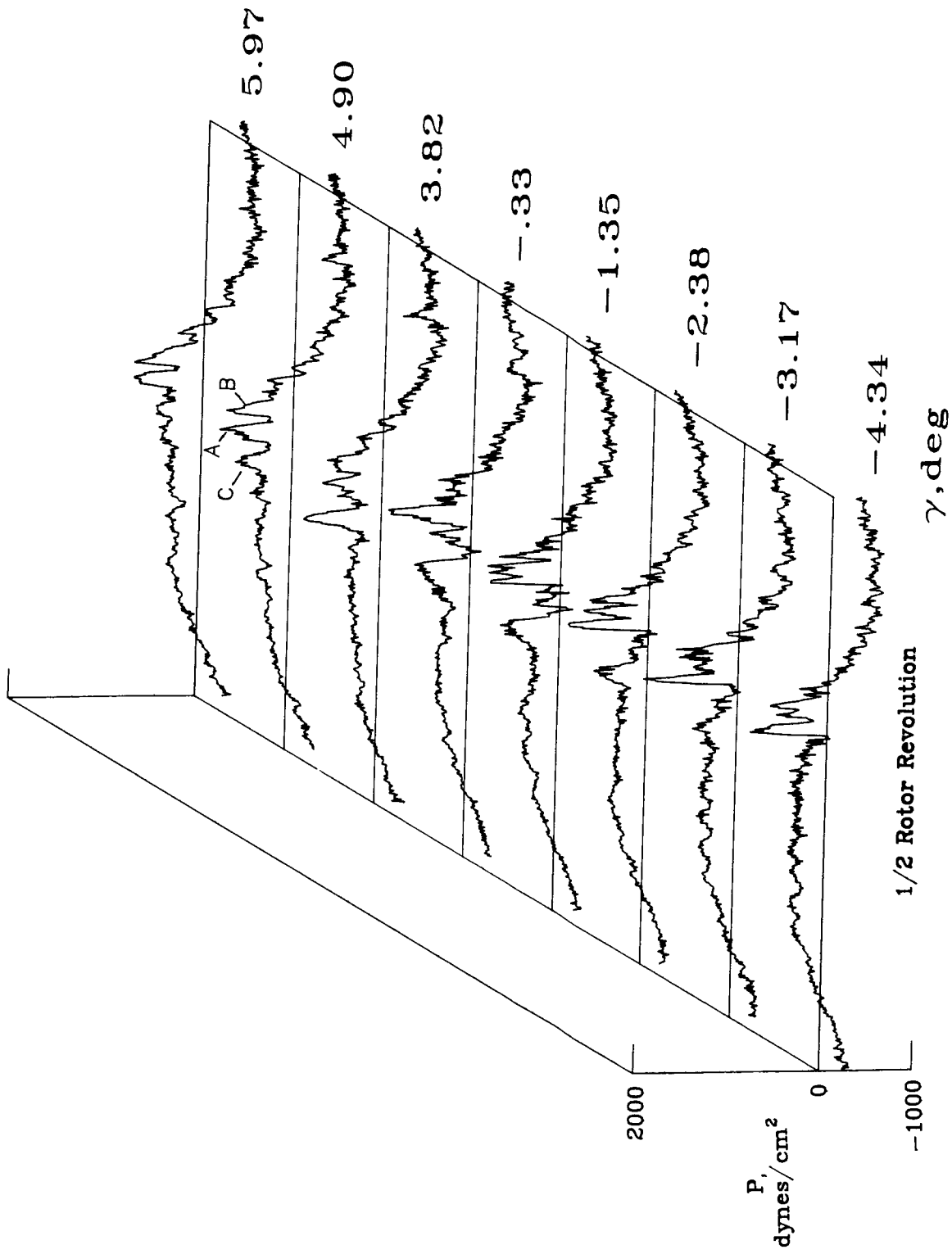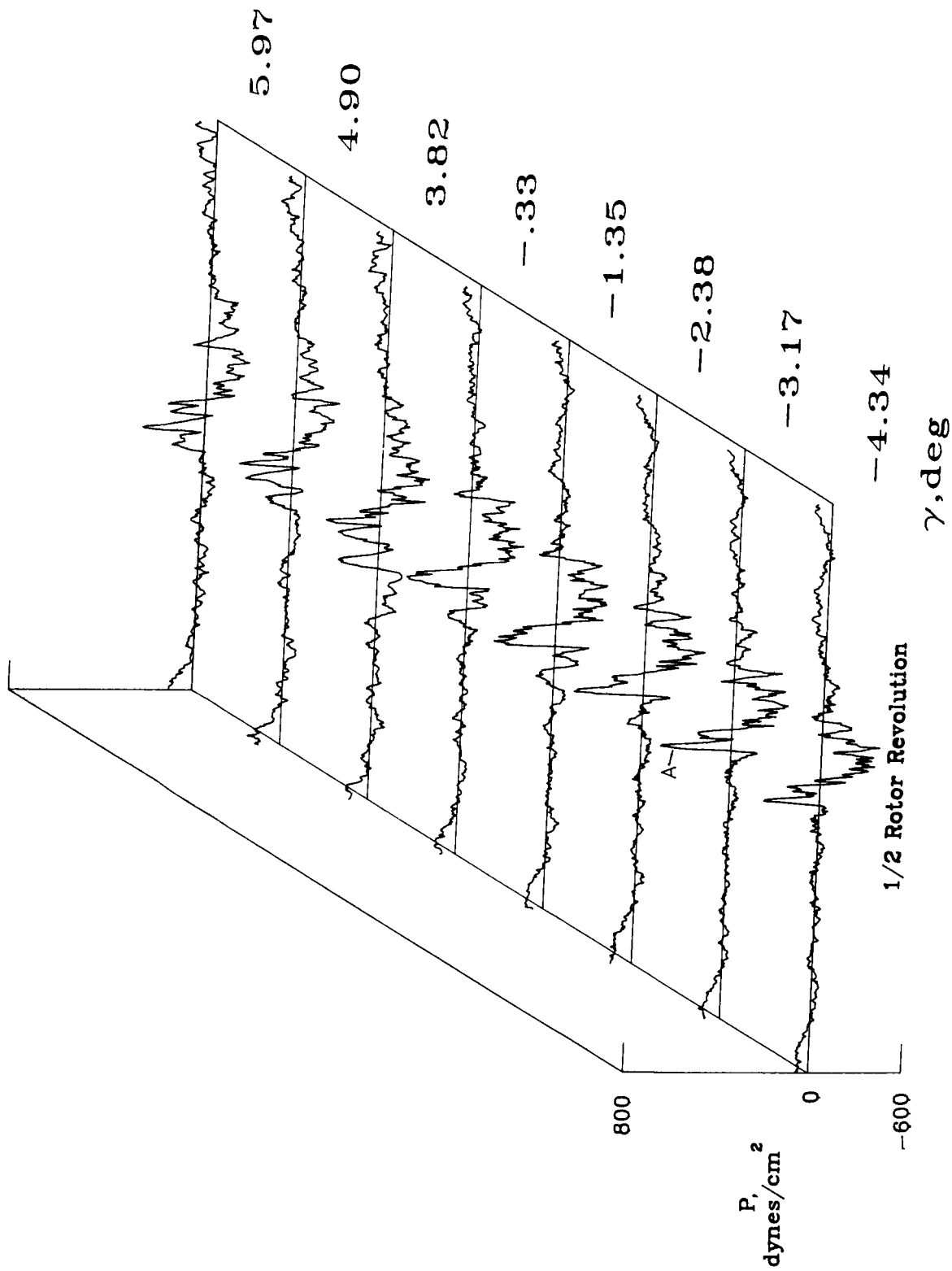Figure A2. Acoustic time history data for standard rotor sytem at $\mu = 0.103$ and $C_T = 0.00363$.
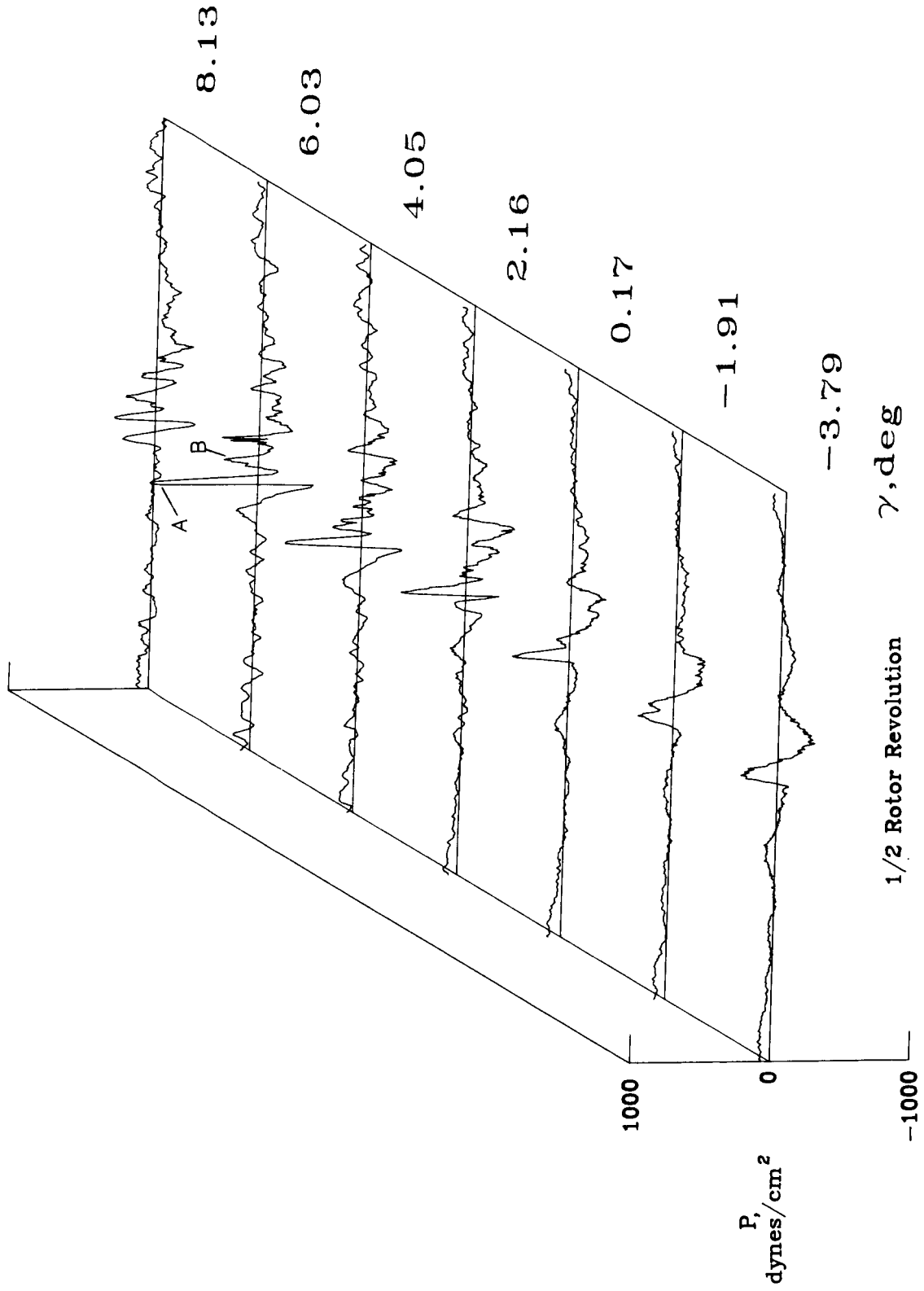
(a) Microphone 2.

(b) Microphone 6.

Figure A2. Continued.

8.13

6.03

4.05

2.16

−1.91

−3.79

γ,deg

B

A

1/2 Rotor Revolution

1000

0

−500

P, dynes/cm²
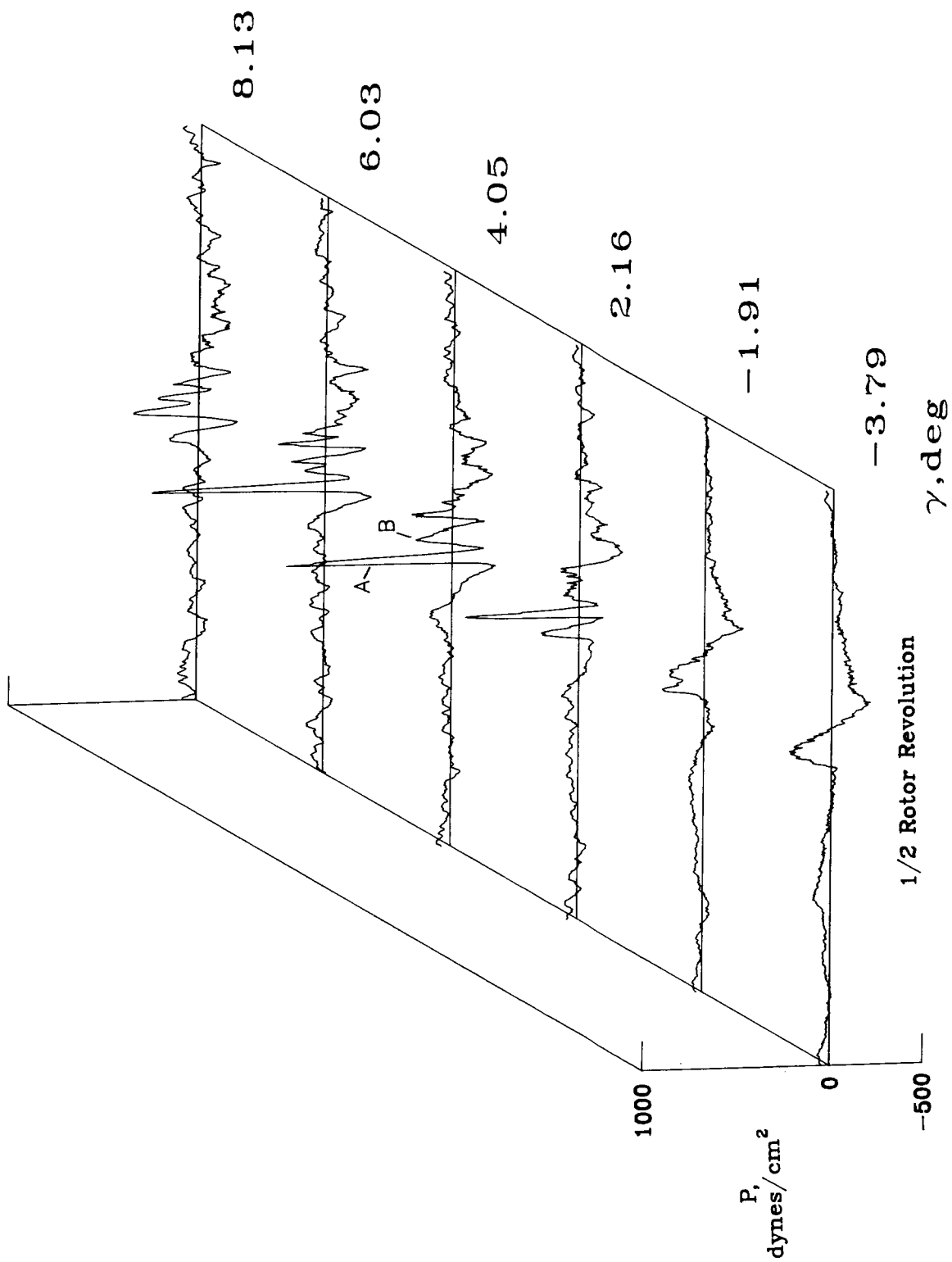
(c) Microphone 7.

Figure A2. Continued.

41
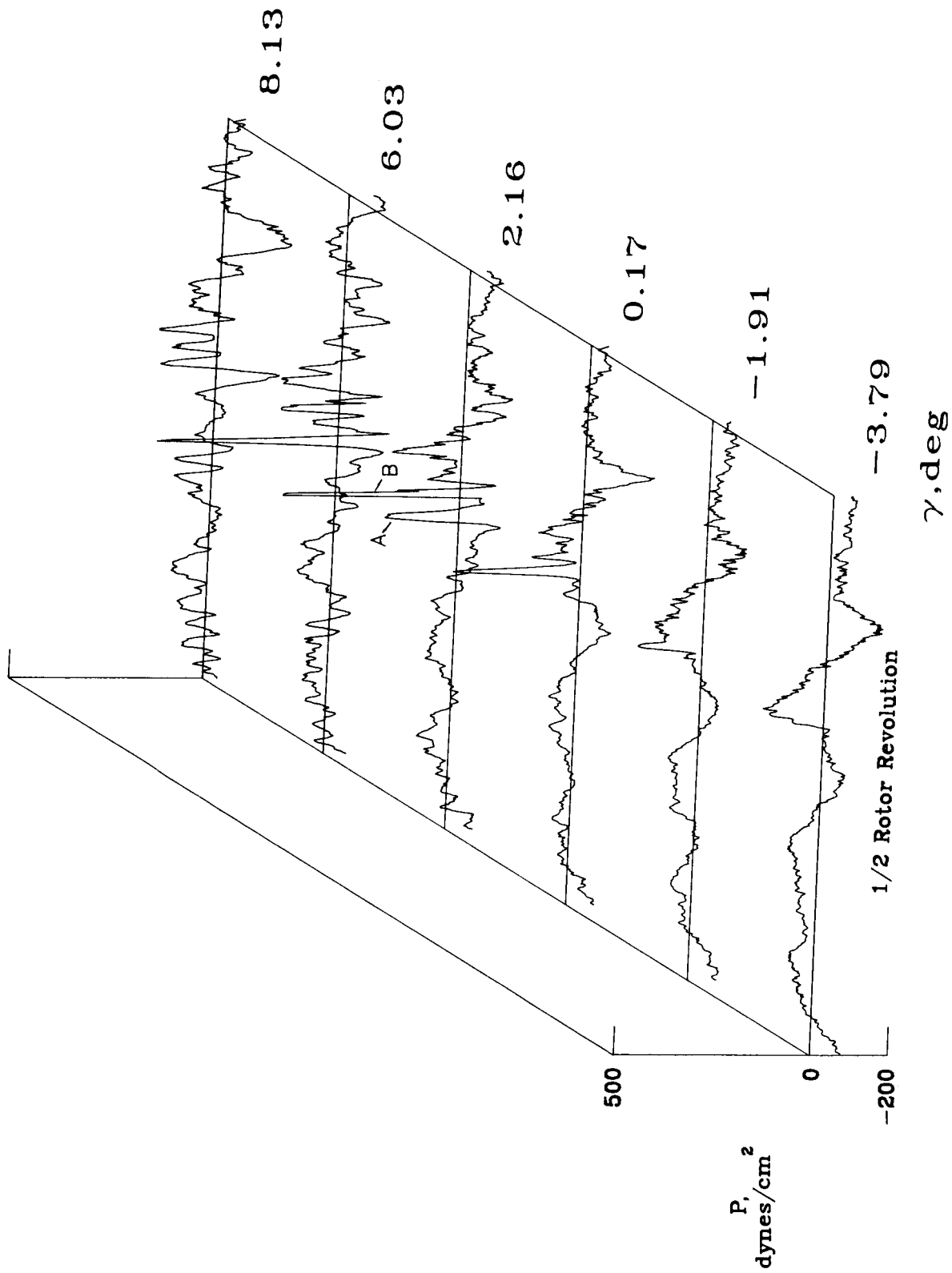
(d) Microphone 8.

Figure A2. Concluded.

4.94

3.89

2.94

1.98

1.00

−.10

−1.02

γ,deg

B
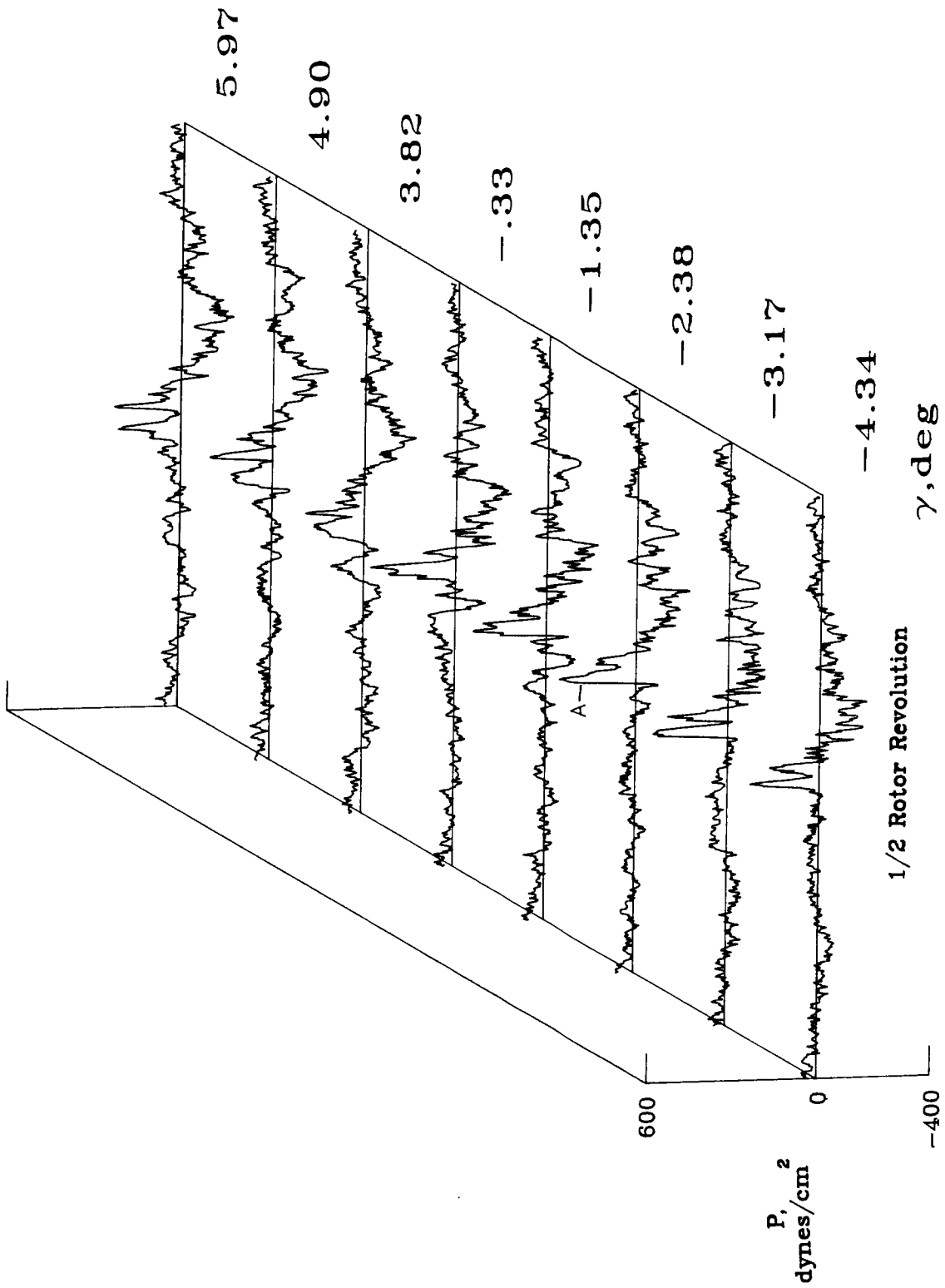
A

1/2 Rotor Revolution

2000

0

−1000

P,
dynes/cm^2
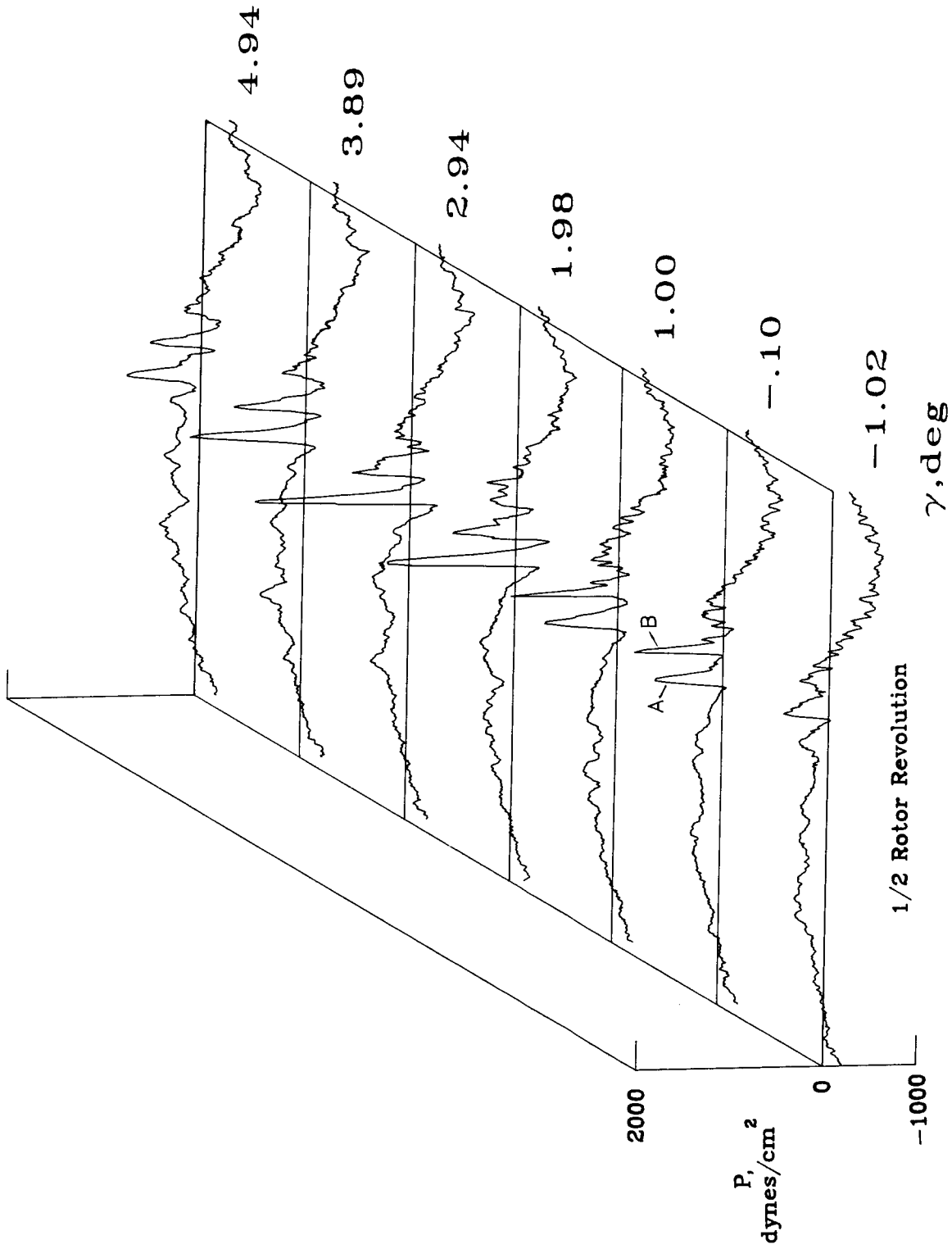
(a) Microphone 2.

Figure A3. Acoustic time history data for standard rotor sytem at $\mu = 0.115$ and $C_T = 0.00313$.
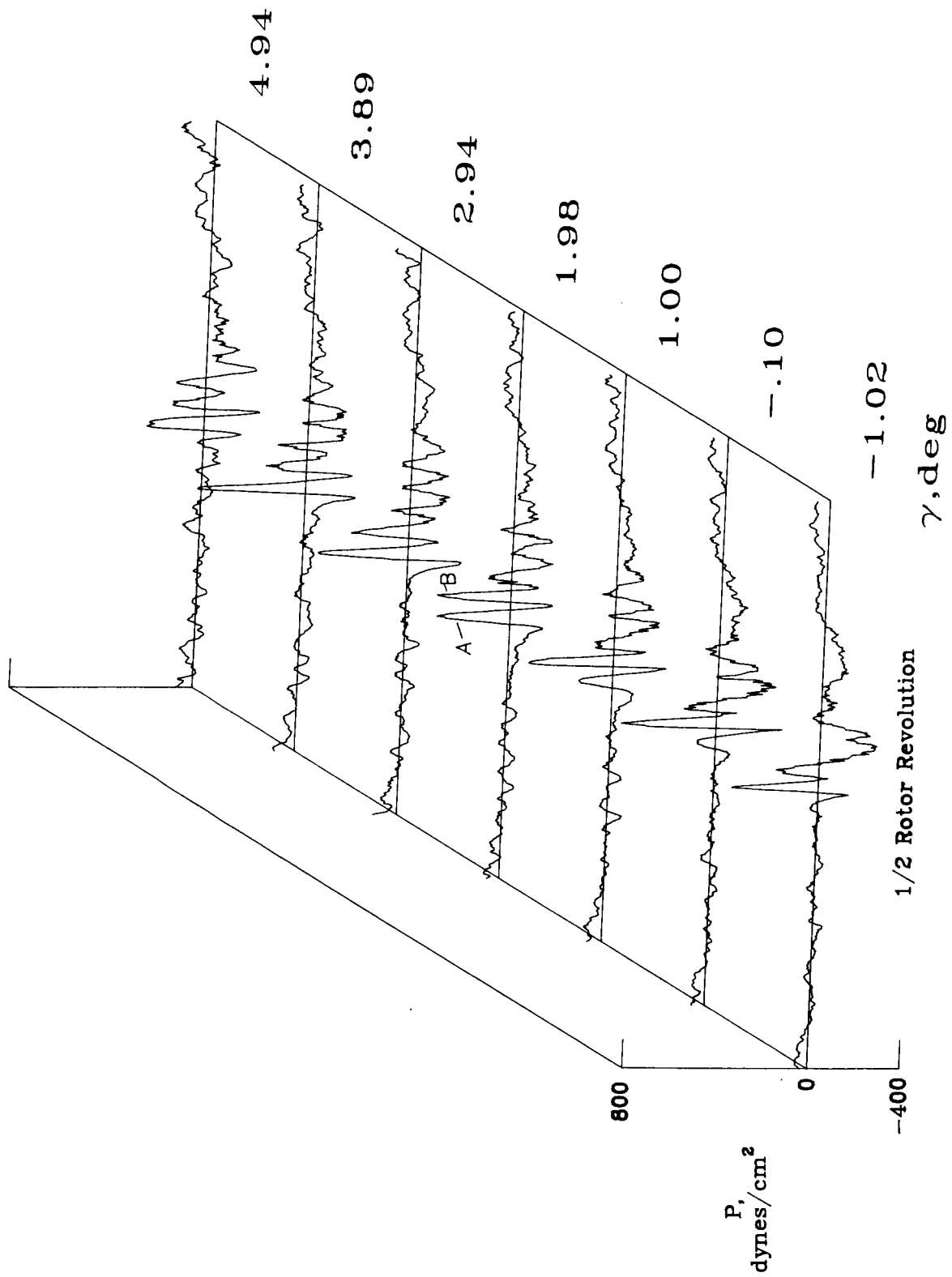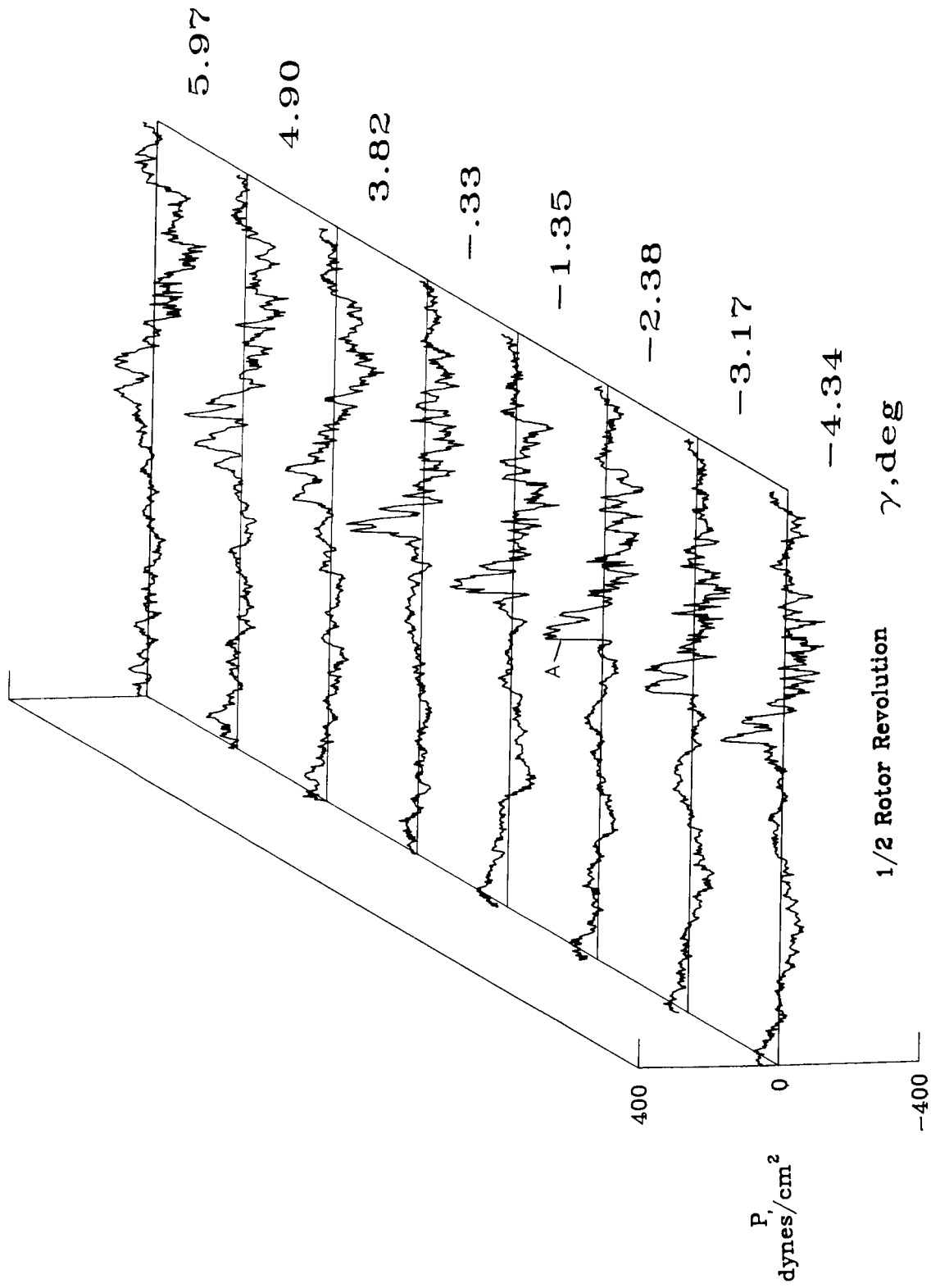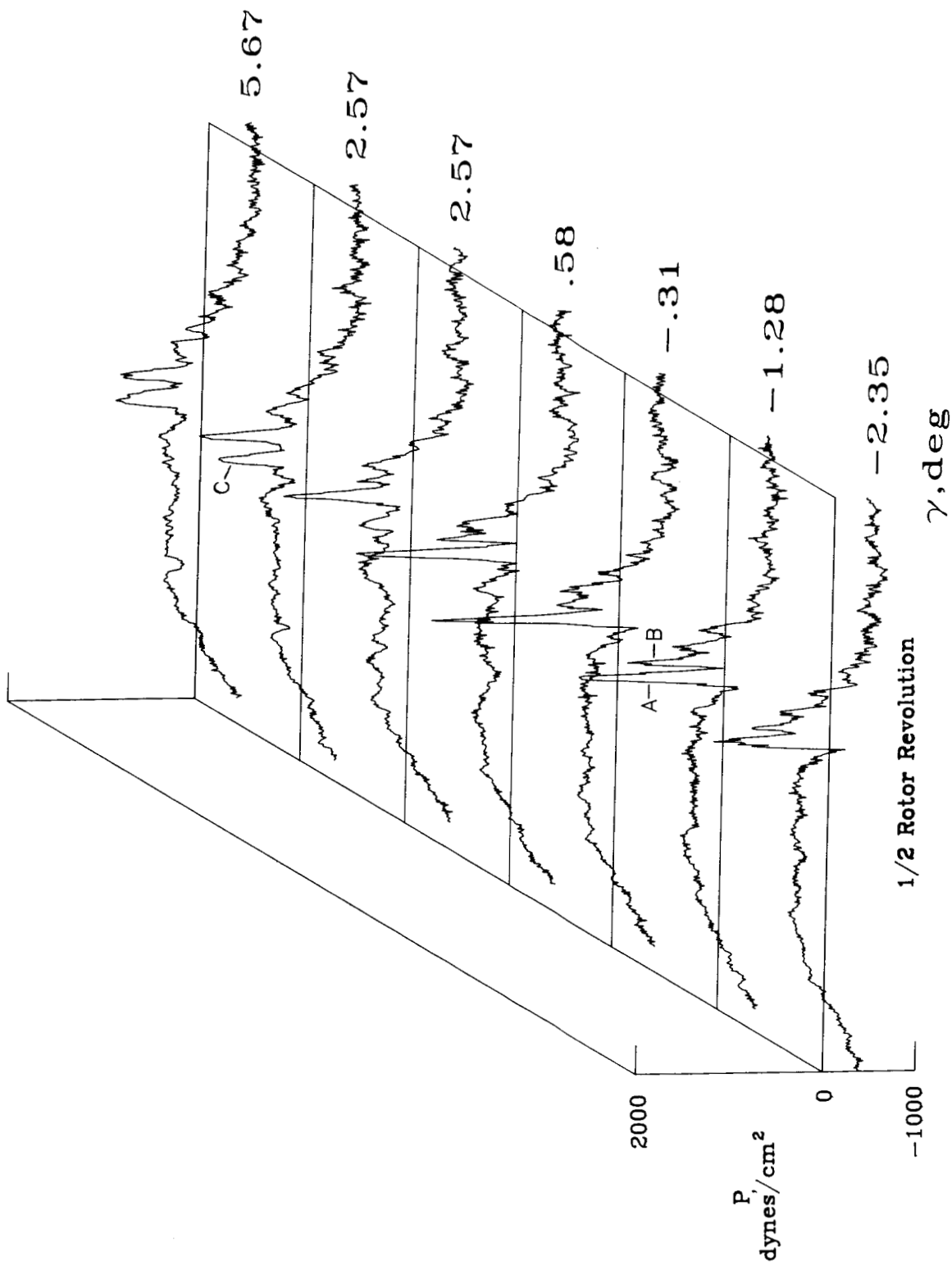
(b) Microphone 6.

Figure A3. Continued.

(c) Microphone 7.

Figure A3. Continued.
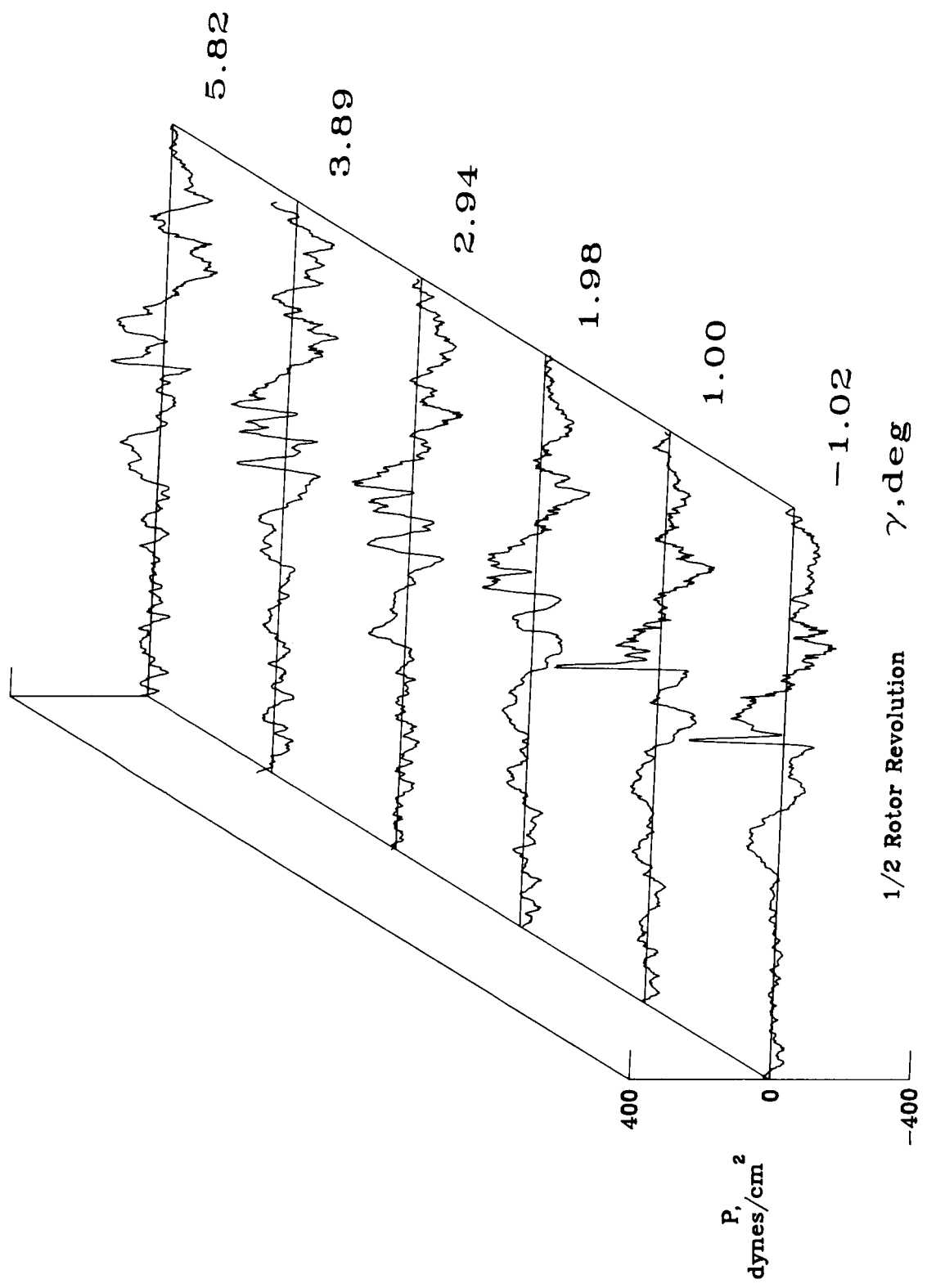
(d) Microphone 8.

Figure A3. Concluded.
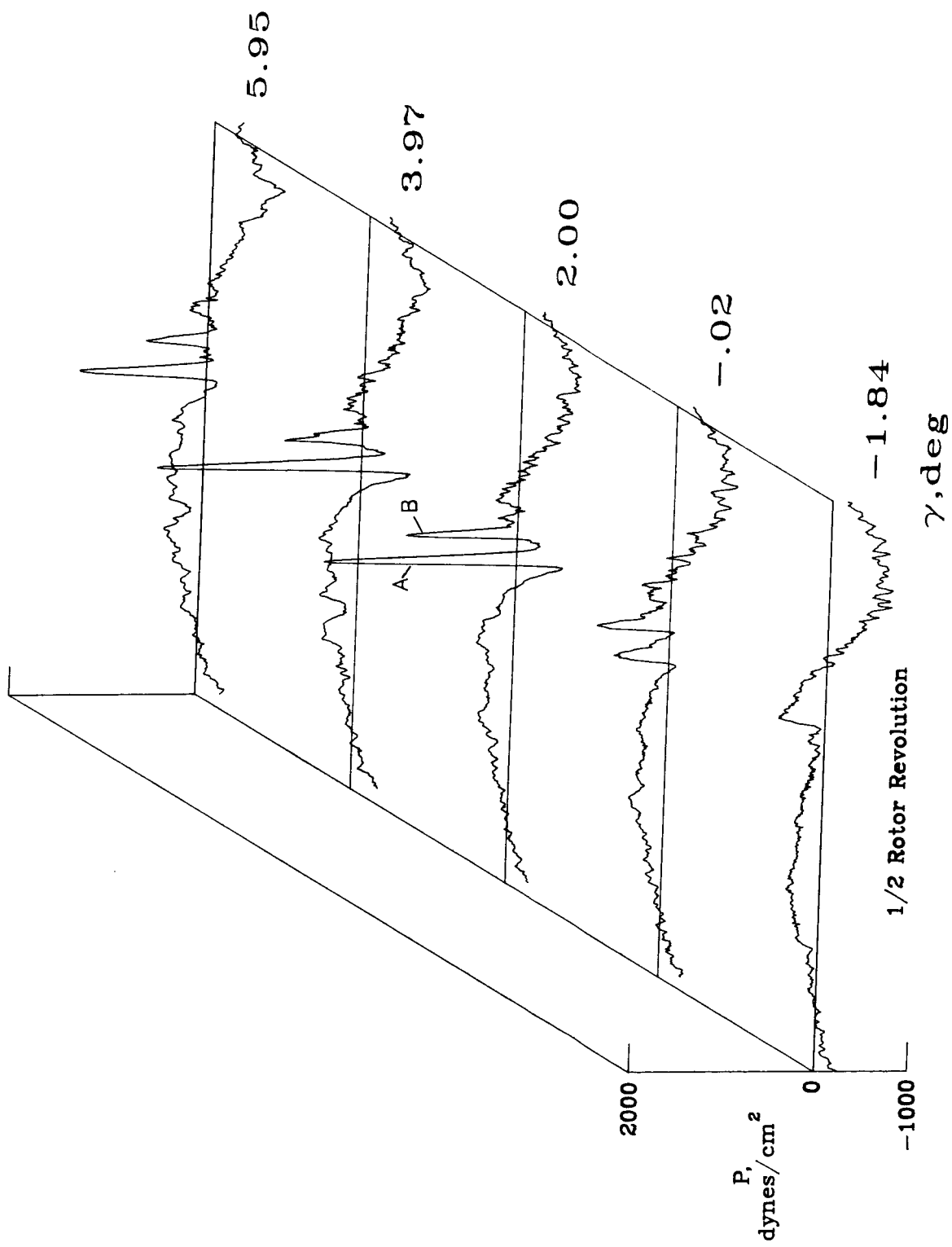
Figure A4. Acoustic time history data for standard rotor system at $\mu = 0.115$ and $C_T = 0.00364$.

(a) Microphone 2.

(b) Microphone 6.

Figure A4. Continued.

5.95

3.97

2.00

−.02

−1.84

γ, deg

A

B

P,
dynes/cm²

600

0

−400

1/2 Rotor Revolution

(c) Microphone 7.

Figure A4. Continued.

5.95

3.97

2.00

−.02

−1.84

γ,deg
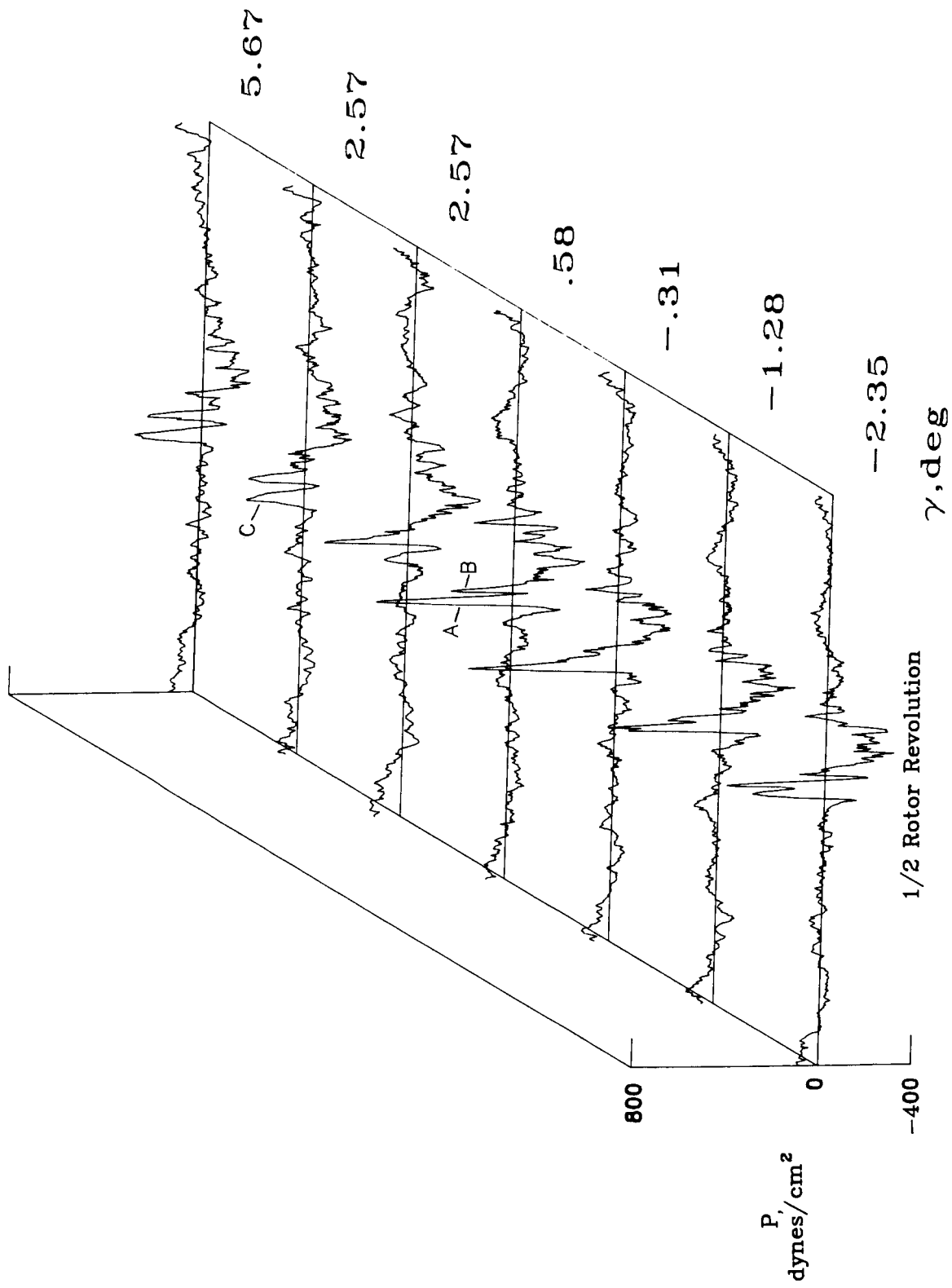
B

A

1/2 Rotor Revolution

400

0

−400

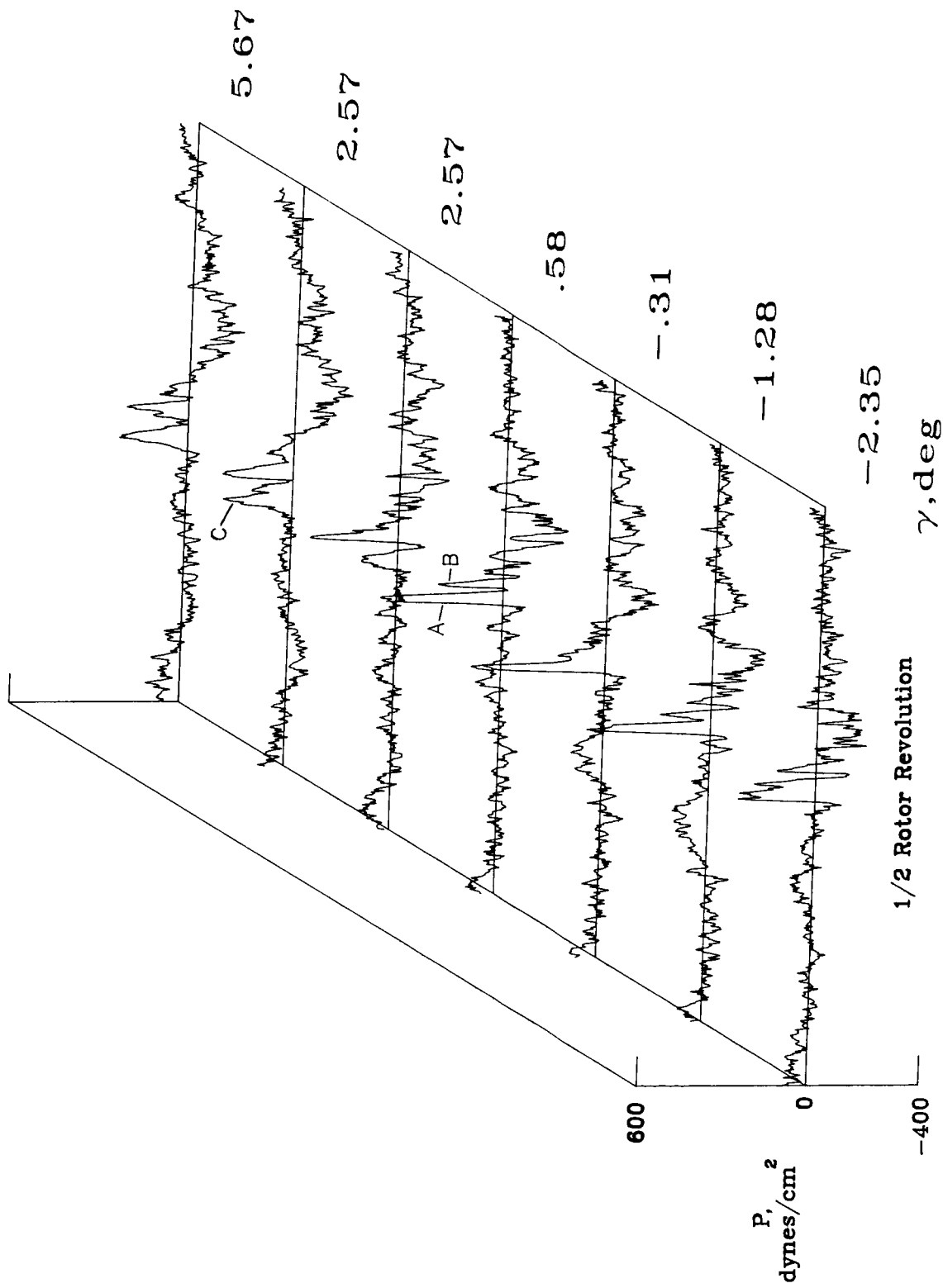P, dynes/cm^2

(d) Microphone 8.

Figure A4. Concluded.
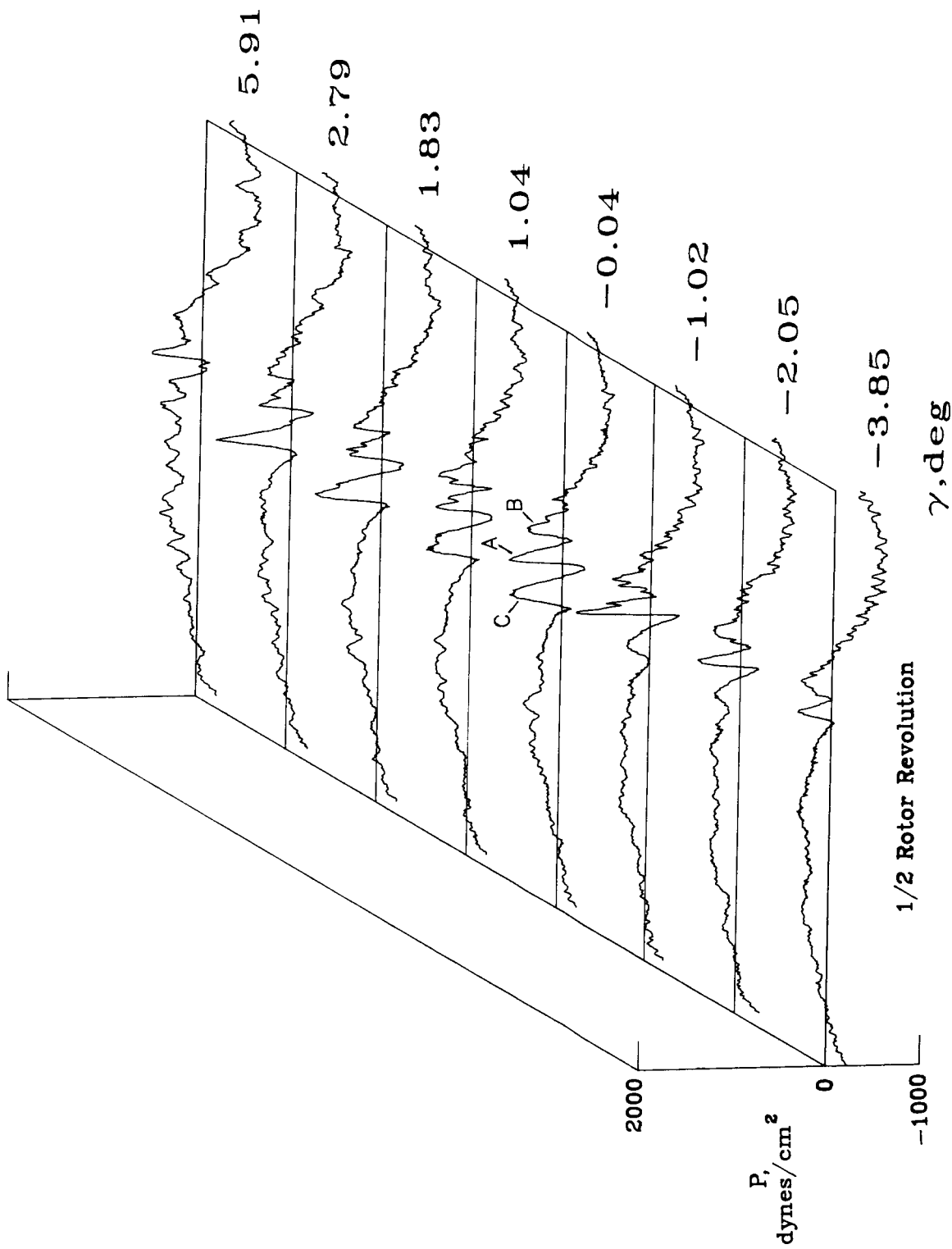
(a) Microphone 2.

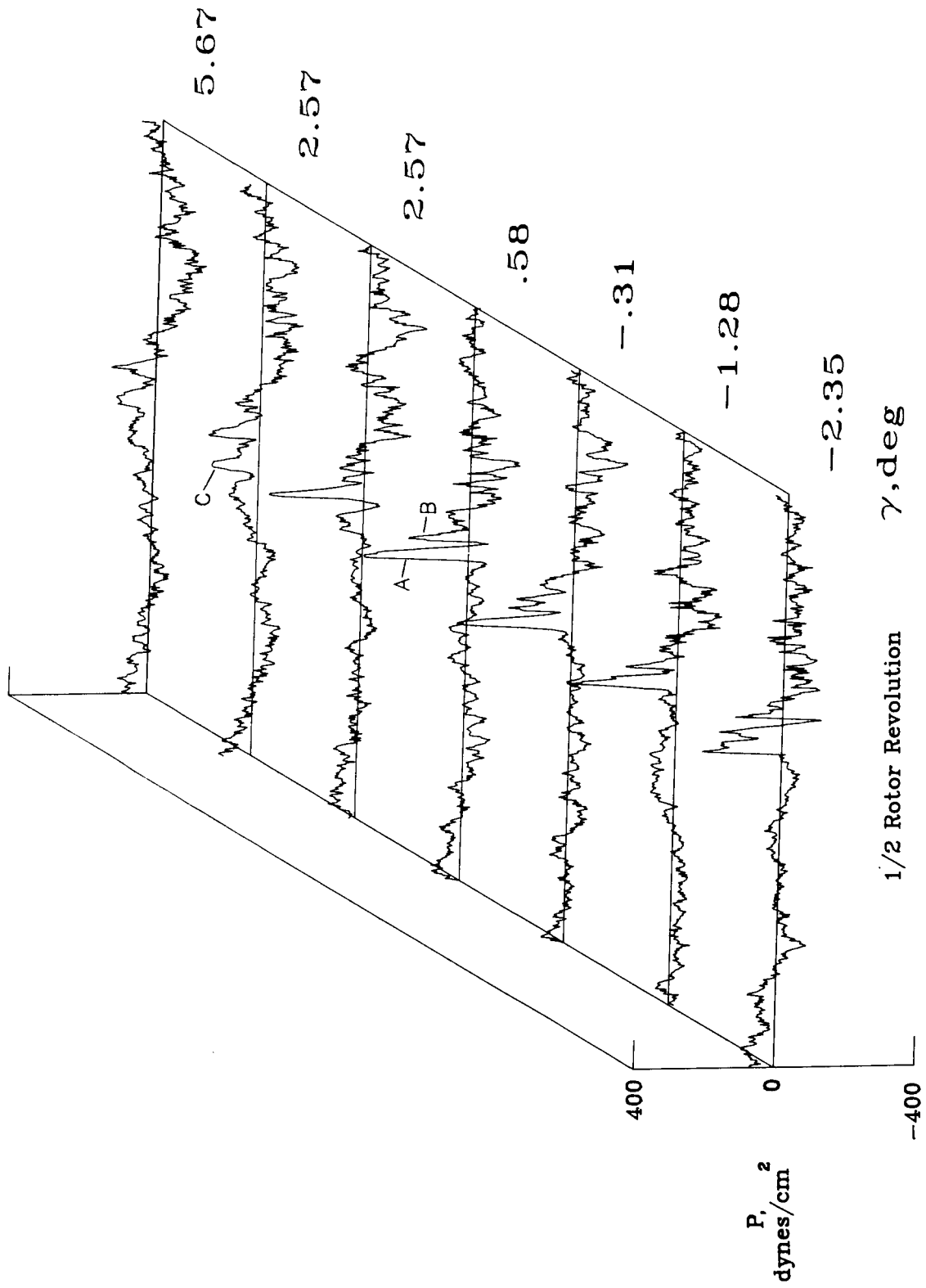Figure A5. Acoustic time history data for standard rotor system at $\mu = 0.124$ and $C_T = 0.00317$.

51
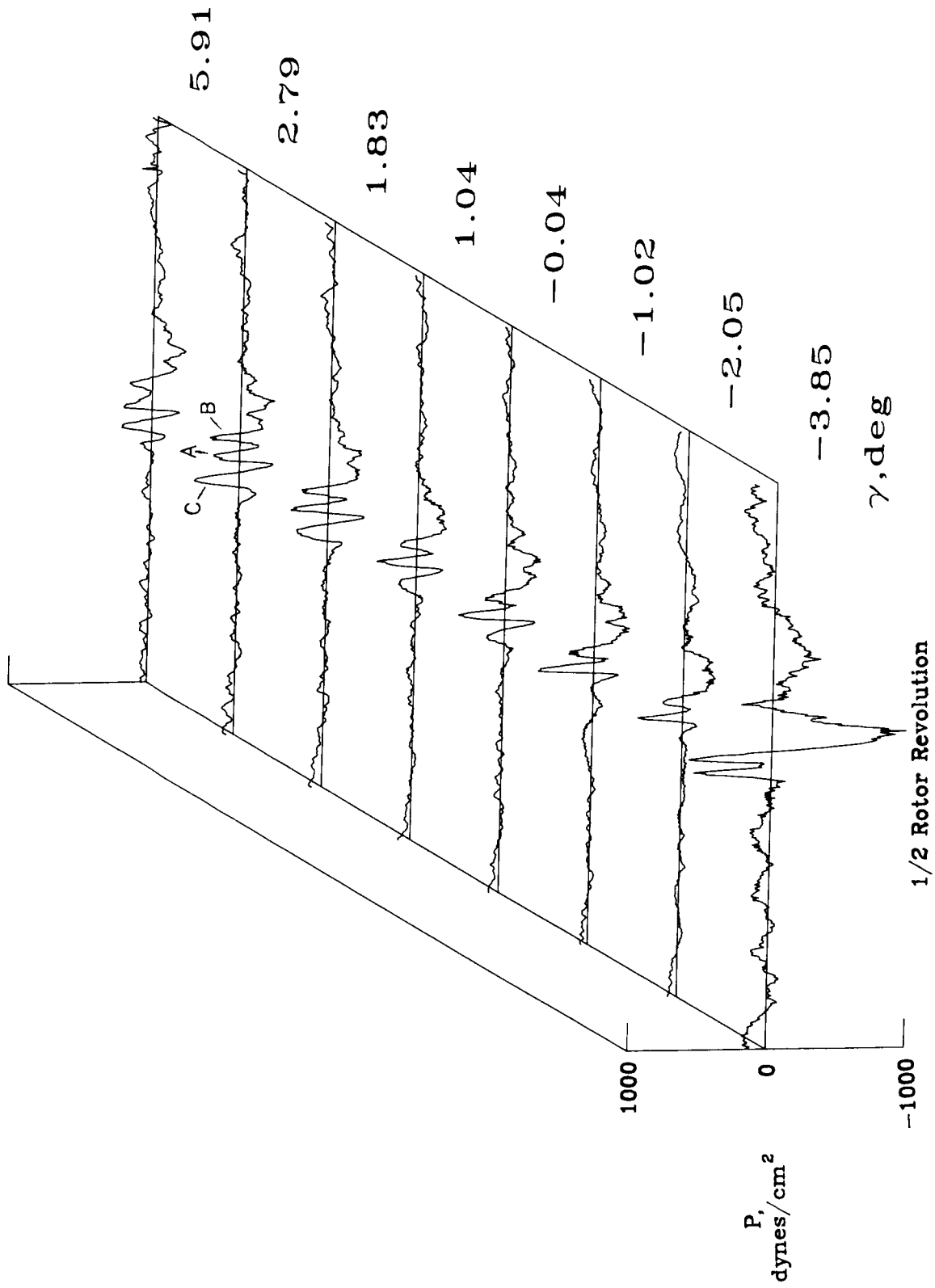
(b) Microphone 6.

Figure A5. Continued.

5.91

2.79

1.83

1.04

−0.04

−1.02

−2.05

−3.85

γ, deg

C

A

1/2 Rotor Revolution

P, dynes/cm²

1000

0

−500
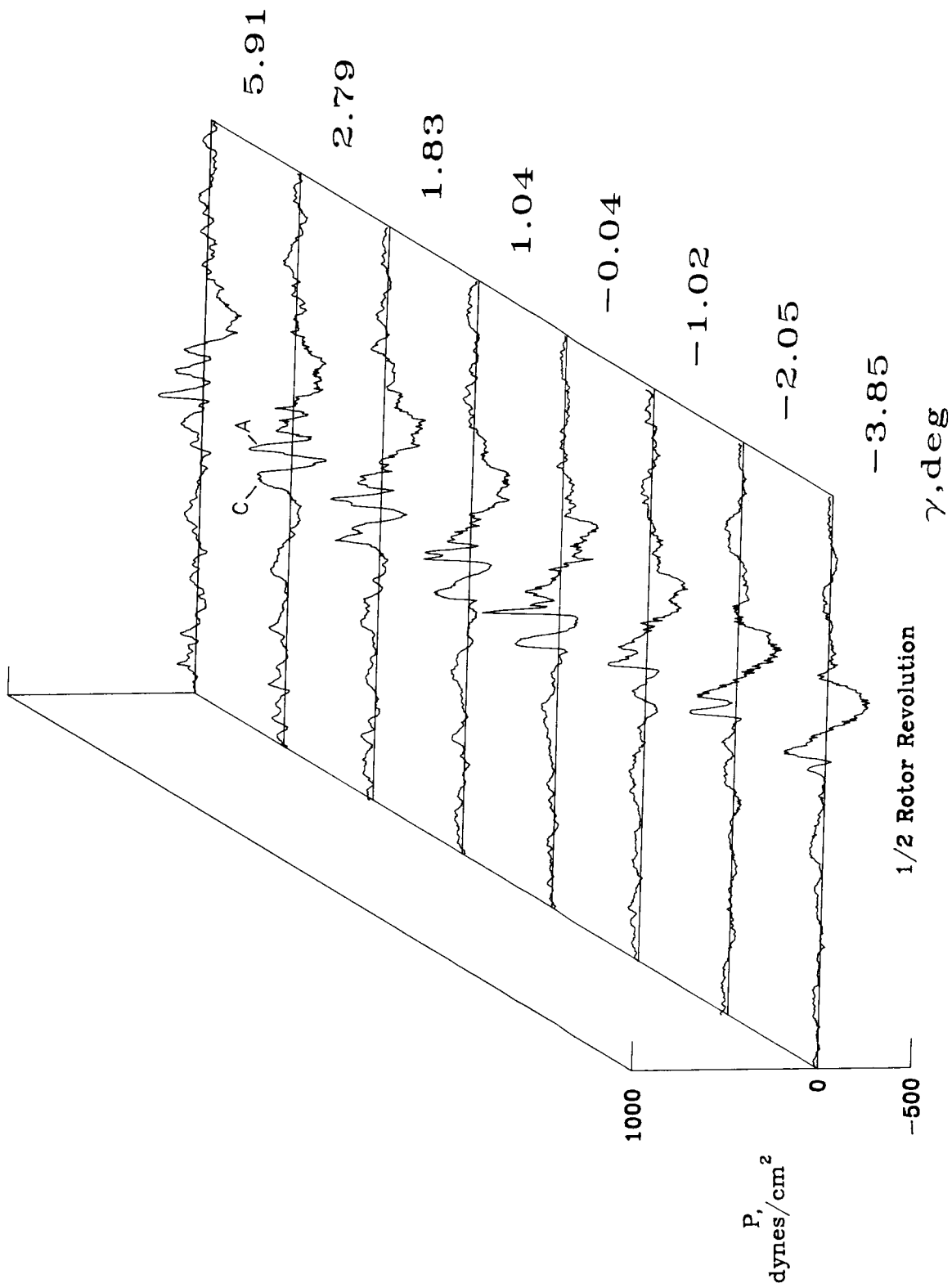
(c) Microphone 7.

Figure A5. Continued.

5.91

2.79

1.83

1.04

−0.04

−1.02

−2.05

−3.85

γ, deg

A

1/2 Rotor Revolution

500

0

−200

P, dynes/cm^2
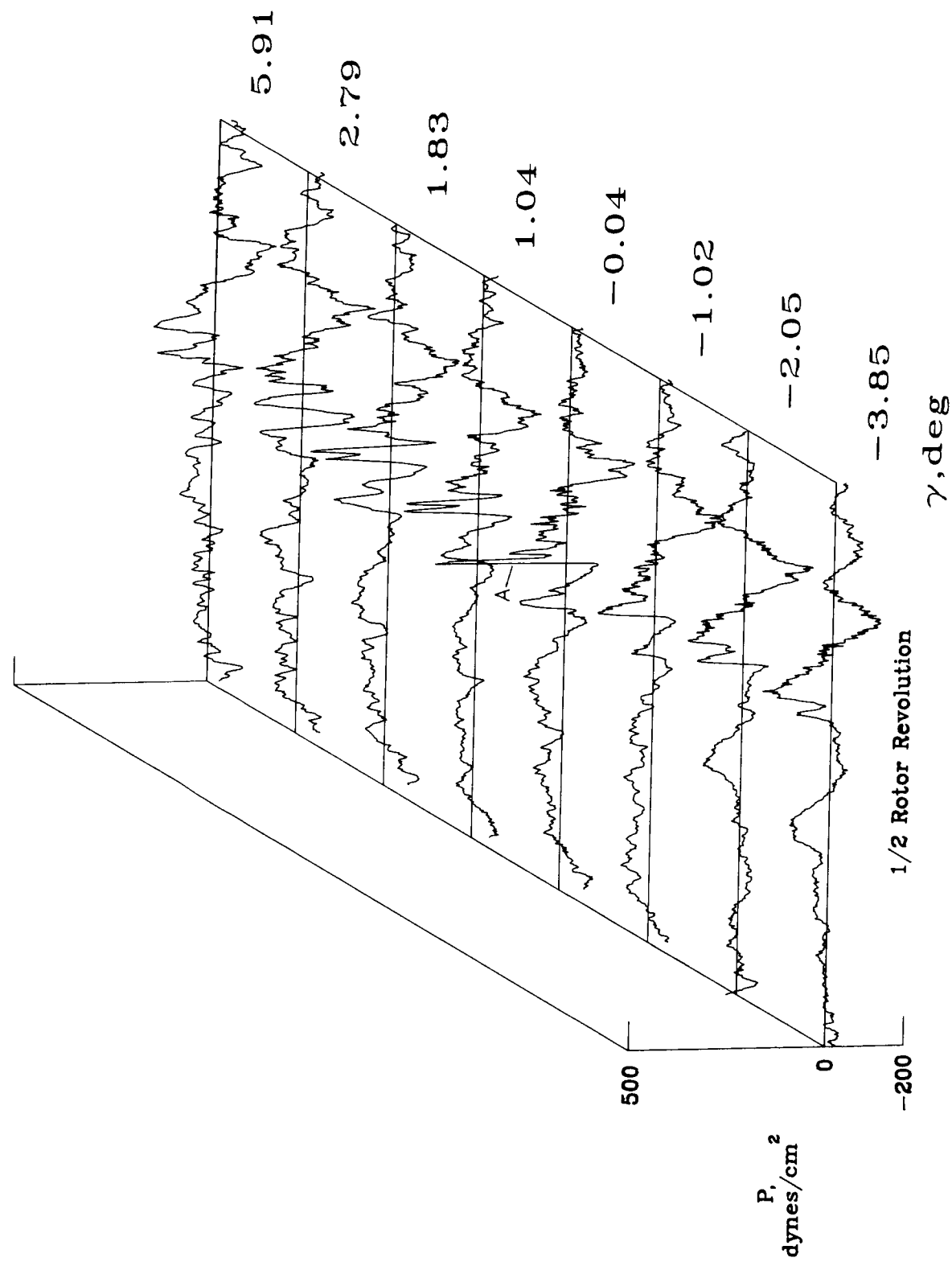
(d) Microphone 8.

Figure A5. Concluded.
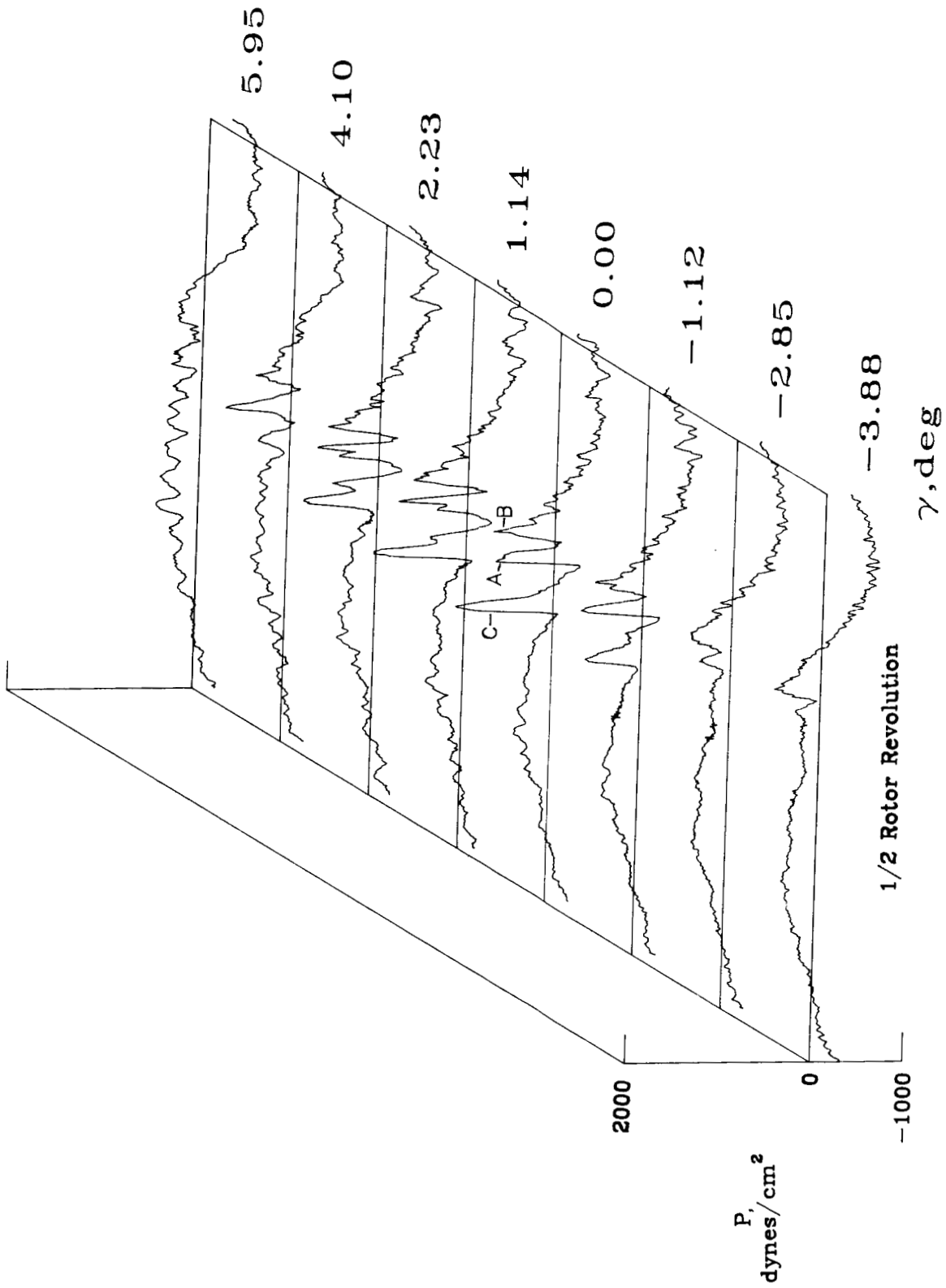
(a) Microphone 2.

Figure A6. Acoustic time history data for standard rotor system at $\mu = 0.135$ and $C_T = 0.00320$.

(b) Microphone 6.

Figure A6. Continued.

5.95
4.10
2.23
1.14
0.00
−1.12
−2.85
−3.88

γ, deg

A
B

1/2 Rotor Revolution

1000

0

−500

P,
dynes/cm^2

(c) Microphone 7.

Figure A6. Continued.

(d) Microphone 8.

Figure A6. Concluded.

(a) Microphone 2.

Figure A7. Acoustic time history data for standard rotor system at $\mu = 0.135$ and $C_T = 0.00361$.
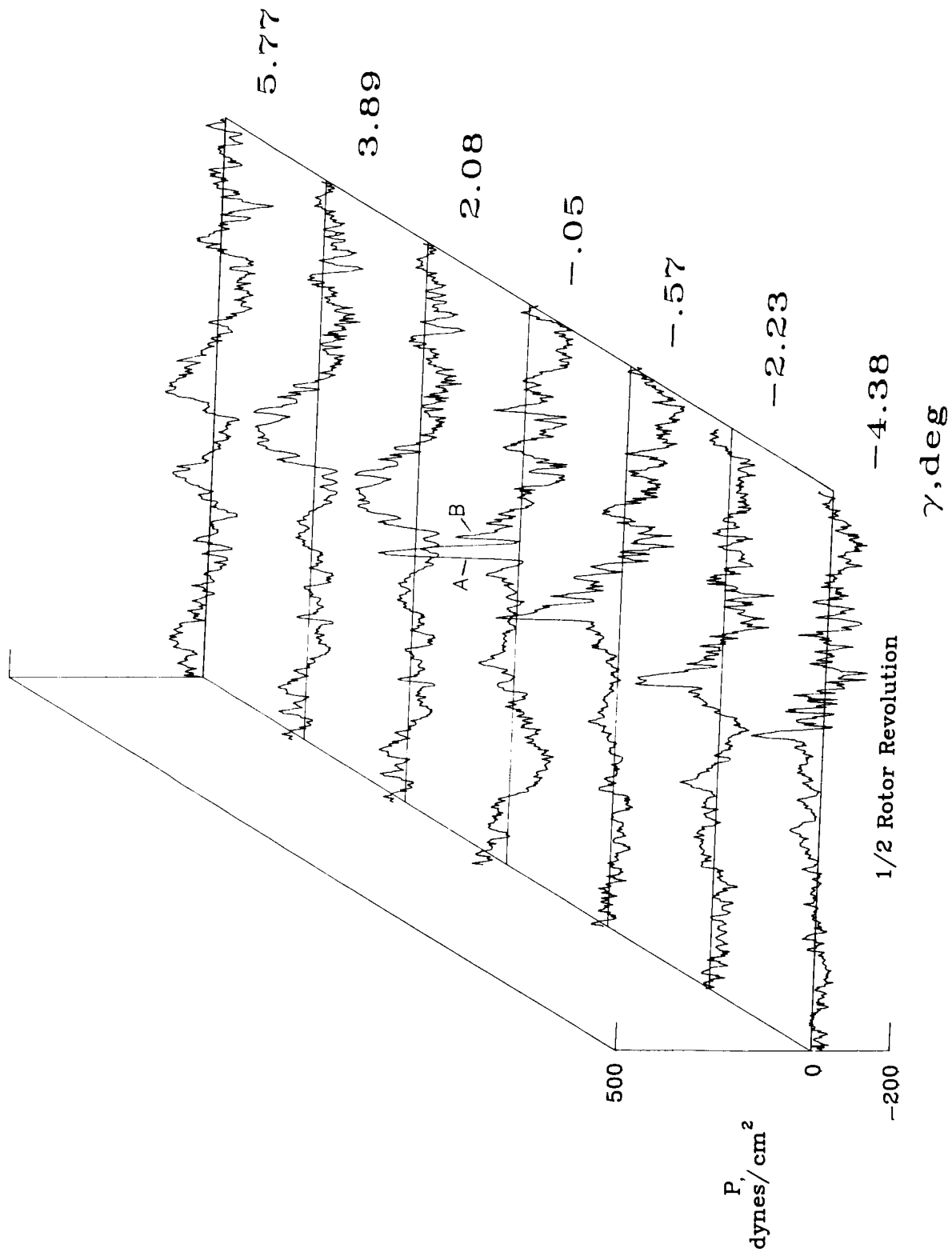
(b) Microphone 6.

Figure A7. Continued.

6.50

4.16

2.35

0.34

−1.50

−3.22

−3.59

γ, deg

A

B

1/2 Rotor Revolution

1000

0

−500

P,
dynes/cm²

(c) Microphone 7.

Figure A7. Concluded.

Figure A8. Acoustic time history data for standard rotor system at $\mu = 0.155$ and $C_T = 0.00355$.

(a) Microphone 2.

(b) Microphone 6.

Figure A8. Continued.

(c) Microphone 7.

Figure A8. Concluded.

(a) Microphone 2.

Figure A9. Acoustic time history data for advanced rotor system at $\mu = 0.125$ and $C_T = 0.00312$.

(b) Microphone 6.

Figure A9. Continued.

5.97
4.90
3.82
-.33
-1.35
-2.38
-3.17
-4.34

γ,deg

A—

1/2 Rotor Revolution

P,
dynes/cm²

600
0
-400

(c) Microphone 7.

Figure A9. Continued.

5.97
4.90
3.82
−.33
−1.35
−2.38
−3.17
−4.34

A

γ,deg

1/2 Rotor Revolution

P,
dynes/cm²

400

0

−400

(d) Microphone 8.

Figure A9. Concluded.

5.67

2.57

2.57

.58

−.31

−1.28

−2.35

γ, deg

C

A
B

1/2 Rotor Revolution

P,
dynes/cm²

2000

0

−1000

(a) Microphone 2.

Figure A10. Acoustic time history data for the advanced rotor system at $\mu = 0.145$ and $C_T = 0.00308$.

(b) Microphone 6.

Figure A10. Continued.

(c) Microphone 7.

Figure A10. Continued.

(d) Microphone 8.

Figure A10. Concluded.
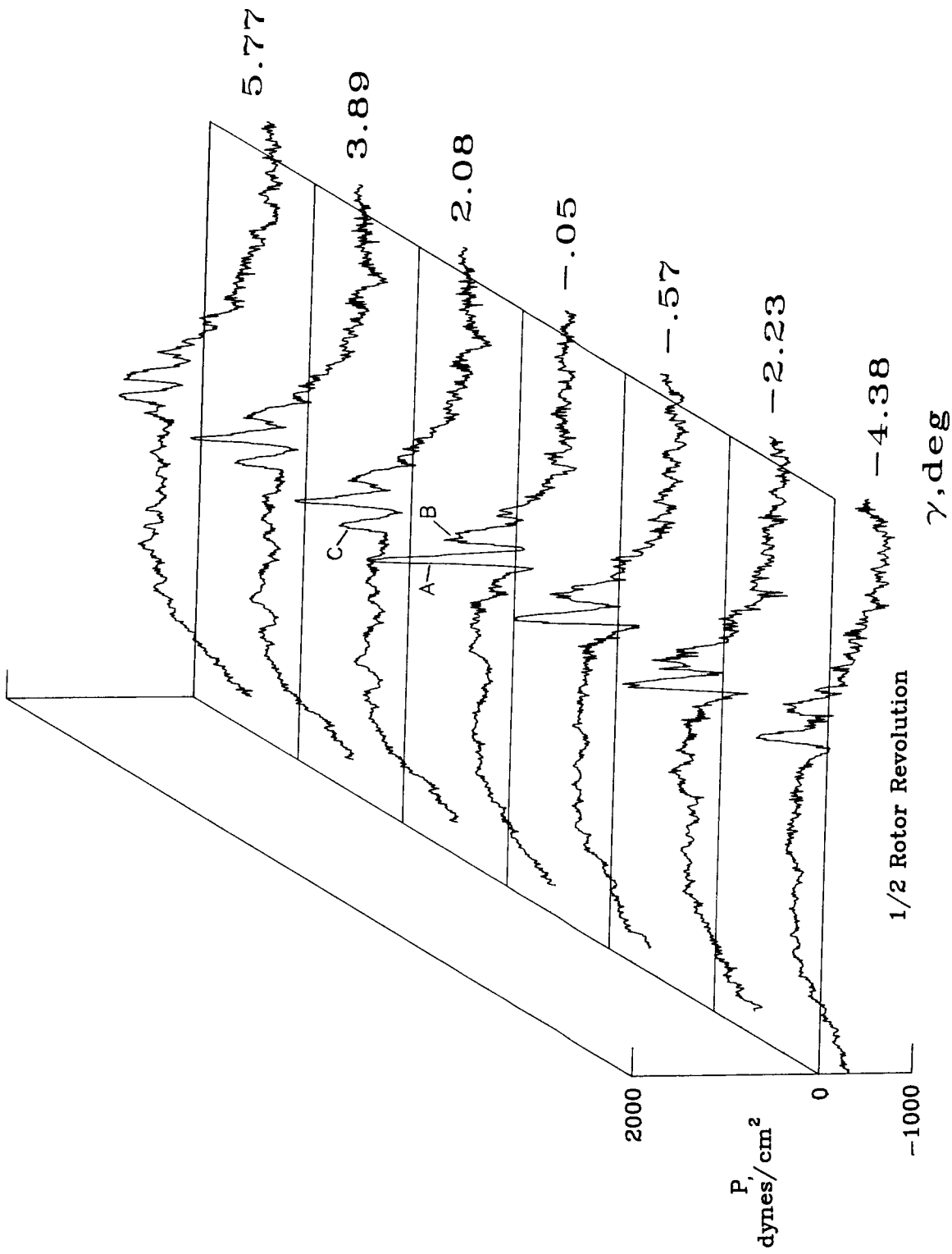
Figure A11. Acoustic time history data for advanced rotor system at $\mu = 0.156$ and $C_T = 0.00359$.
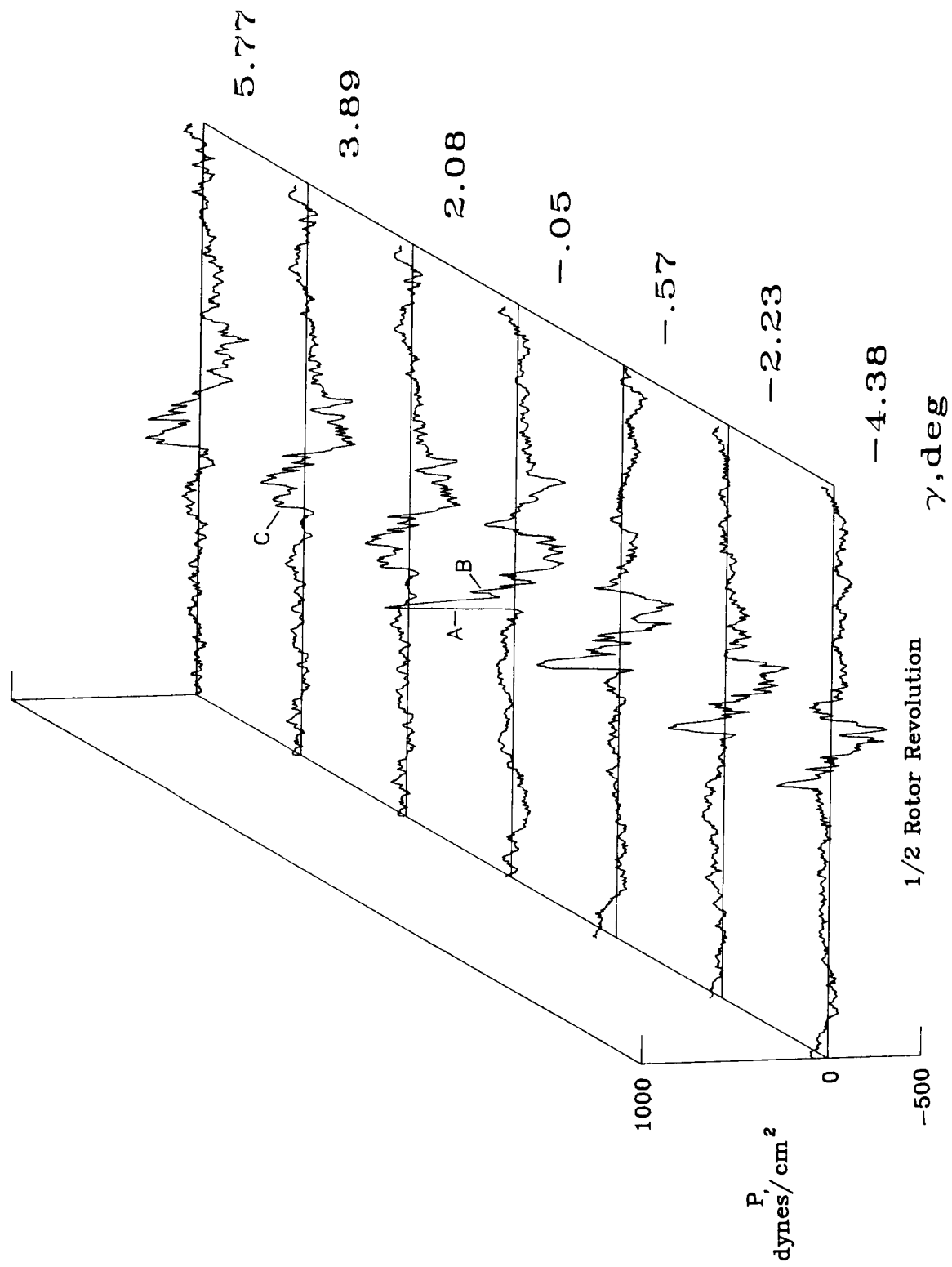
(a) Microphone 2.

(b) Microphone 6.

Figure A11. Continued.
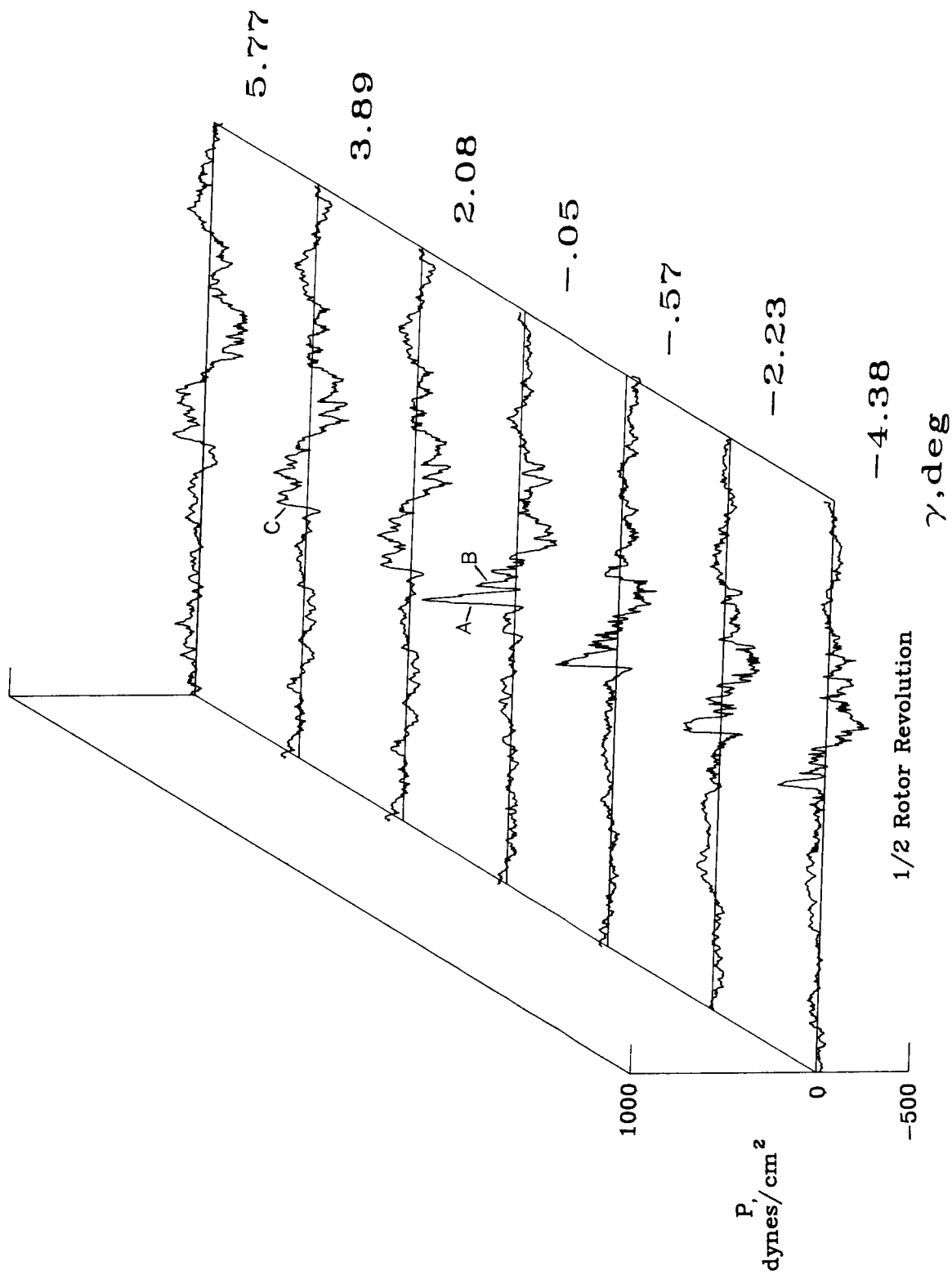
(c) Microphone 7.

Figure A11. Continued.

(d) Microphone 8.

Figure A11. Concluded.

BVI

A   +

B   O

r/R

.25
.50
.75
1.0

0°
30°
60°
90°
120°
150°
180°
210°
240°
270°
300°
330°
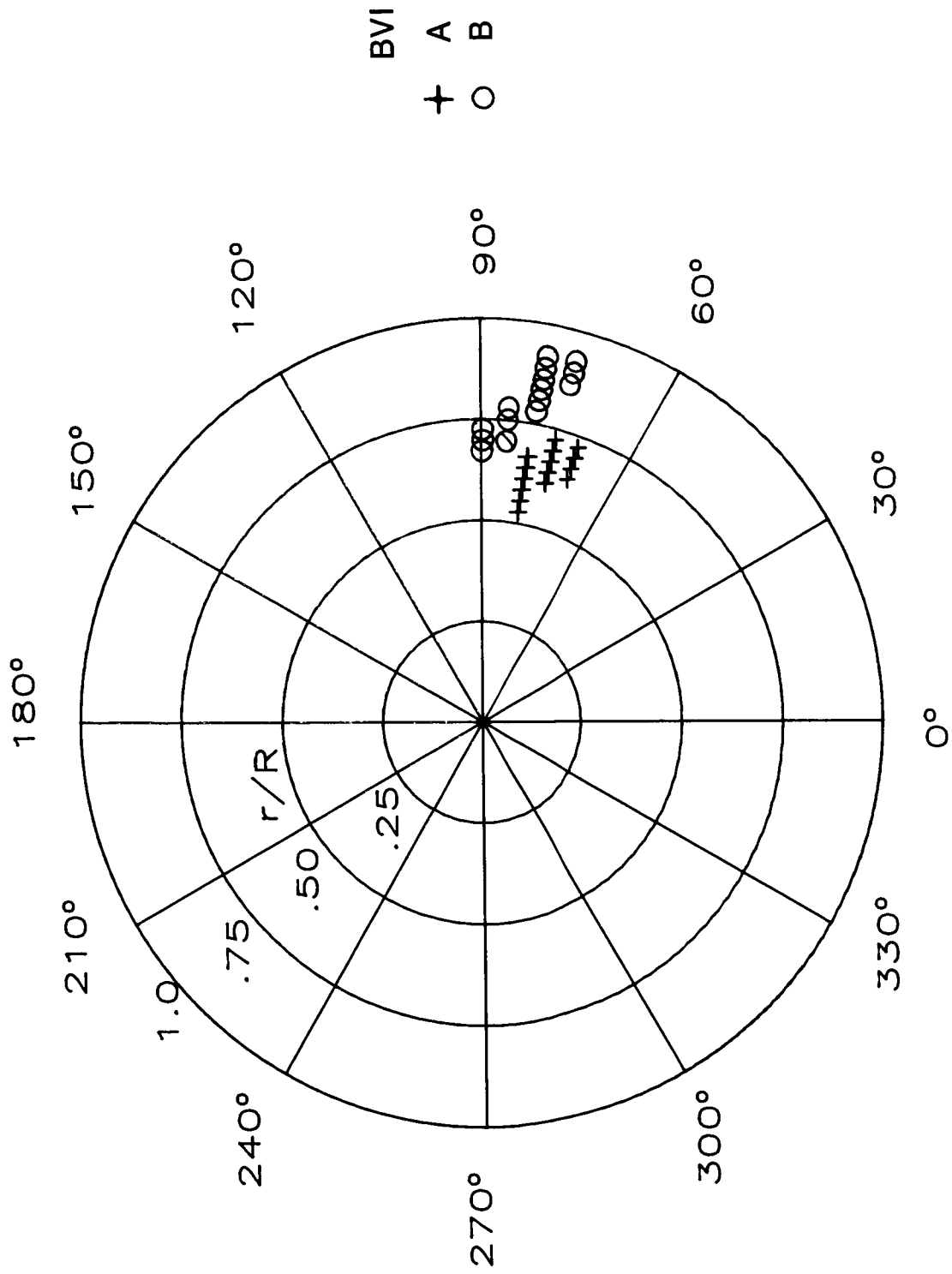
(a) $\mu = 0.104$ and $C_T = 0.00313$.

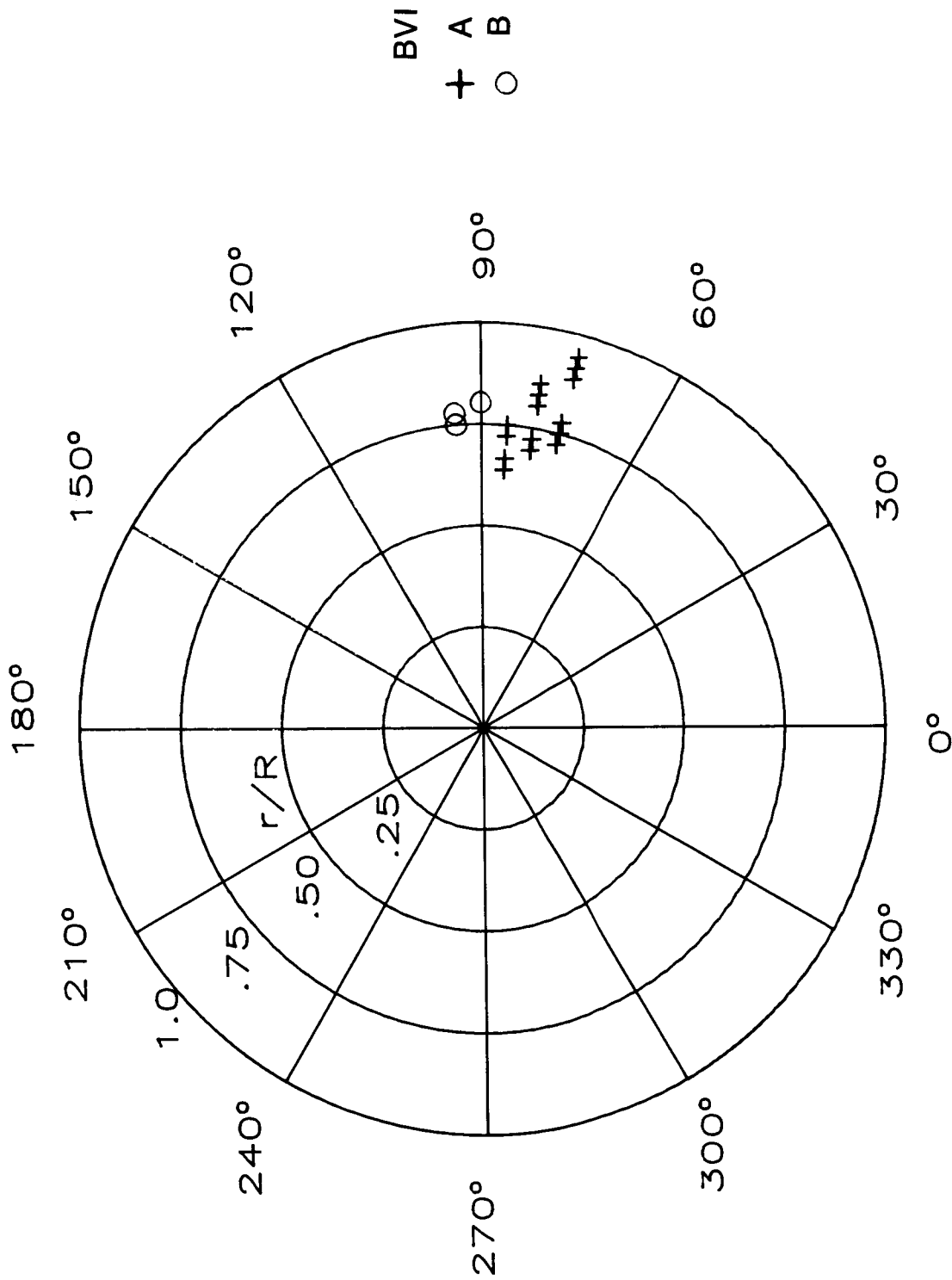Figure A12. Source-location results for standard rotor system.
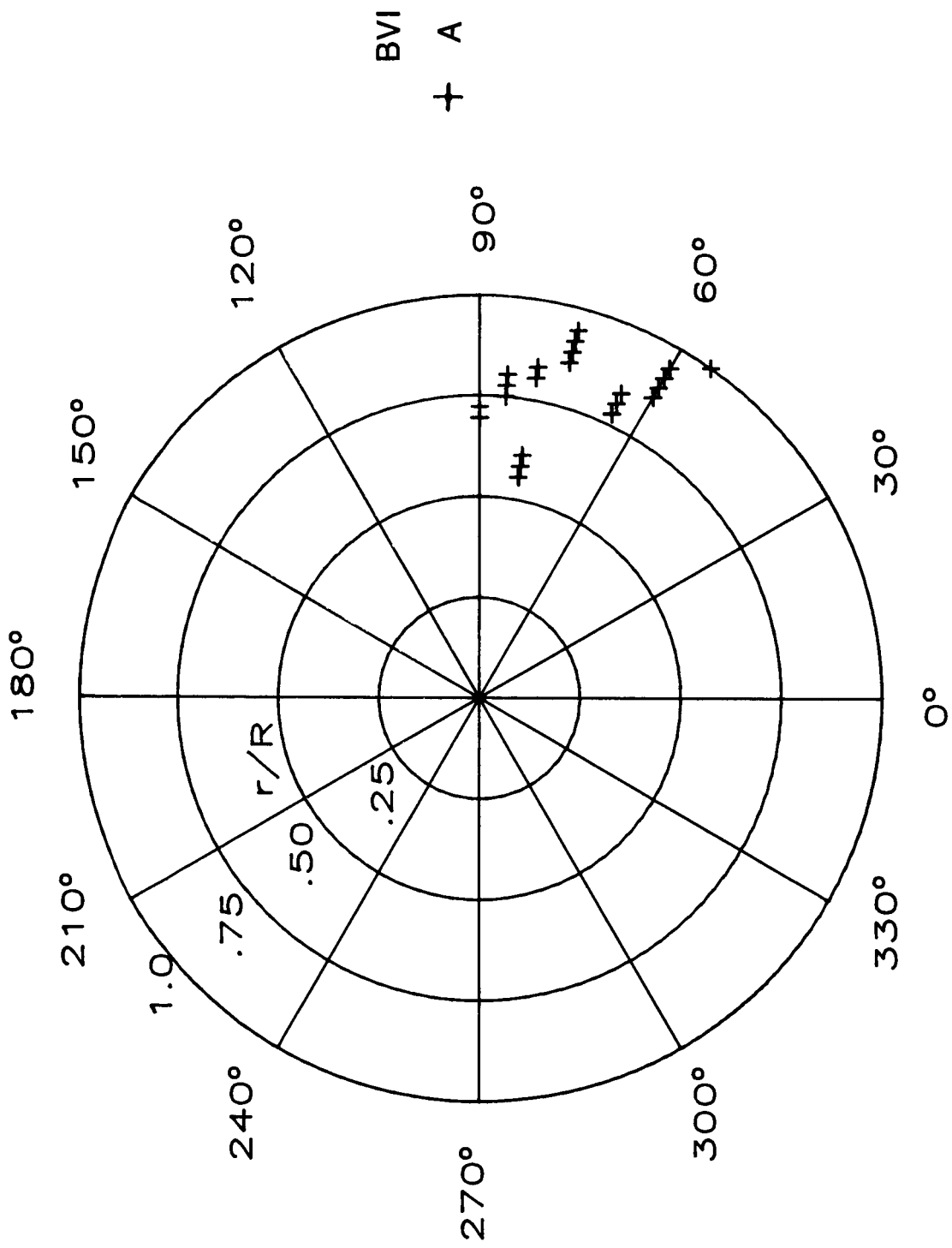
(b) $\mu = 0.103$ and $C_T = 0.00363$.

Figure A12. Continued.
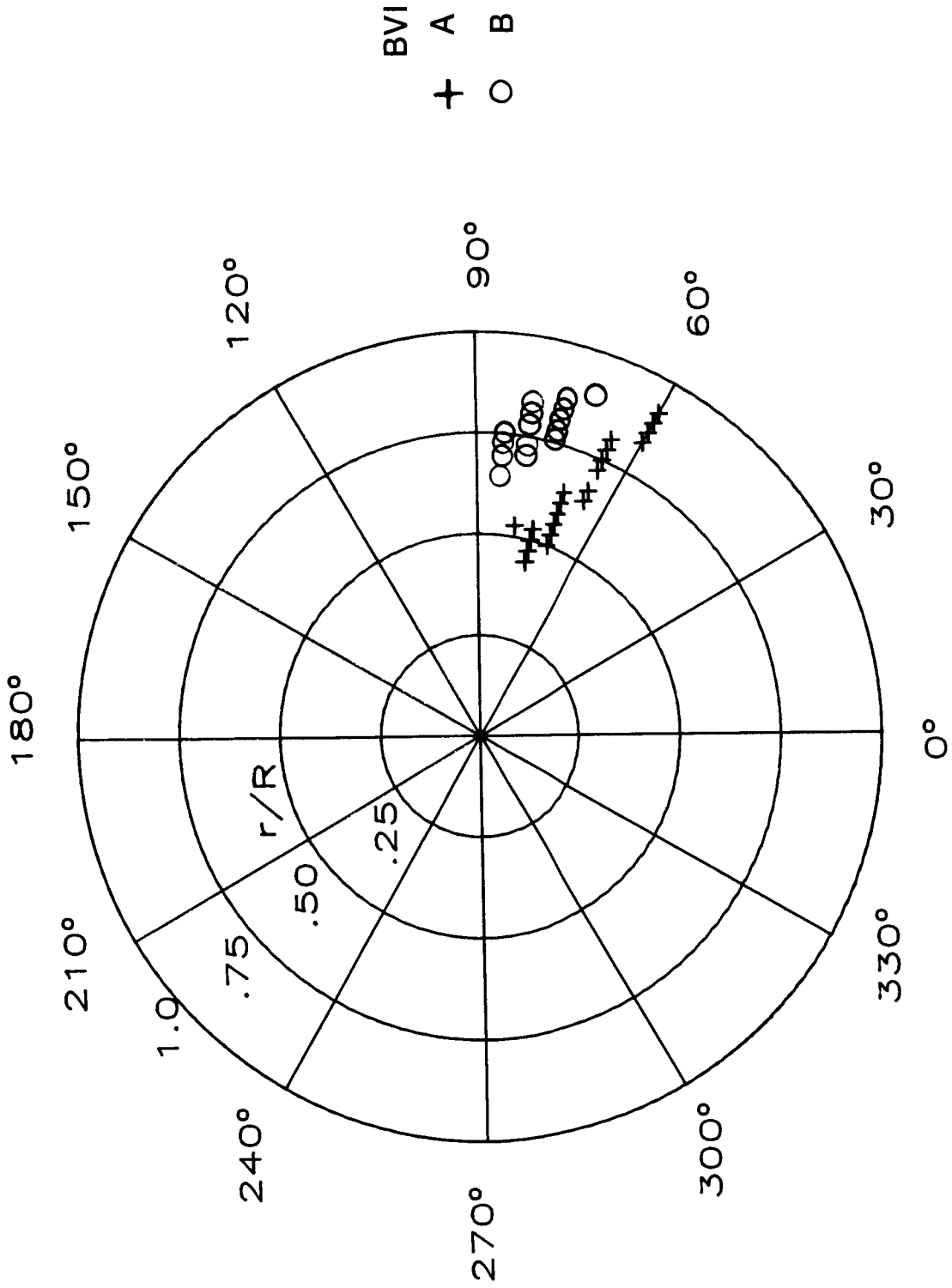
(c) $\mu = 0.115$ and $C_T = 0.00313$.

Figure A12. Continued.

79
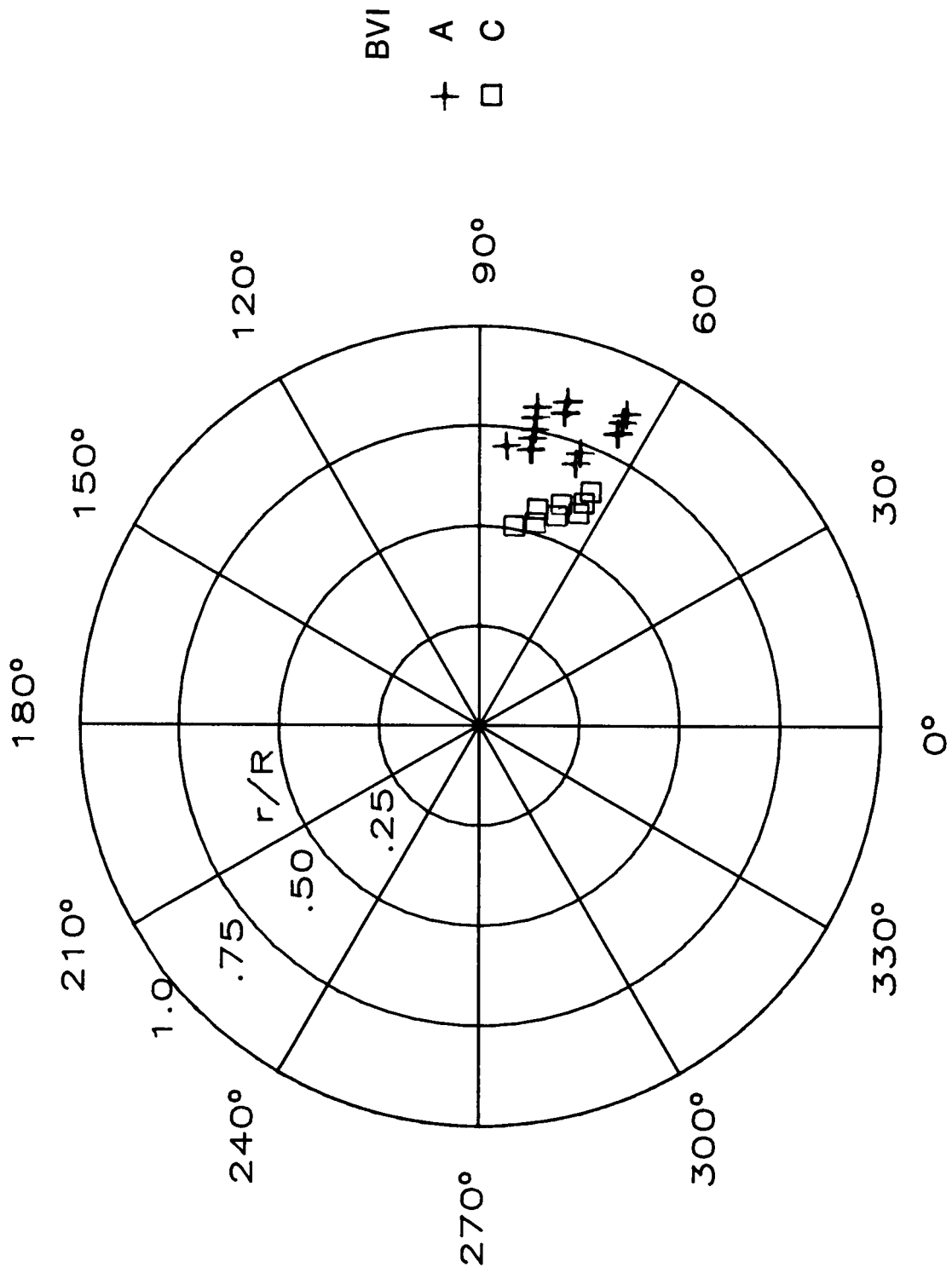
(d) $\mu = 0.115$ and $C_T = 0.00364$.

Figure A12. Continued.
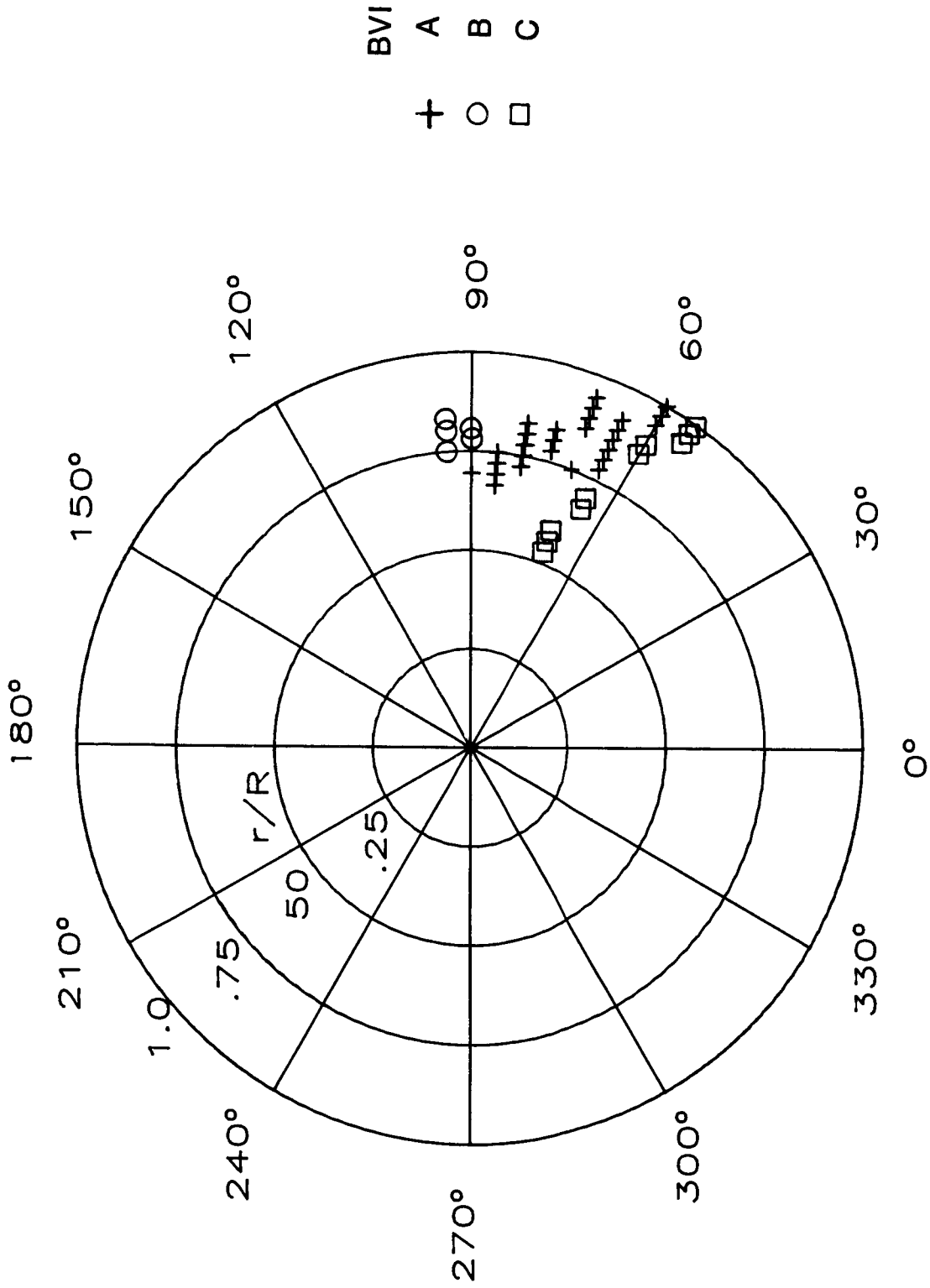
(e) $\mu = 0.124$ and $C_T = 0.00317$.

Figure A12. Continued.
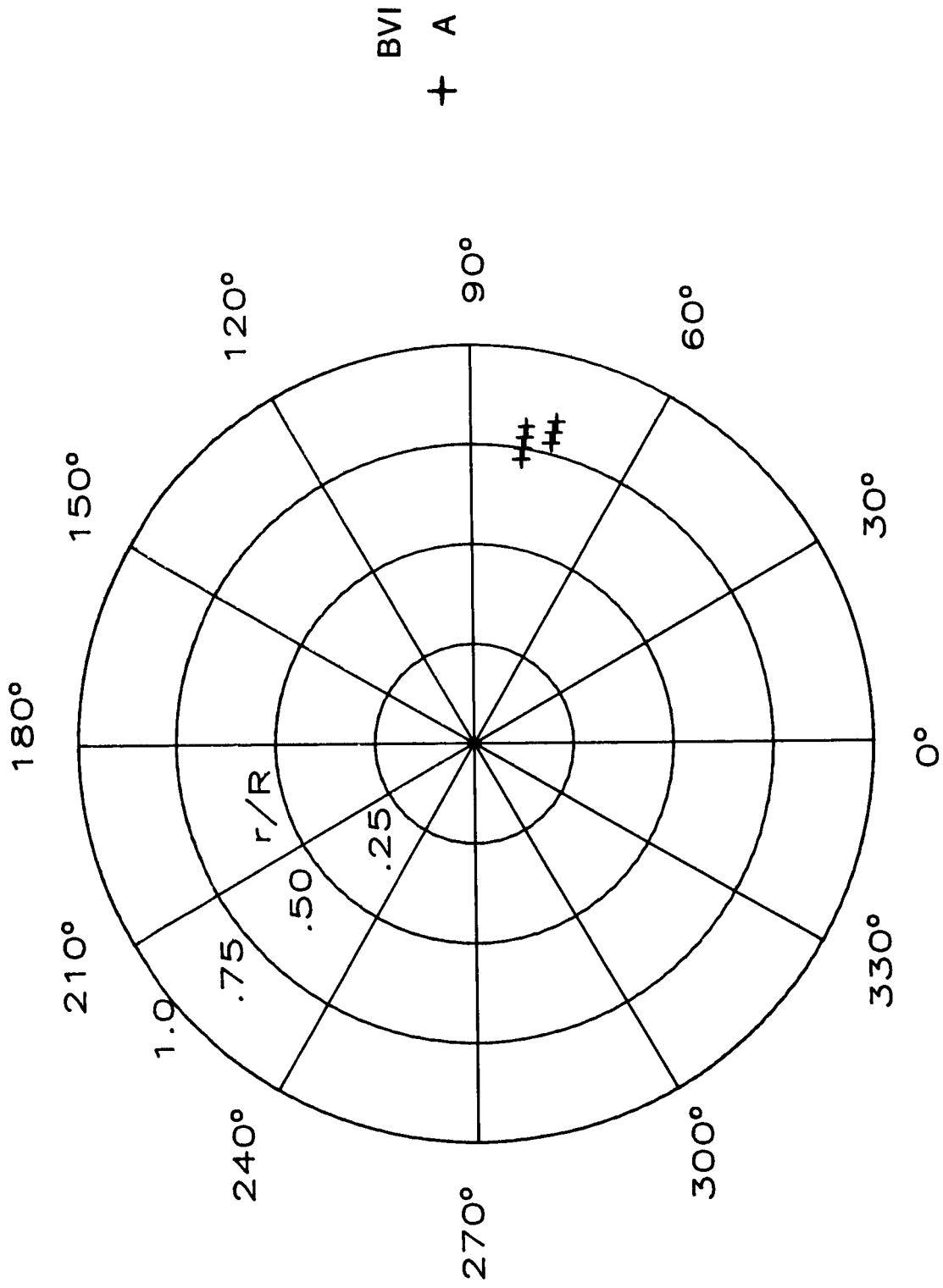
(f) $\mu = 0.124$ and 0.00365.

Figure A12. Continued.
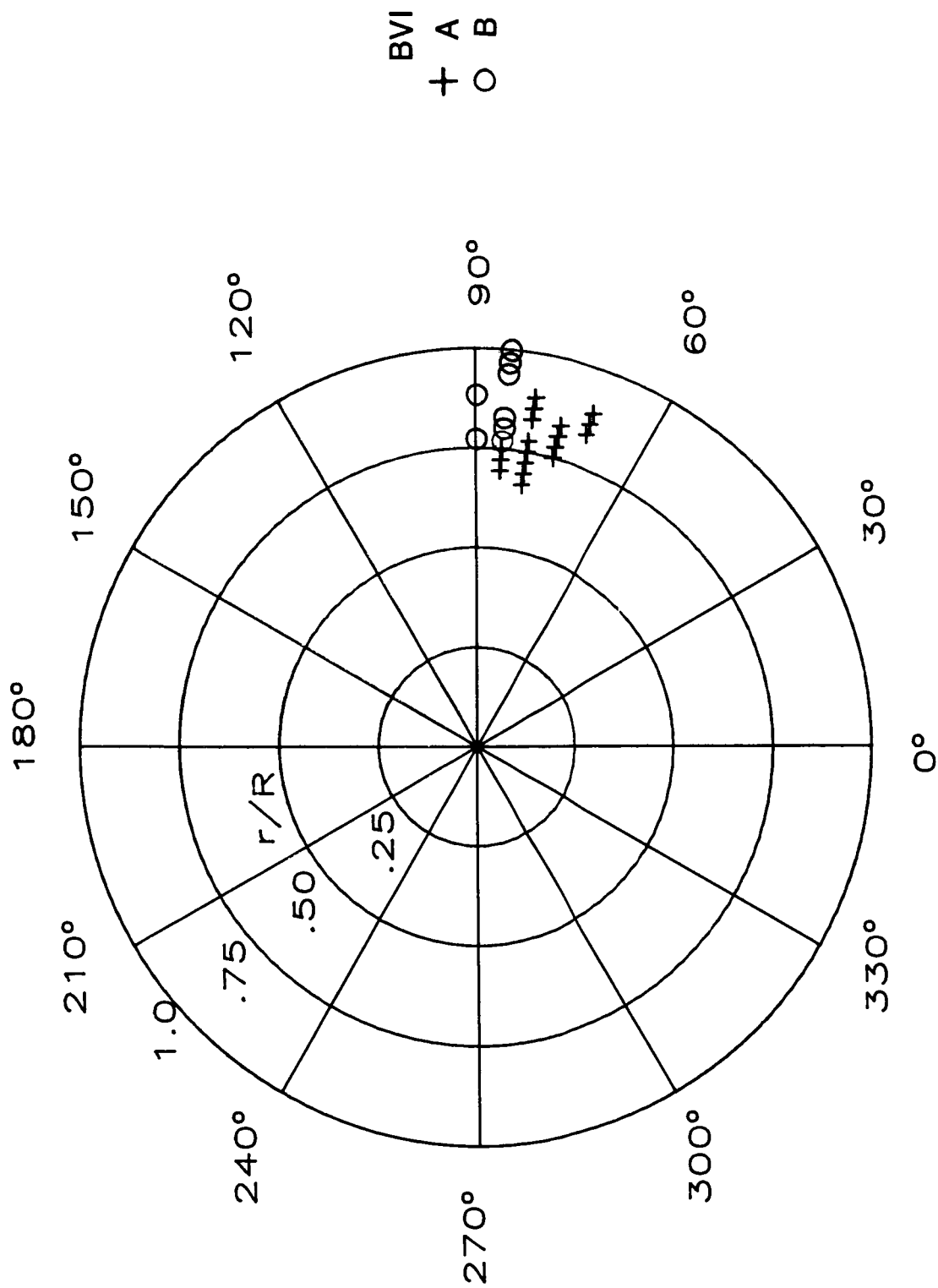
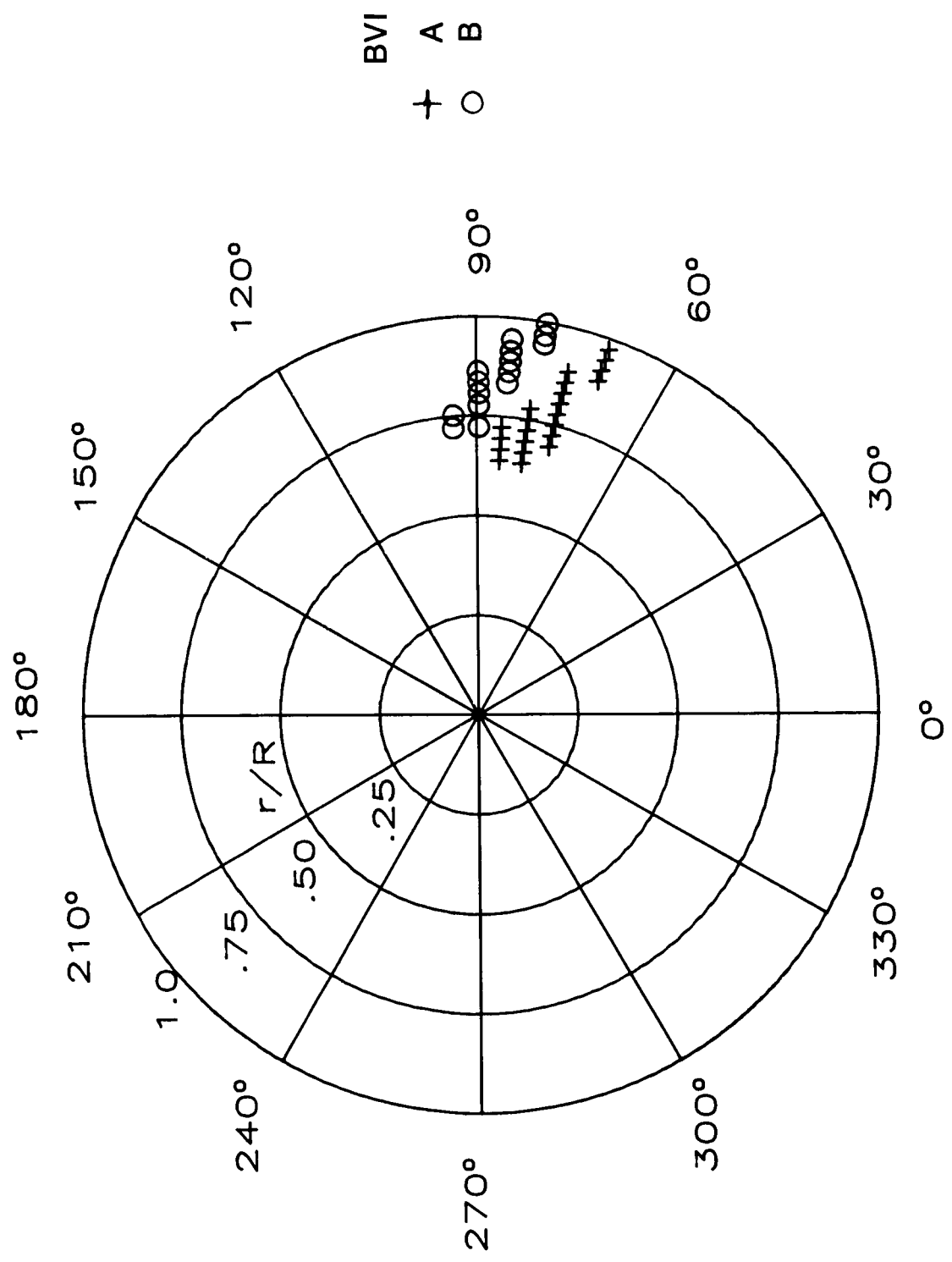(g) $\mu = 0.135$ and $C_T = 0.00320$.

Figure A12. Continued.
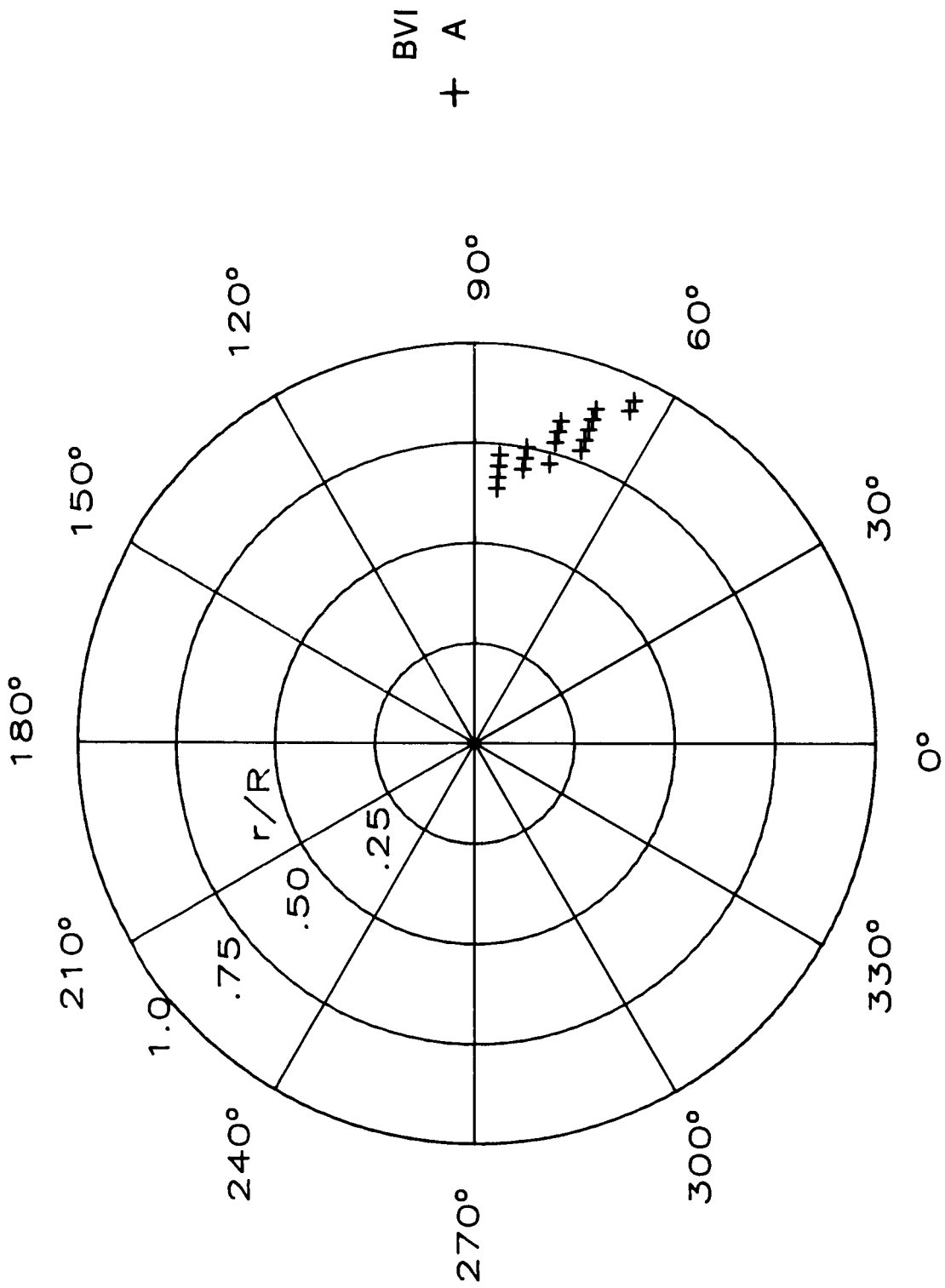
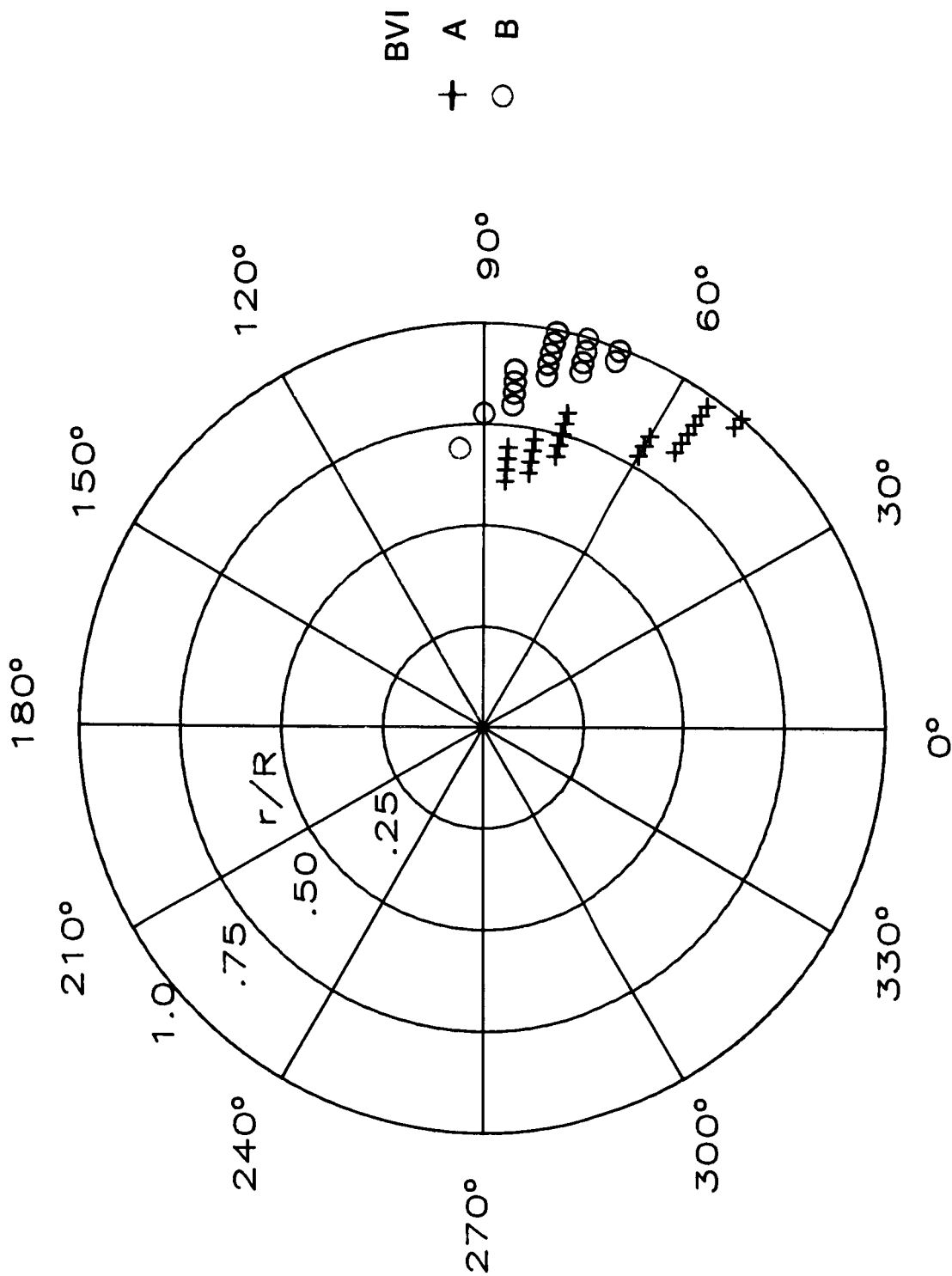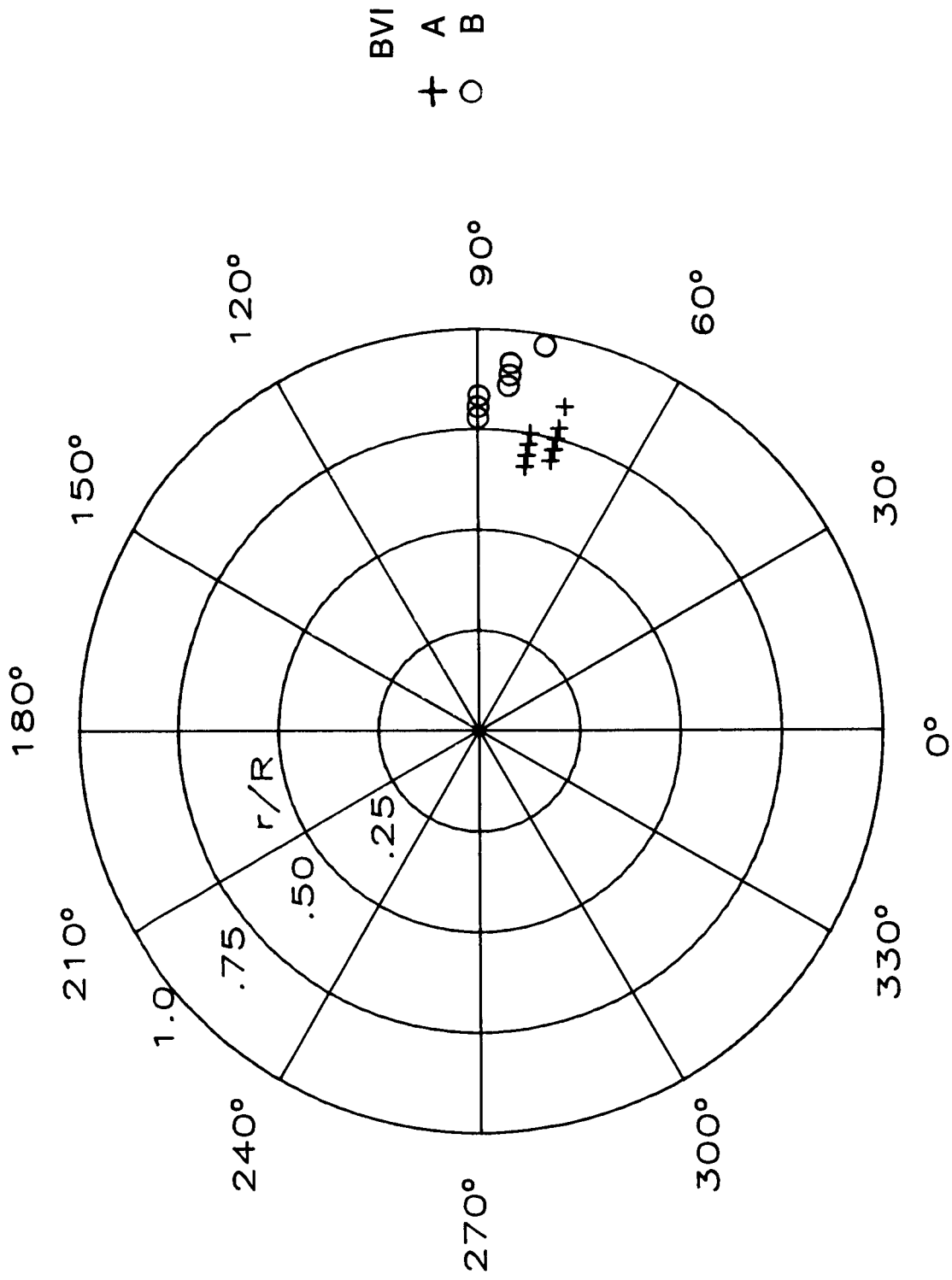(h) $\mu = 0.135$ and $C_T = 0.00361$.

Figure A12. Continued.

(i) $\mu = 0.145$ and $C_T = 0.00320$. Continued.

Figure A12. Continued.

(j) $\mu = 0.155$ and $C_T = 0.00320$.

Figure A12. Continued.

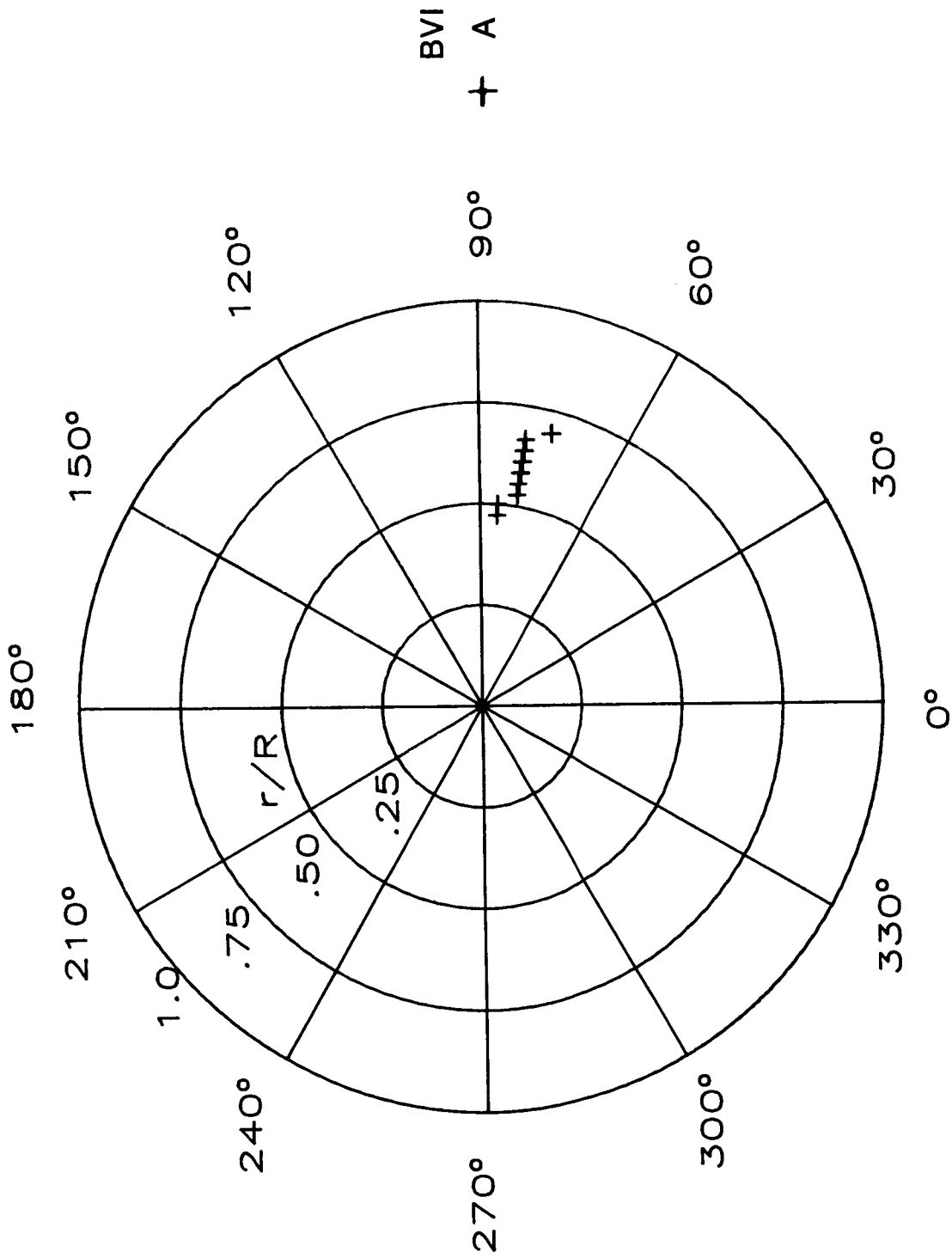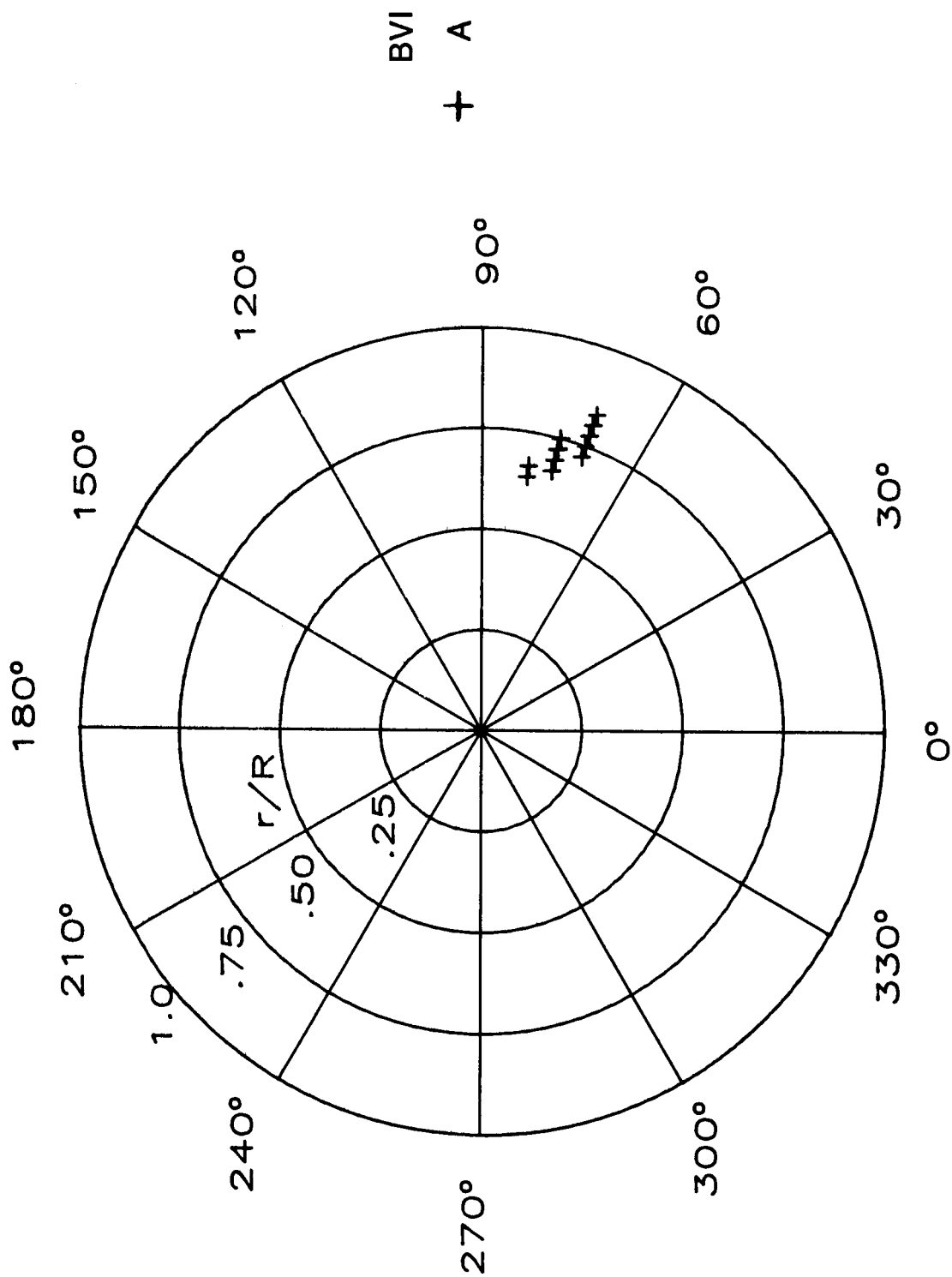(k) $\mu = 0.166$ and $C_T = 0.00318$.

Figure A12. Continued.

BVI

A +
B ○

r/R

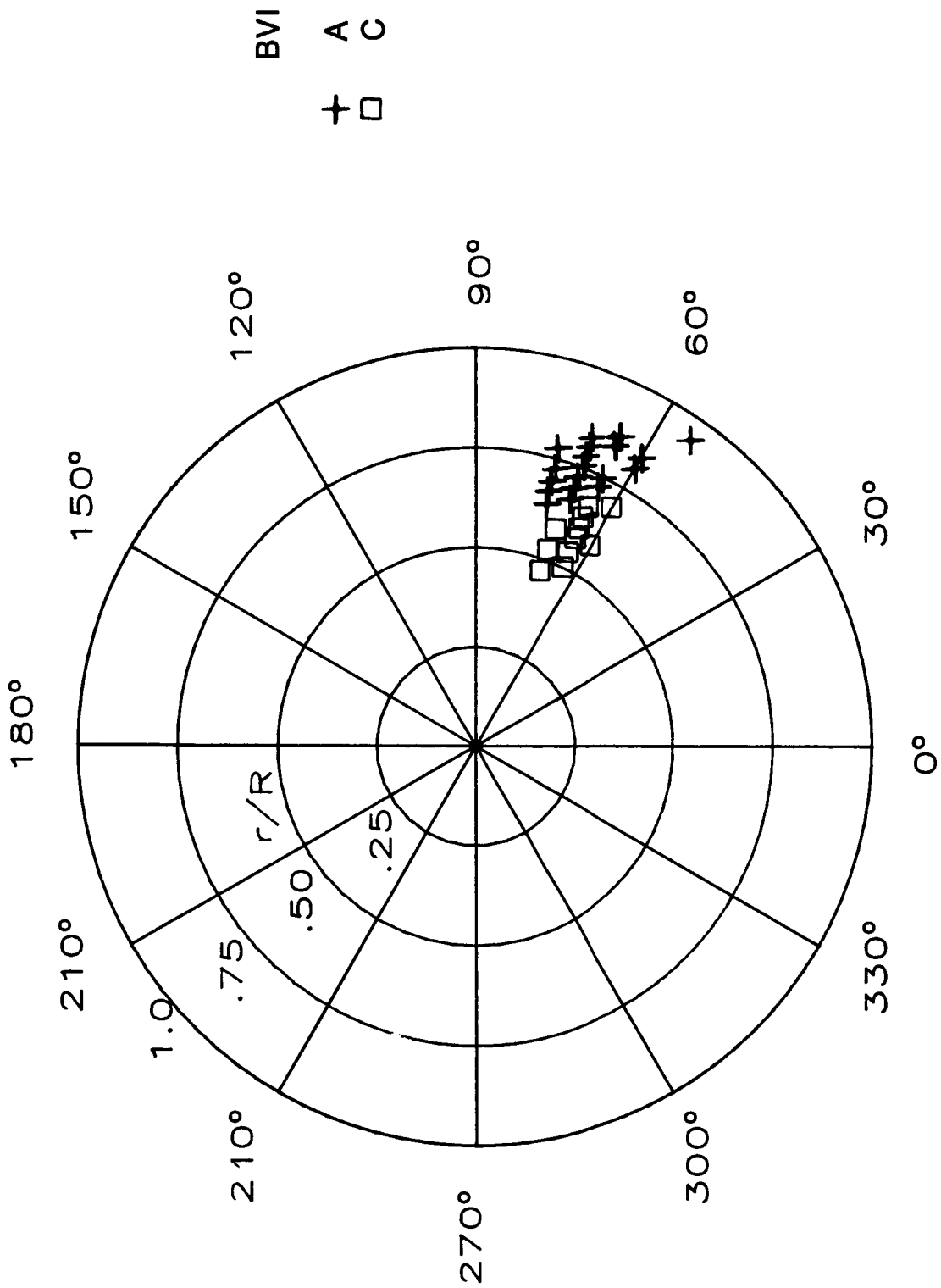(l) $\mu = 0.155$ and $C_T = 0.00355$.

Figure A12. Continued.

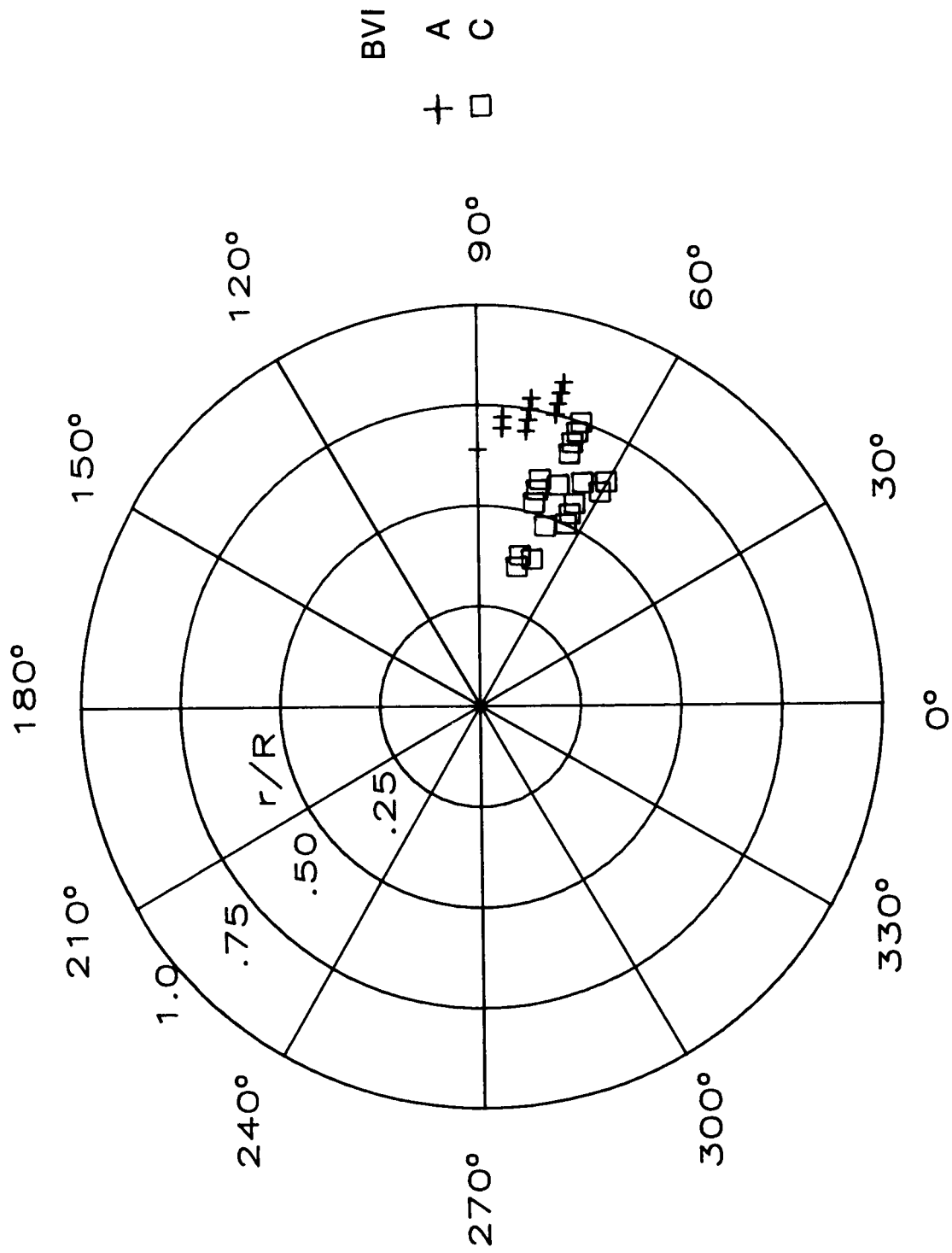(m) $\mu = 0.186$ and $C_T = 0.00317$.

Figure A12. Continued.

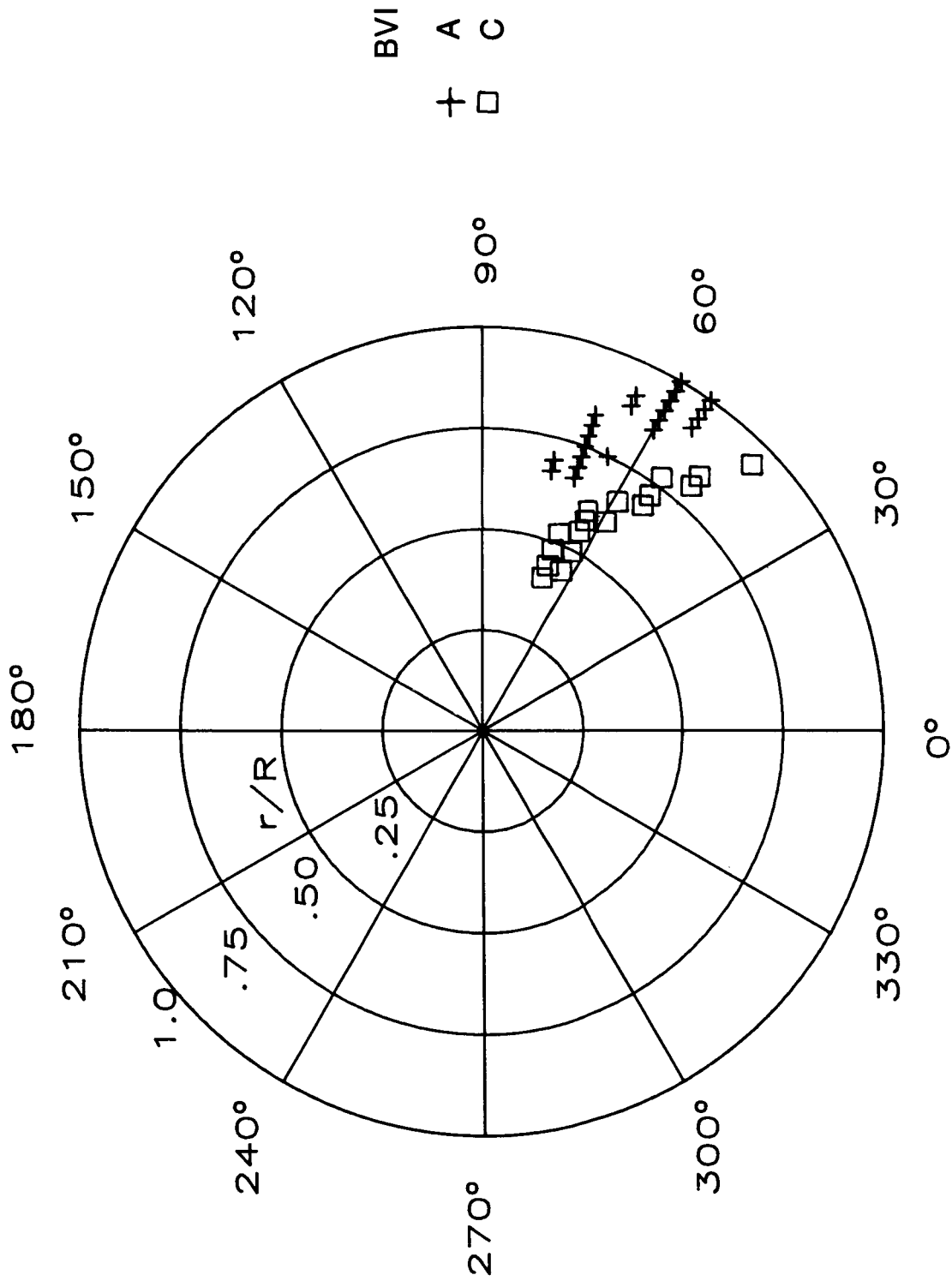(n) $\mu = 0.167$ and $C_T = 0.00358$.

Figure A12. Concluded.

(a) $\mu = 0.104$ and $C_T = 0.00309$.

Figure A13. Source-location results for advanced rotor system.

(b) $\mu = 0.103$ and $C_T = 0.00358$.

Figure A13. Continued.

(c) $\mu = 0.114$ and $C_T = 0.00315$.

Figure A13. Continued.

(d) $\mu = 0.114$ and $C_T = 0.00360$.

Figure A13. Continued.

BVI

+ A

(e) $\mu = 0.125$ and $C_T = 0.00312$.

Figure A13. Continued.

BVI

+ A

120°

90°

150°

60°

180°

30°

r/R

.25

.50

.75

1.0

210°

0°

240°

330°

270°

300°

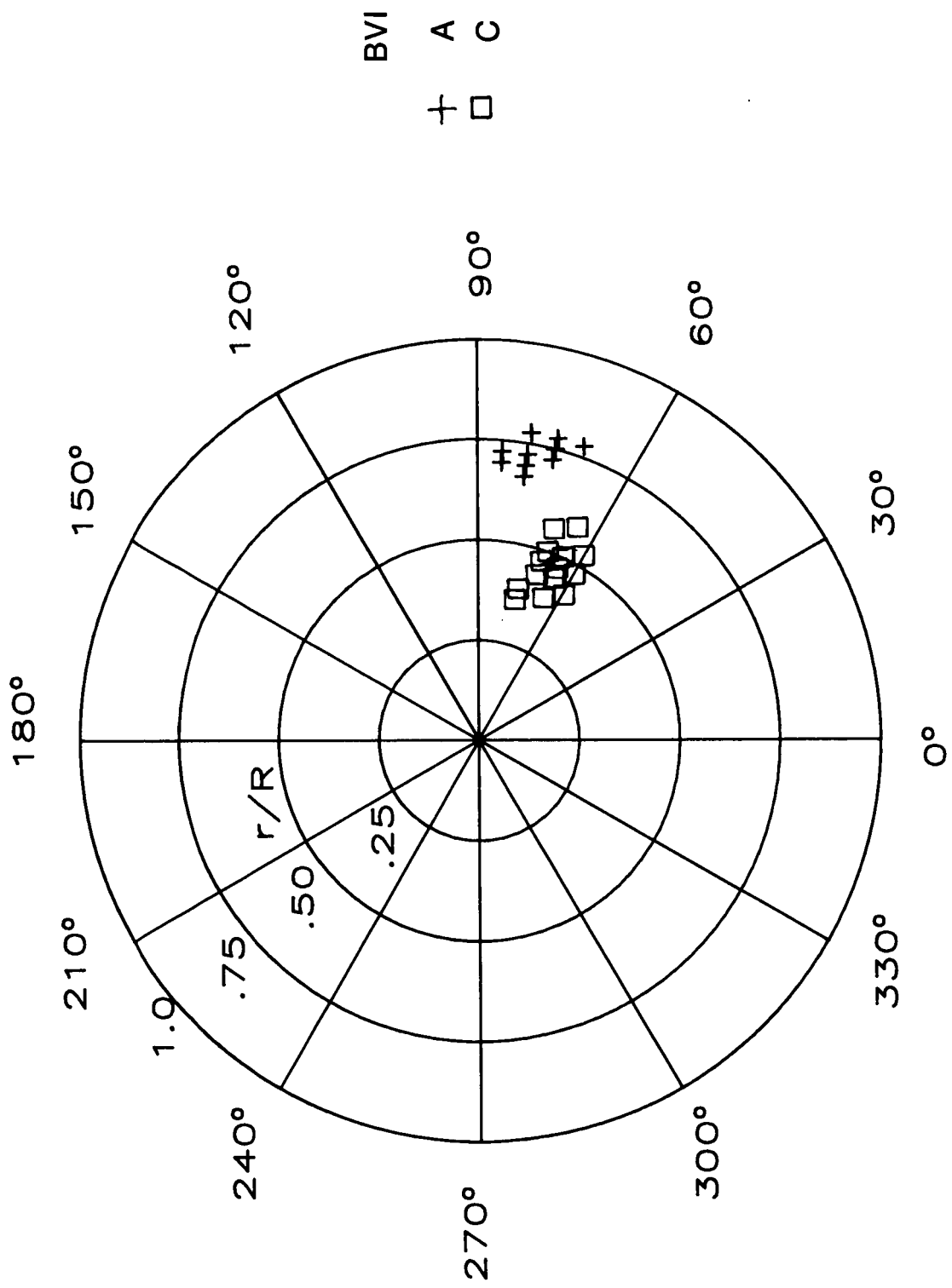(f) $\mu = 0.127$ and $C_T = 0.00361$.

Figure A13. Continued.

C-2

(g) $\mu = 0.134$ and $C_T = 0.00315$.

Figure A13. Continued.

(h) $\mu = 0.135$ and $C_T = 0.00360$.

Figure A13. Continued.
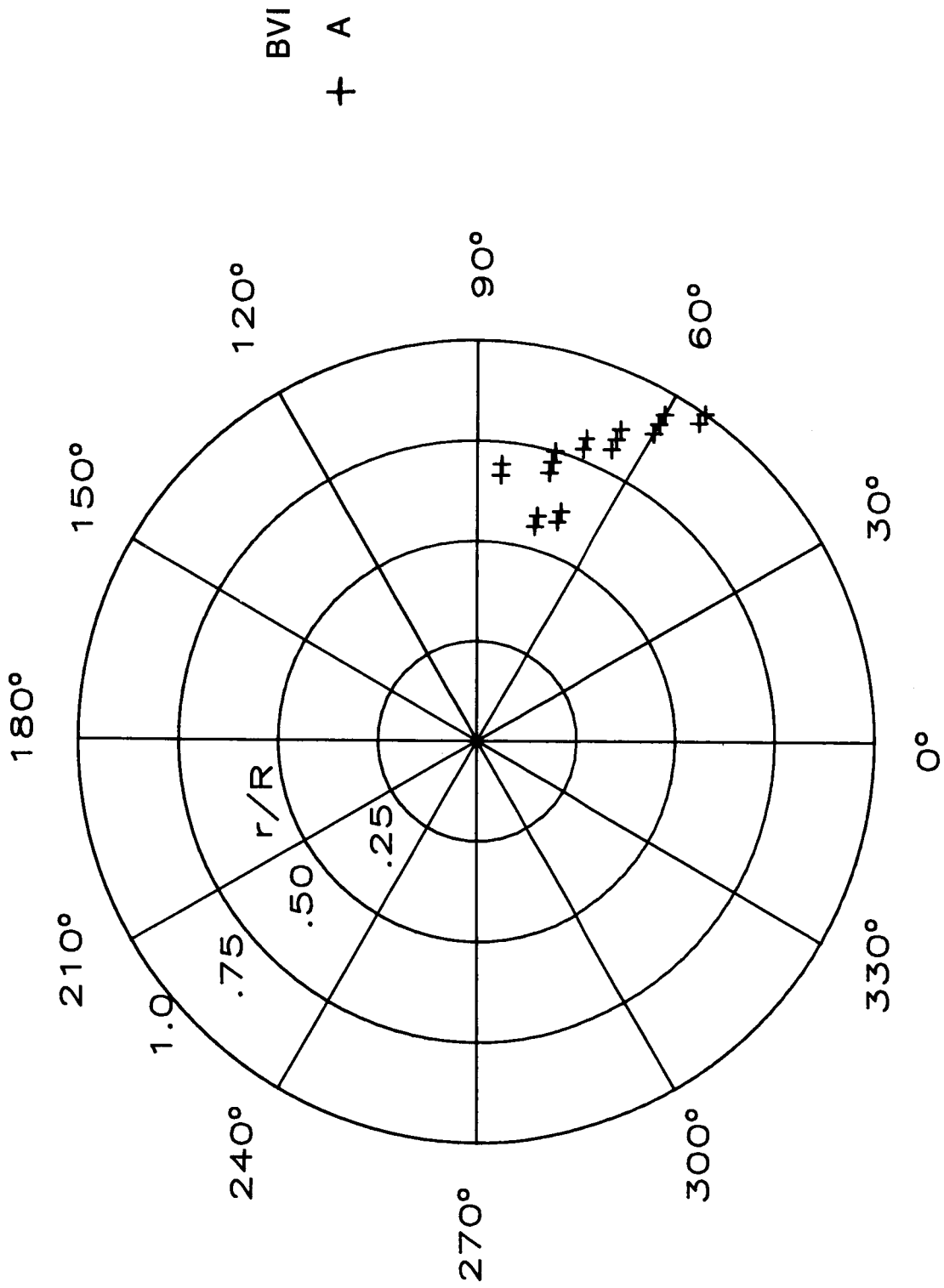
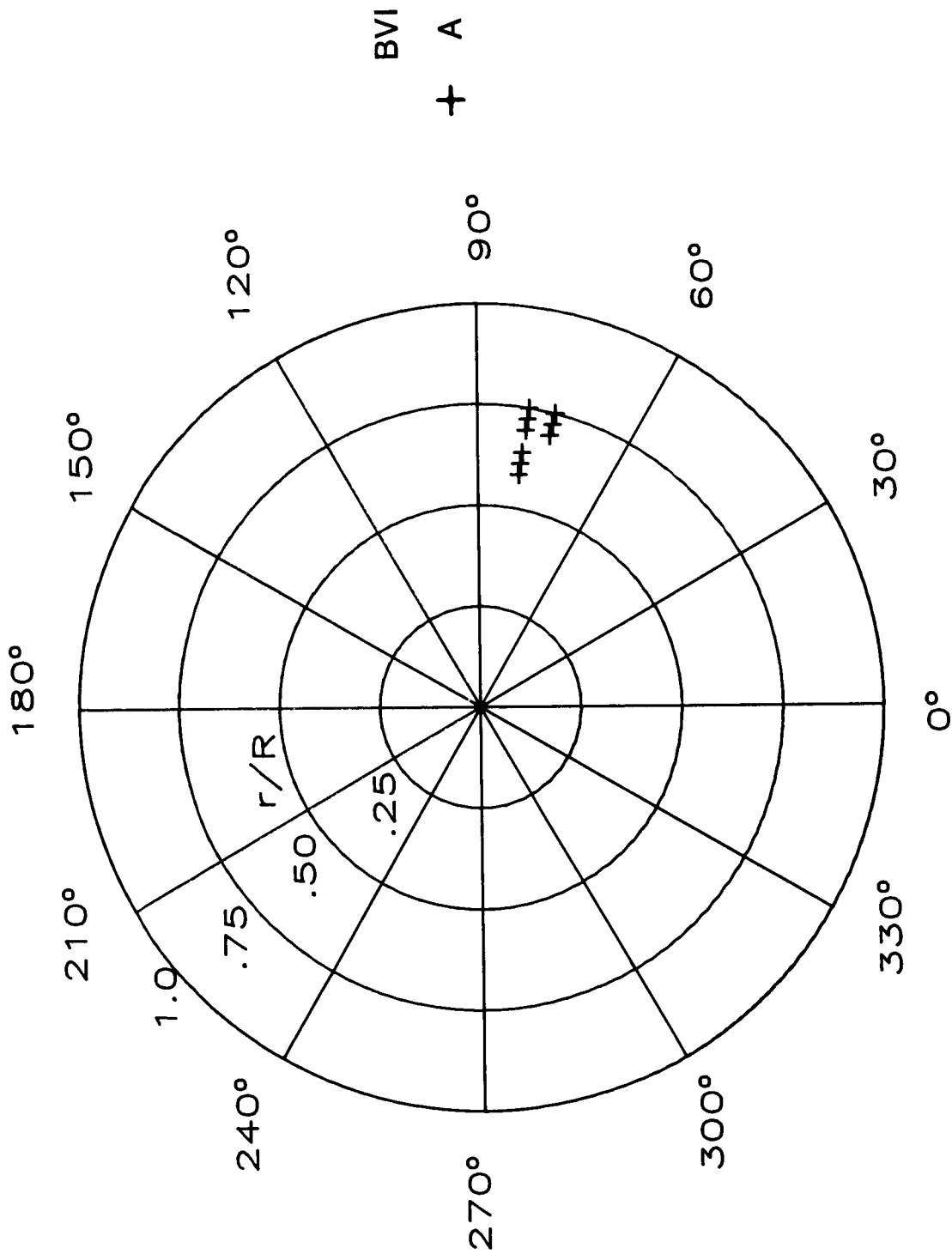(i) $\mu = 0.145$ and $C_T = 0.00308$.

Figure A13. Continued.

(j) $\mu = 0.146$ and $C_T = 0.00361$.
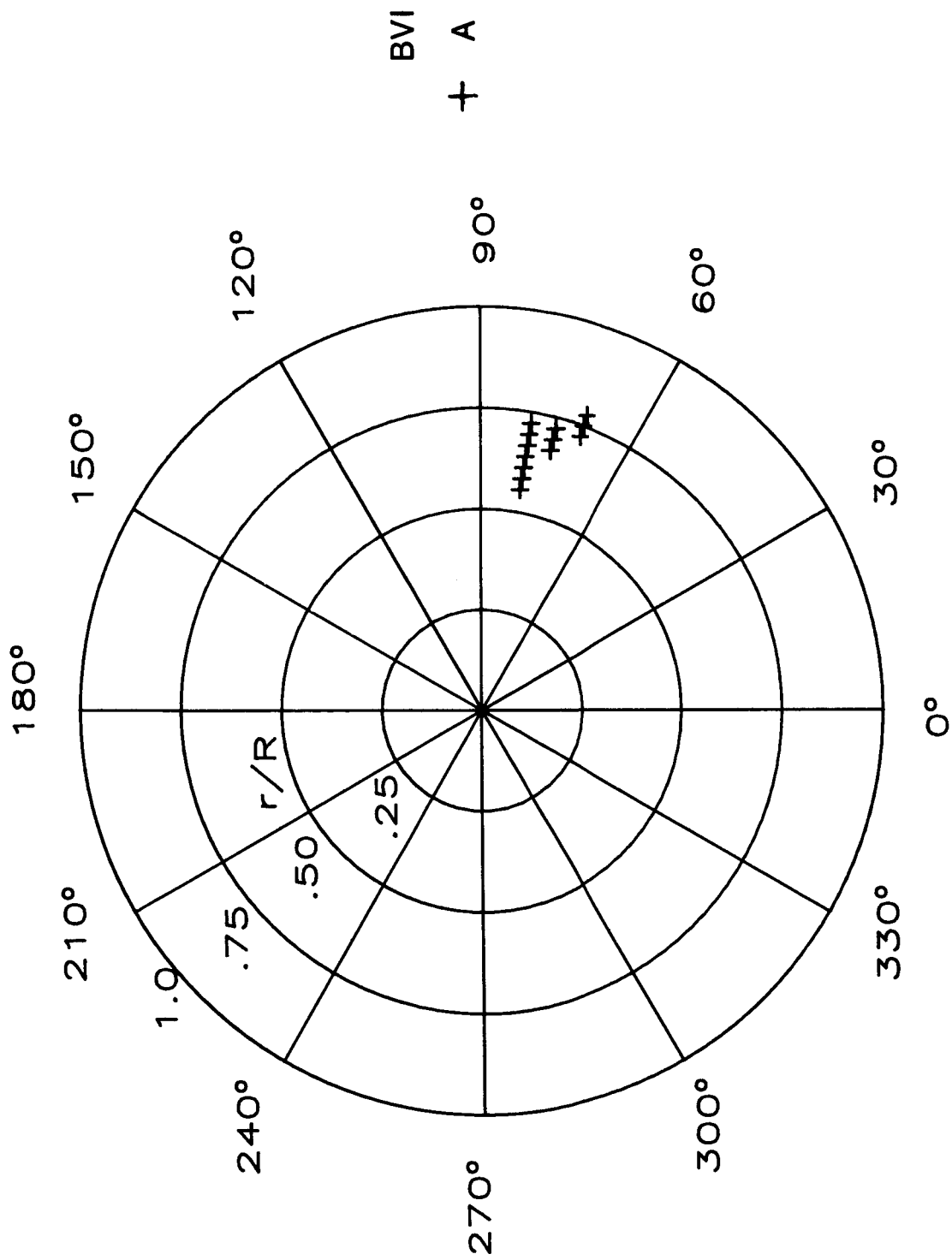
Figure A13. Continued.

(k) $\mu = 0.156$ and $C_T = 0.00319$.

Figure A13. Continued.

(l) $\mu = 0.156$ and $C_T = 0.00359$.
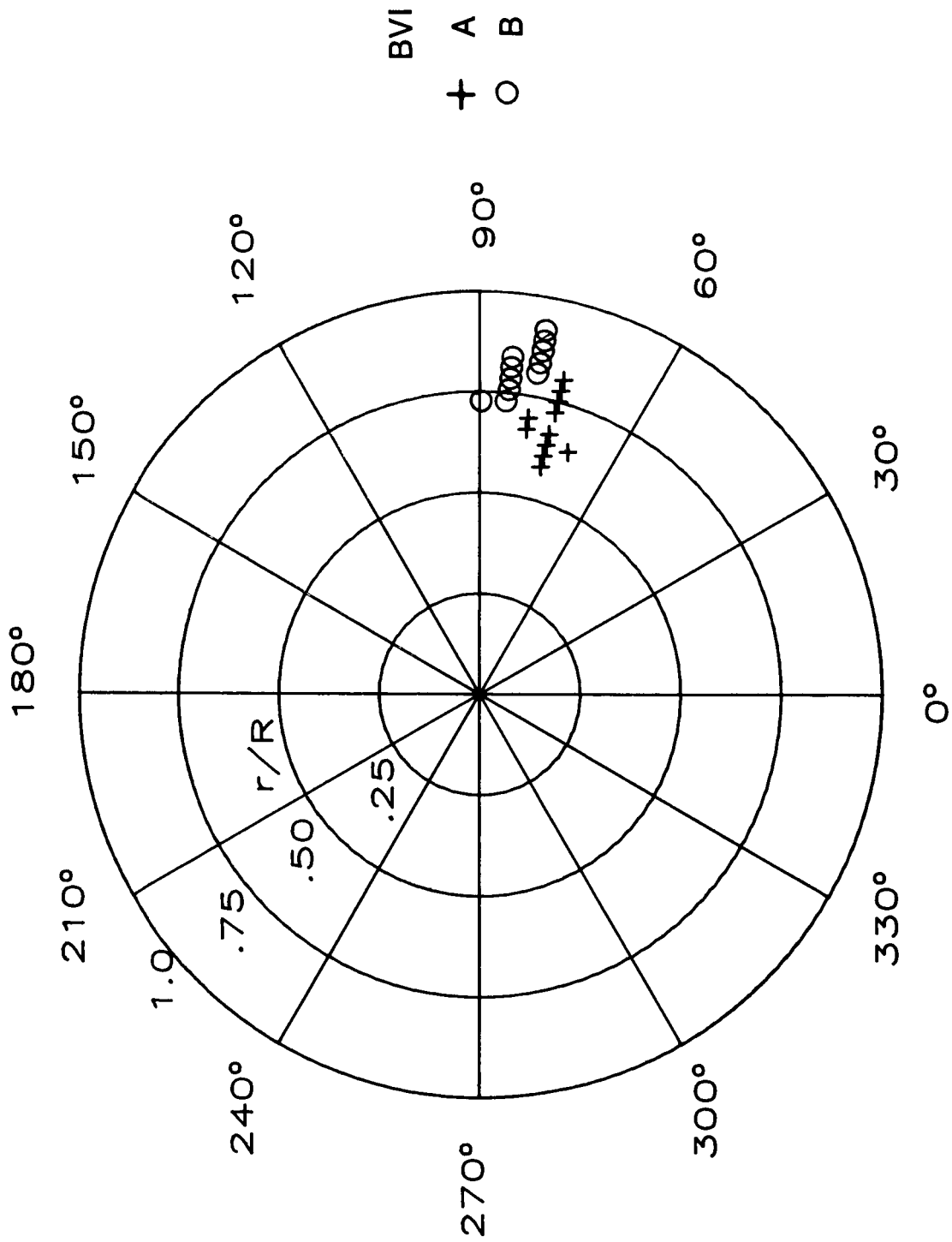
Figure A13. Continued.

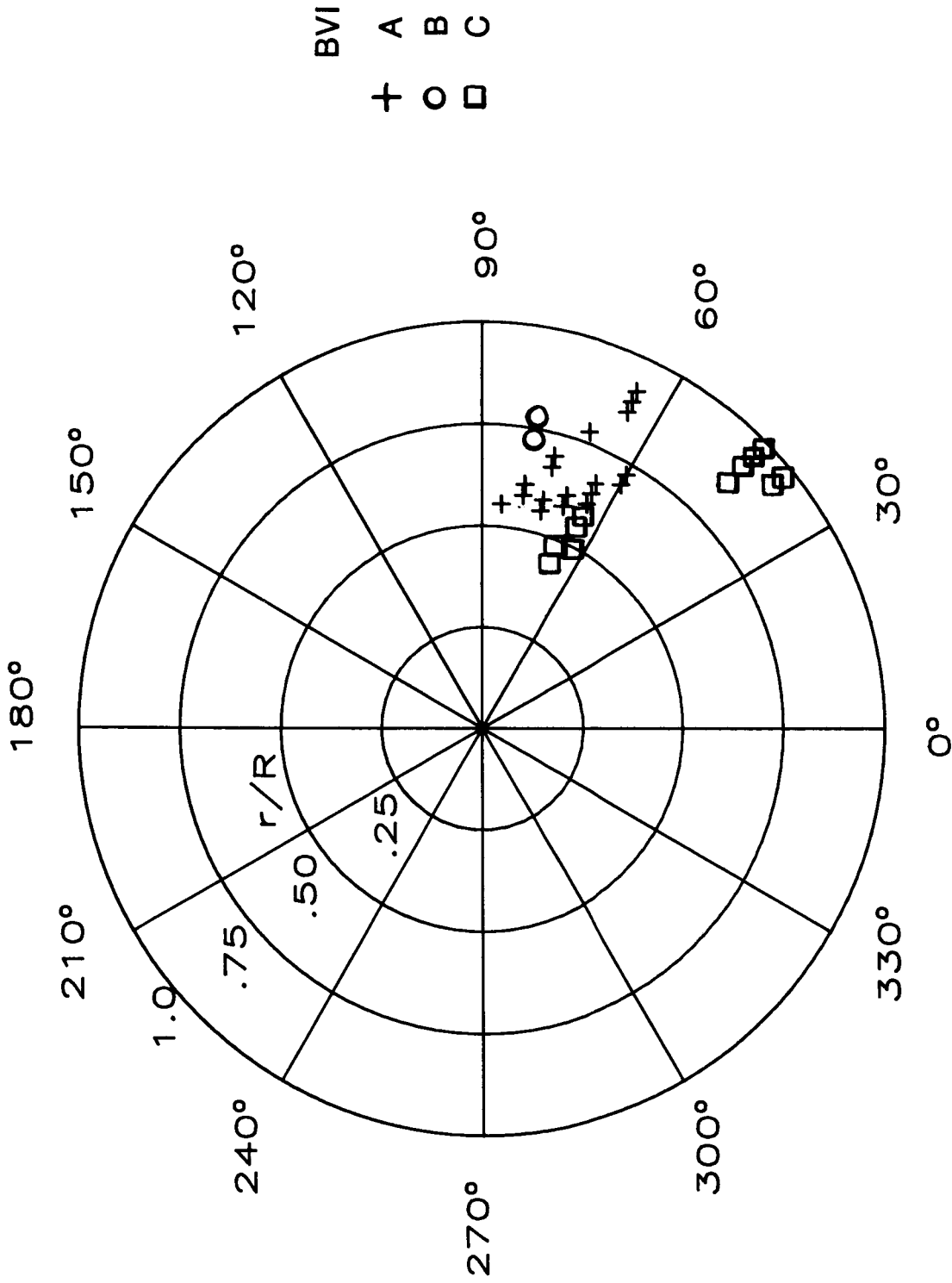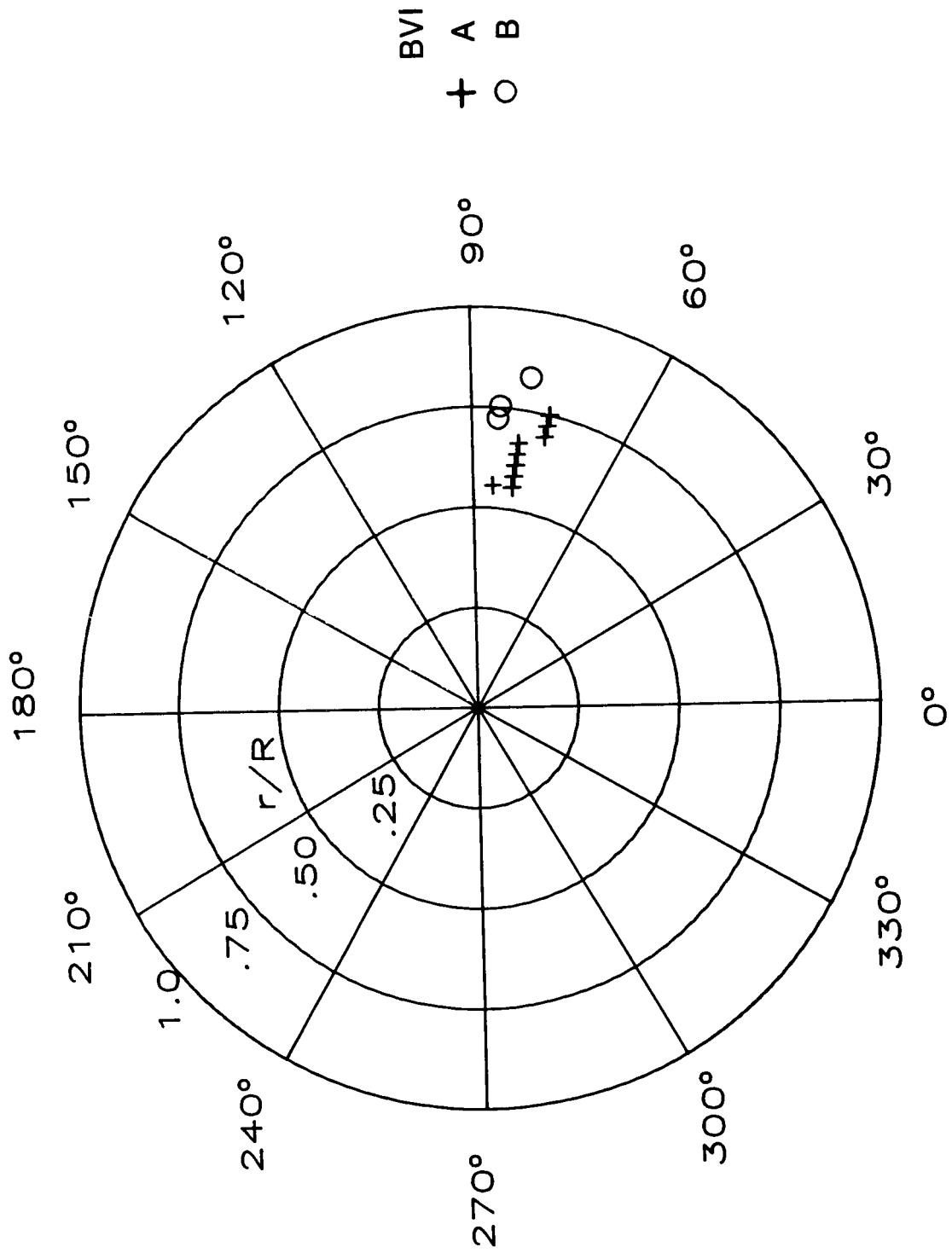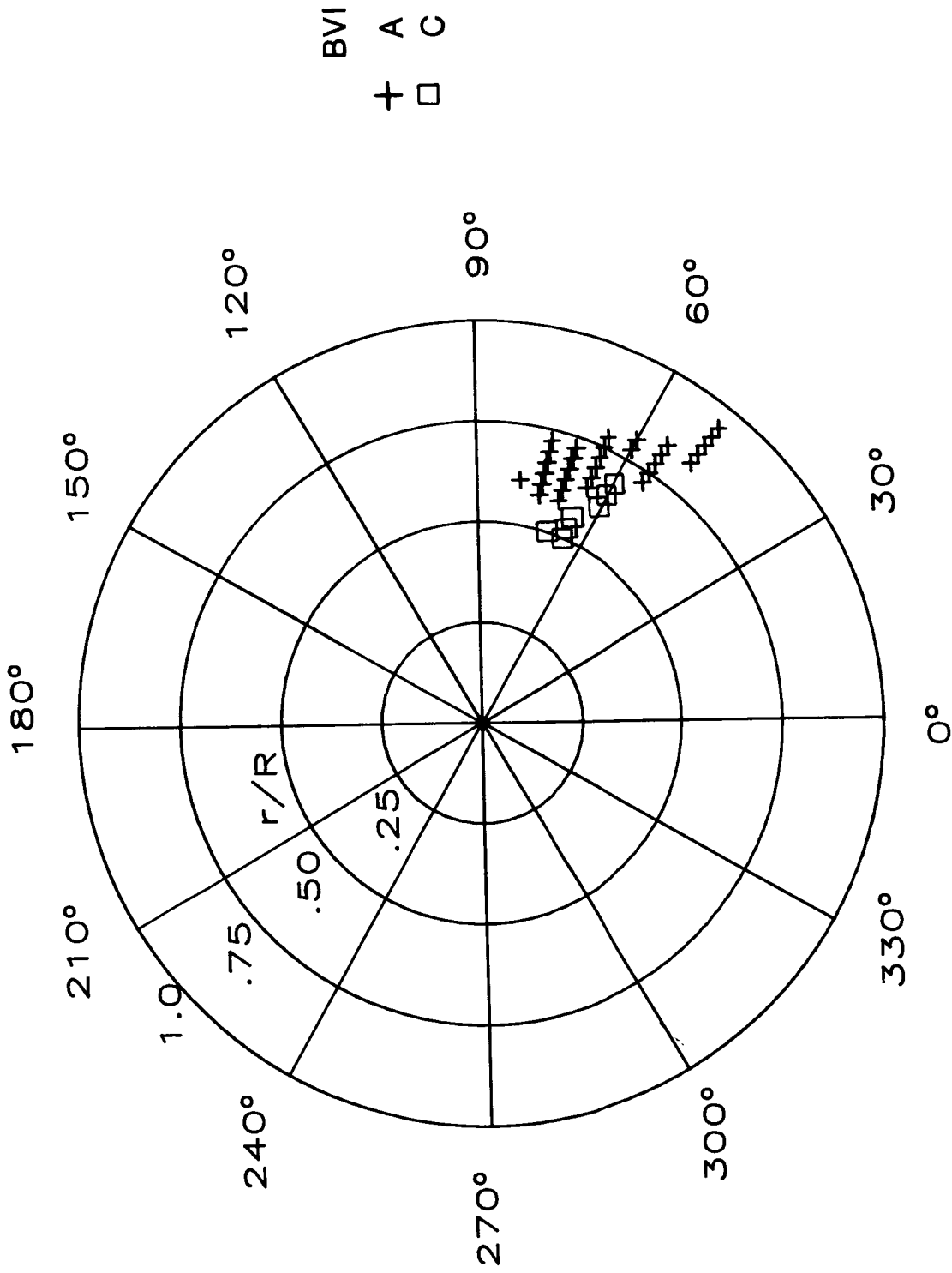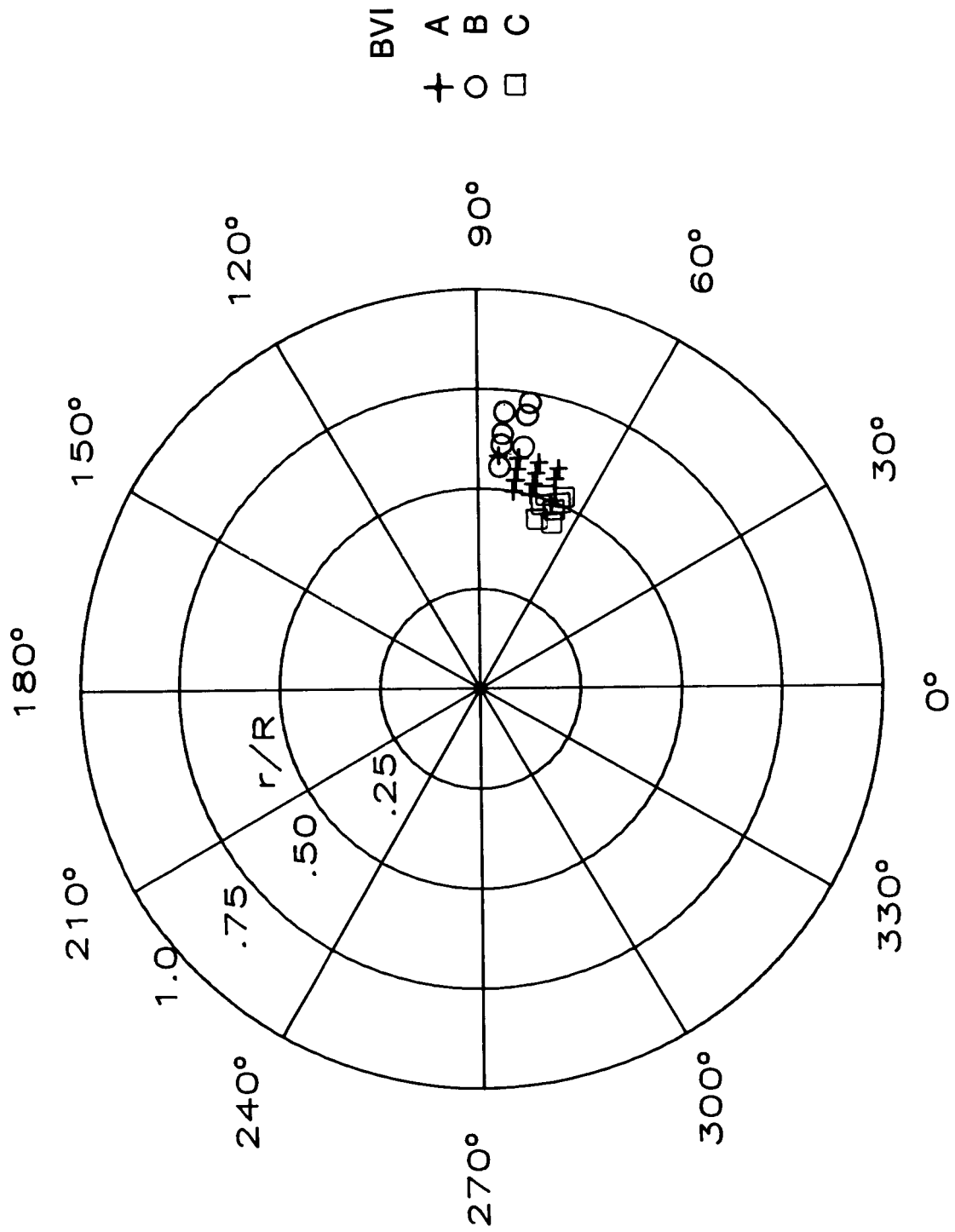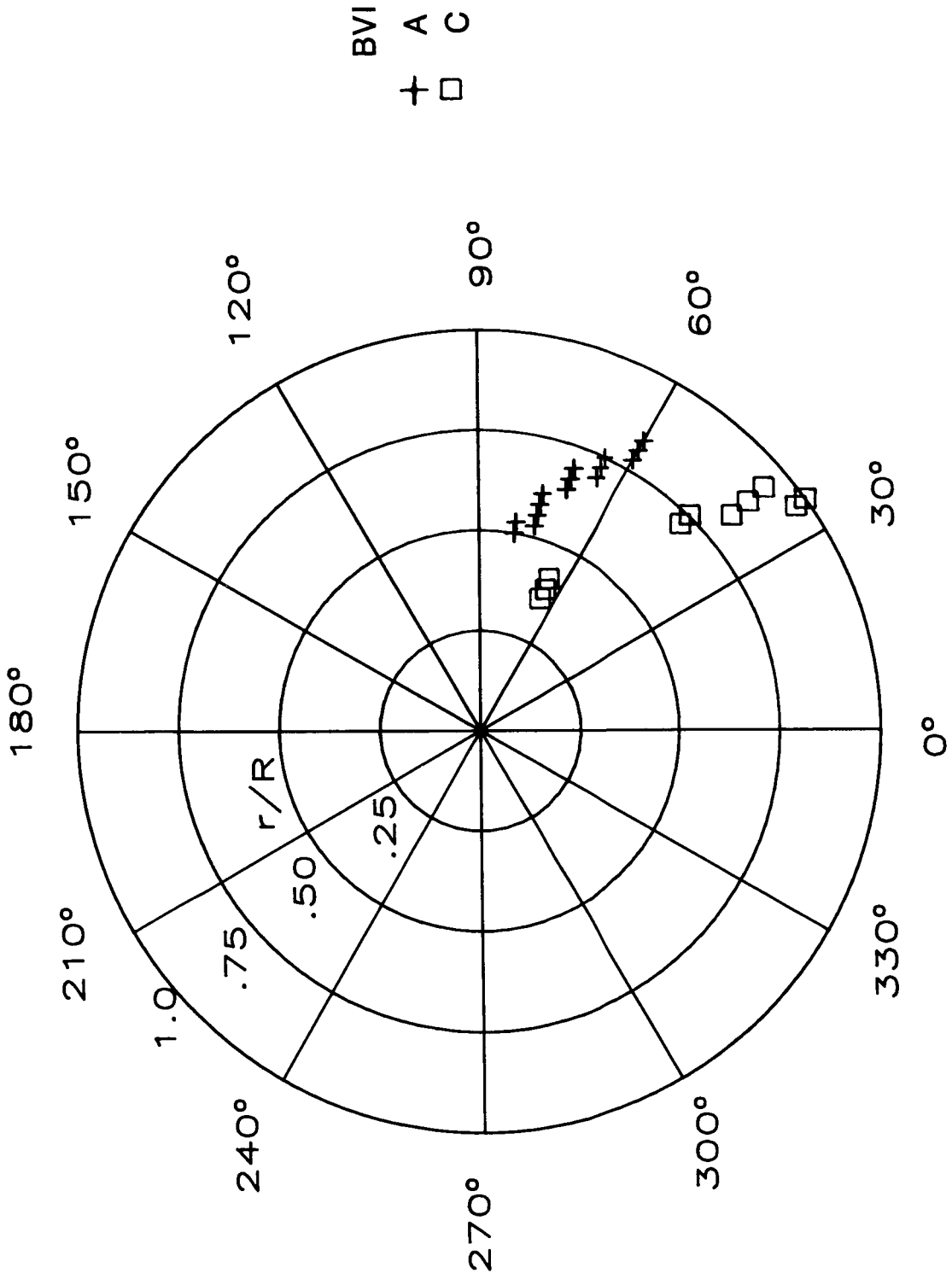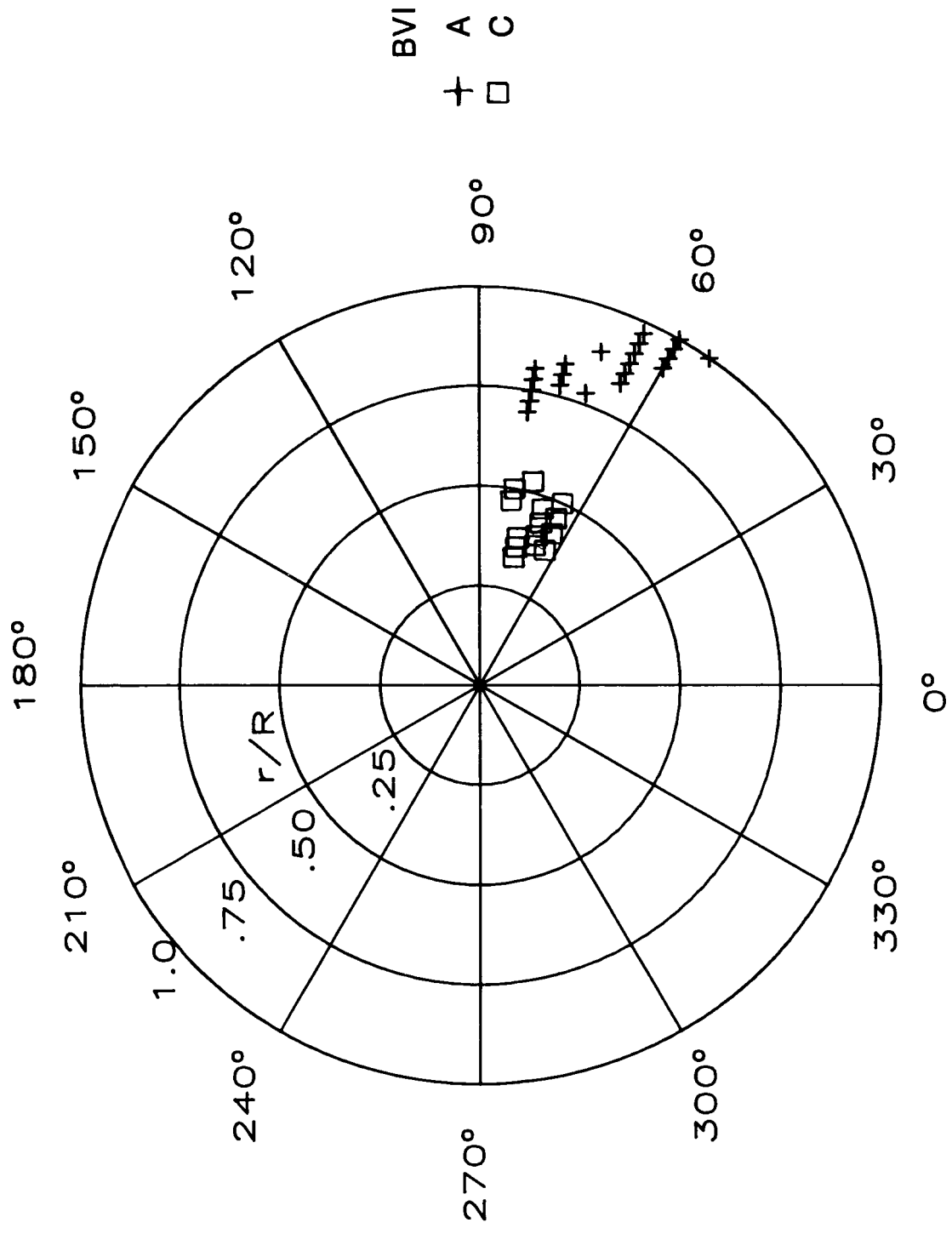BVI
+ A
□ C

r/R

.25
.50
.75
1.0

90°
120°
150°
180°
210°
240°
270°
300°
330°
0°
30°
60°

(m) $\mu = 0.167$ and $C_T = 0.00313$.

Figure A13. Continued.

(n) $\mu = 0.187$ and $C_T = 0.00309$.

Figure A13. Concluded.

References

1. Charles, Bruce D.: Acoustic Effects of Rotor-Wake Interaction During Low-Power Descent. *National Symposium on Helicopter Aerodynamic Efficiency,* American Helicopter Soc., Inc., 1975, pp. 7-1–7-8.
2. Schmitz, F. H.; and Boxwell, D. A.: In-Flight Far-Field Measurement of Helicopter Impulsive Noise. *J. American Helicopter Soc.,* vol. 21, no. 4, Oct. 1976, pp. 2–16.
3. Hardin, Jay C.; and Lamkin, Stanley L.: Aeroacoustic Interaction of a Distributed Vortex With a Lifting Joukowski Airfoil. AIAA-84-2287, Oct. 1984.
4. Booth, Earl R., Jr.; and Yu, James C.: *New Technique for Experimental Generation of Two-Dimensional Blade-Vortex Interaction at Low Reynolds Numbers.* NASA TP-2551, 1986.
5. Landgrebe, Anton J.; and Egolf, T. Alan: Prediction of Helicopter Induced Flow Velocities Using the Rotorcraft Wake Analysis. Preprint No. 1002, *32nd Annual National V/STOL Forum,* American Helicopter Soc., May 1976.
6. Landgrebe, Anton J.; and Egolf, T. Alan: *User's Manual for the UTRC Rotorcraft Wake Analysis Computer Program.* UTRC Rep. R75-911852-19 (Contract DAAJ02-74-C-0027), United Technologies Research Center, Oct. 1975.
7. Hoad, Danny R.; Helicopter Model Scale Results of Blade-Vortex Interaction Impulsive Noise as Affected by Tip Modification. *36th Annual Forum Proceedings,* American Helicopter Soc., Inc., May 1980, pp. 80-62-1–80-62-13.
8. Martin, R. M.; Elliott, J. W.; and Hoad, D. R.: Comparison of Experimental and Analytical Predictions of Rotor Blade-Vortex Interactions Using Model Scale Acoustic Data. AIAA-84-2269, Oct. 1984.
9. Berry, John D.: Quarter-Scale Testing of an Advanced Rotor System for the UH-1 Helicopter. *37th Annual Forum Proceedings,* American Helicopter Soc., Inc., 1981, pp. 456–462.
10. Berry, John D.: *Performance Testing of a Main Rotor System for a Utility Helicopter at 1/4 Scale.* NASA TM-83274, AVRADCOM TR 82-B-3, 1982.
11. Hoad, Danny R.; and Conner, David A.: Acoustic Performance Evaluation of an Advanced UH-1 Helicopter Main Rotor System. *37th Annual Forum Proceedings,* American Helicopter Soc., Inc., 1981, pp. 548–556.
12. Conner, David A.; and Hoad, Danny R.: *Reduction of High-Speed Impulsive Noise by Blade Planform Modification of a Model Helicopter Rotor.* NASA TM-84553, AVRADCOM TR 82-B-6, 1982.
13. Conner, David A.; and Hoad, Danny R.: Helicopter Model Scale Results of Blade-Vortex Interaction Impulsive Noise as Affected by Blade Planform. *38th Annual Forum Proceedings,* American Helicopter Soc., Inc., 1982, pp. 528–537.
14. Conner, David A.; and Hoad, Danny R.: *Experimental Blade Vortex Interaction Noise Characteristics of a Utility Helicopter at 1/4 Scale.* NASA TM-84653, AVSCOM TM 83-B-1, 1984.
15. Wilson, John C.; A General Rotor Model System for Wind-Tunnel Investigations. *J. Aircr.,* vol. 14, no. 7, July 1977, pp. 639–643.
16. Bingham, Gene J.; and Noonan, Kevin W.: *Two-Dimensional Aerodynamic Characteristics of Three Rotorcraft Airfoils at Mach Numbers From 0.35 to 0.90.* NASA TP-2000, AVRADCOM TR 82-B-2, 1982.
17. Theobald, M. A.: *Evaluation of the Acoustic Measurement Capability of the NASA Langley V/STOL Wind Tunnel Open Test Section With Acoustically Absorbent Ceiling and Floor Treatments.* Rep. No. 3820 (Contract NAS1-14611-18), Bolt Beranek and Newman Inc., May 1978.
18. Cox, C. R.: Helicopter Rotor Aerodynamic and Aeroacoustic Environments. AIAA Preprint 77-1338, Oct. 1977.
19. Hoad, Danny R.: *Evaluation of Helicopter Noise Due to Blade-Vortex Interaction for Five Tip Configurations.* NASA TP-1608, 1979.
20. Widnall, Shelia: Helicopter Noise Due to Blade-Vortex Interaction. *J. Acoust. Soc. America,* vol. 50, no. 1, pt. 2, July 1971, pp. 354–365.
21. Leighton, Kenneth P.; Hubbard, James E., Jr.; Harris, Wesley L.; and Peele, Stephen E. A.: Parametric Studies and Flow Visualization of Model Helicopter Rotor Blade Slap. Paper presented at the AIAA Seventh Aeroacoustics Conference (Palo Alto, California), Oct. 5–7, 1981.
22. Hubbard, James E., Jr.; and Leighton, Kenneth P.: A Comparison of Model Helicopter Rotor Primary and Secondary Blade/Vortex Interaction Blade Slap. AIAA-83-0723, Apr. 1983.
23. Beddoes, T. S.: A Wake Model for High Resolution Airloads. *Proceedings of International Conference on Rotorcraft Basic Research,* American Helicopter Soc., Inc., 1985.
24. Landgrebe, Anton J.; Taylor, Robert B.; Egolf, T. Alan; and Bennett John C.: Helicopter Airflow and Wake Characteristics for Low Speed and Hovering Flight From Rocket Interference Investigations. *37th Annual Forum Proceedings,* American Helicopter Soc., Inc., May 1981, pp. 51–65.
25. Egolf, T. A.; and Landgrebe, A. J.: Generalized Wake Geometry for a Helicopter Rotor in Forward Flight and Effect of Wake Deformation on Airloads. *40th Annual Forum Proceedings,* American Helicopter Soc., Inc., 1984, pp. 359–376.

1. Report No. NASA TP-2658 AVSCOM TM 87-B-1	2. Government Accession No.	3. Recipient's Catalog No.
4. Title and Subtitle Helicopter Blade-Vortex Interaction Locations—Scale-Model Acoustics and Free-Wake Analysis Results		5. Report Date April 1987
		6. Performing Organization Code 505-61-51-10
7. Author(s) Danny R. Hoad		8. Performing Organization Report No. L-16214
9. Performing Organization Name and Address Aerostructures Directorate USAARTA-AVSCOM Langley Research Center Hampton, VA 23665-5225		10. Work Unit No.
		11. Contract or Grant No.
12. Sponsoring Agency Name and Address National Aeronautics and Space Administration Washington, DC 20546-0001 and U.S. Army Aviation System Command St. Louis, MO 63120-1798		13. Type of Report and Period Covered Technical Paper
		14. Sponsoring Agency Code 1L162209AH76A

15. Supplementary Notes
Danny R. Hoad: Aerostructures Directorate, USAARTA-AVSCOM.

16. Abstract
The results of a model rotor acoustic test in the Langley 4- by 7-Meter Tunnel are used to evaluate a free-wake analytical technique. An acoustic triangulation technique is used to locate the position in the rotor disk where the blade-vortex interaction noise originates. These locations, along with results of the rotor free-wake analysis, are used to define the geometry of the blade-vortex interaction noise phenomena as well as to determine if the free-wake analysis is a capable diagnostic tool. Data from tests of two teetering rotor systems are used in these analyses.

17. Key Words (Suggested by Authors(s)) Helicopter Rotor Free wake Acoustics Blade-vortex interaction Vortices	18. Distribution Statement Unclassified Unlimited Subject Category 02

19. Security Classif.(of this report) Unclassified	20. Security Classif.(of this page) Unclassified	21. No. of Pages 106	22. Price A06